Your Development Partner of Smart Devices

INTERNATIONAL CENTER FOR ACTUATORS AND TRANSDUCERS

Materials Research Institute
The Pennsylvania State University
University Park, PA 16802
Director Prof. Kenji Uchino

Contact
Prof. Kenji Uchino
134 Materials Research Lab
Kenjiuchino@psu.edu
814-863-8035

http://www.psu.edu/dept/ICAT

Report Documentation Page

Form Approved
OMB No. 0704-0188

Public reporting burden for the collection of information is estimated to average 1 hour per response, including the time for reviewing instructions, searching existing data sources, gathering and maintaining the data needed, and completing and reviewing the collection of information. Send comments regarding this burden estimate or any other aspect of this collection of information, including suggestions for reducing this burden, to Washington Headquarters Services, Directorate for Information Operations and Reports, 1215 Jefferson Davis Highway, Suite 1204, Arlington VA 22202-4302. Respondents should be aware that notwithstanding any other provision of law, no person shall be subject to a penalty for failing to comply with a collection of information if it does not display a currently valid OMB control number.

1. REPORT DATE **00 JUN 2003**	2. REPORT TYPE **N/A**	3. DATES COVERED **-**

4. TITLE AND SUBTITLE **International Center For Actuators And Transducers**	5a. CONTRACT NUMBER
	5b. GRANT NUMBER
	5c. PROGRAM ELEMENT NUMBER
6. AUTHOR(S)	5d. PROJECT NUMBER
	5e. TASK NUMBER
	5f. WORK UNIT NUMBER
7. PERFORMING ORGANIZATION NAME(S) AND ADDRESS(ES) **Materials Research Institute Pennsylvania State University University Park, PA 16802**	8. PERFORMING ORGANIZATION REPORT NUMBER
9. SPONSORING/MONITORING AGENCY NAME(S) AND ADDRESS(ES)	10. SPONSOR/MONITOR'S ACRONYM(S)
	11. SPONSOR/MONITOR'S REPORT NUMBER(S)

12. DISTRIBUTION/AVAILABILITY STATEMENT
Approved for public release, distribution unlimited

13. SUPPLEMENTARY NOTES
See also ADM001697, ARO-44924.1-EG-CF, International Conference on Intelligent Materials (5th)(Smart Systems & Nanotechnology)., The original document contains color images.

14. ABSTRACT

15. SUBJECT TERMS

16. SECURITY CLASSIFICATION OF:			17. LIMITATION OF ABSTRACT	18. NUMBER OF PAGES	19a. NAME OF RESPONSIBLE PERSON
a. REPORT **unclassified**	b. ABSTRACT **unclassified**	c. THIS PAGE **unclassified**	**UU**	**121**	

Standard Form 298 (Rev. 8-98)
Prescribed by ANSI Std Z39-18

MISSION

The world center for fundamental and application oriented research on ceramic actuators and transducers

Founded: 1992

People

35	Persons
12	Faculty
1	Secretary
2	Research Associates
12	Graduate Students
8	Visiting Professors/Researchers

Supported by

10	Industry Members

-ICAT Research Activities-

1. Compact Ultrasonic Motors
Windmill motor (flat and short)
PZT tube motor (thin and long)
Metal tube motor (cheaper version)
2. Piezoelectric Transformers
3. New Actuator Materials
High EM coupling single crystals
$Pb(Zn_{1/3}Nb_{2/3})O_3$ $PbTiO_3$
Photostriction
4. Reliability of Actuators
Acoustic emission
Loss mechanisms in piezoelectrics
High power piezoelectric materials
Rare Earth Metals doped PZT- $Pb(Mn_{1/3}Sb_{2/3})O_3$
5. Piezoelectric Thin Films
6. Actuator Modeling

Compact Ultrasonic Motors

Windmill Motor

The 3 mm Motor (Koc et. al., 1999)

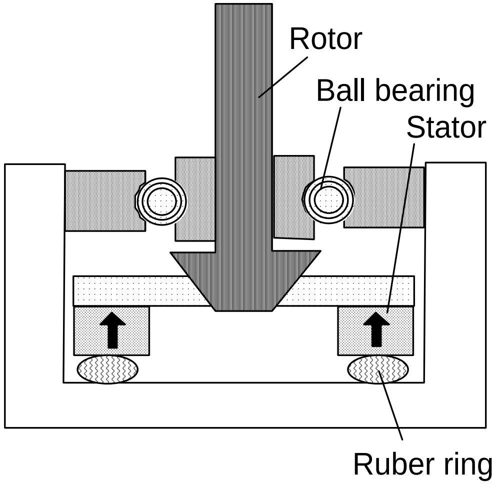

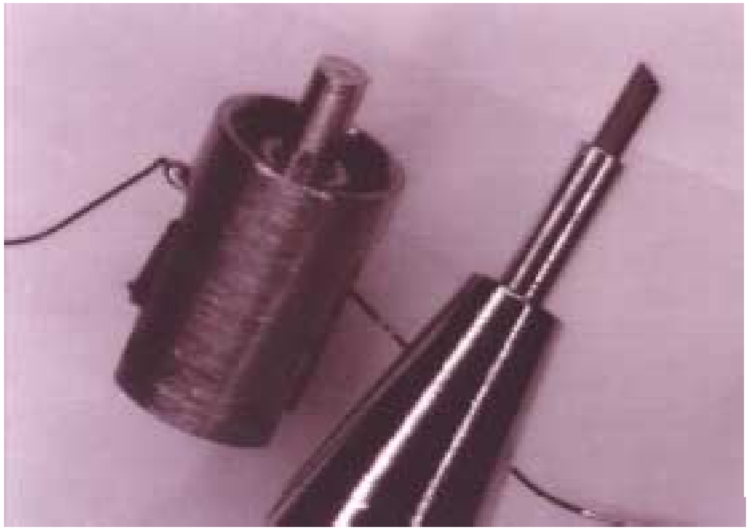

Encapsulated motor next to a 0.5 mm metallic pencil
(Steel housing was coated with an epoxy insulator)

Metal Tube Motor

A PIEZOELECTRIC MOTOR USING TWO ORTHOGONAL BENDING MODES OF A HOLLOW CYLINDER

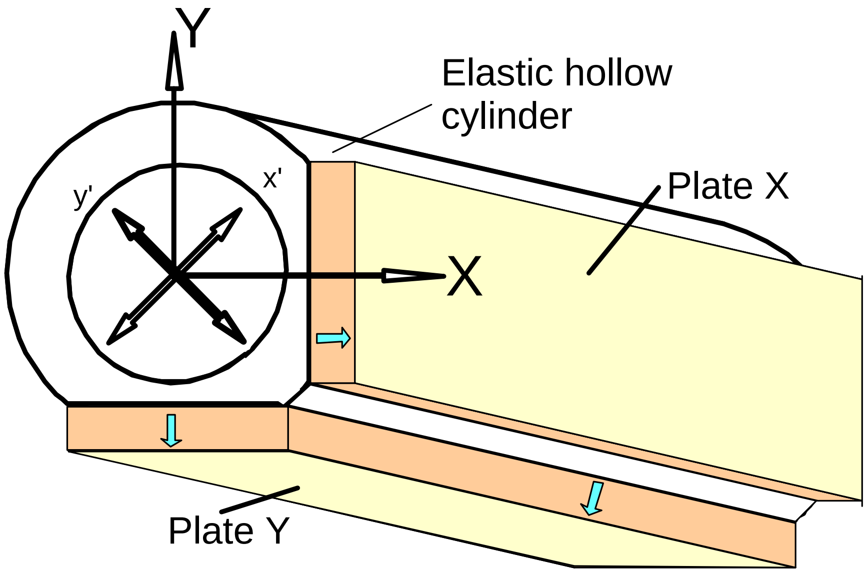

Structure of the motor stator

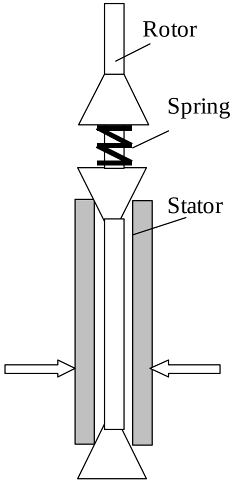

Assembly of the motor

Metal Tube Motor

Manufactured Motors

Dimensions of the Stator	**1st**	**2nd**	**3rd**
Outside Diameter	2.4 mm	1.6 mm	1.6 mm
Length of the Stator	10 mm	6 mm	**4 mm**
Total Length	~15 mm	~10 mm	**~5 mm**

1st

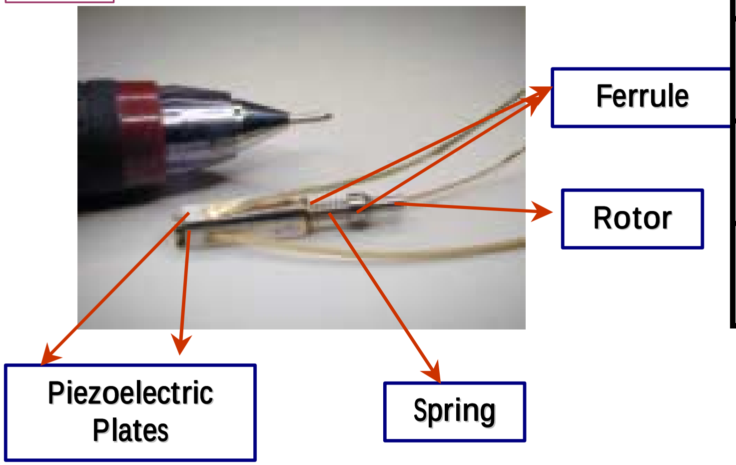
Ferrule

Rotor

Piezoelectric Plates

Spring

2nd

3rd

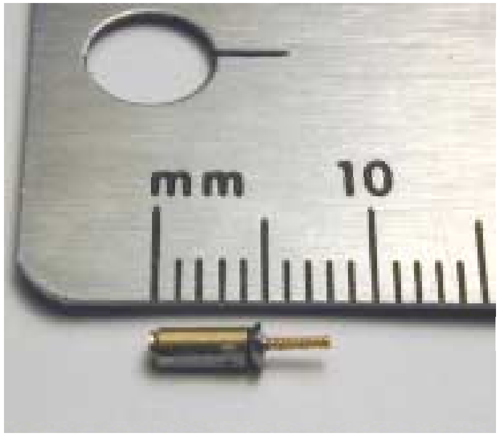

STRUCTURE OF THE MICRO VEHICLE

- ***Two piezoelectric motors*** were connected from the stator's nodal points with.
- Each motor has two tires, so the robot has four tires.
- Each piezoelectric motor has three electrical cables for a rotation of cw and ccw directions.
- The robot can move forward when both motors are spinning at the same time.
- For left or right turns one of the motors needs to stop while the other motor is operating.

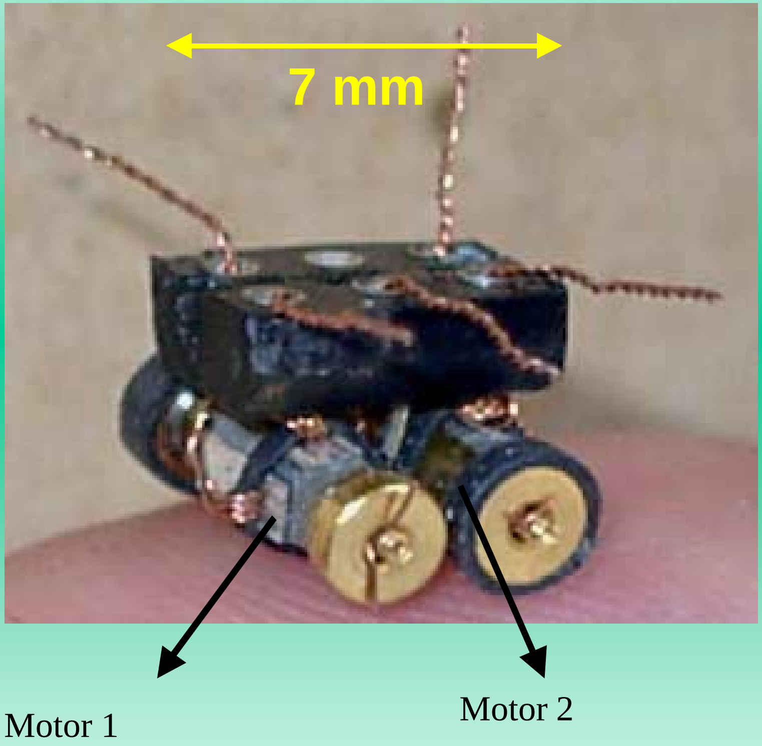

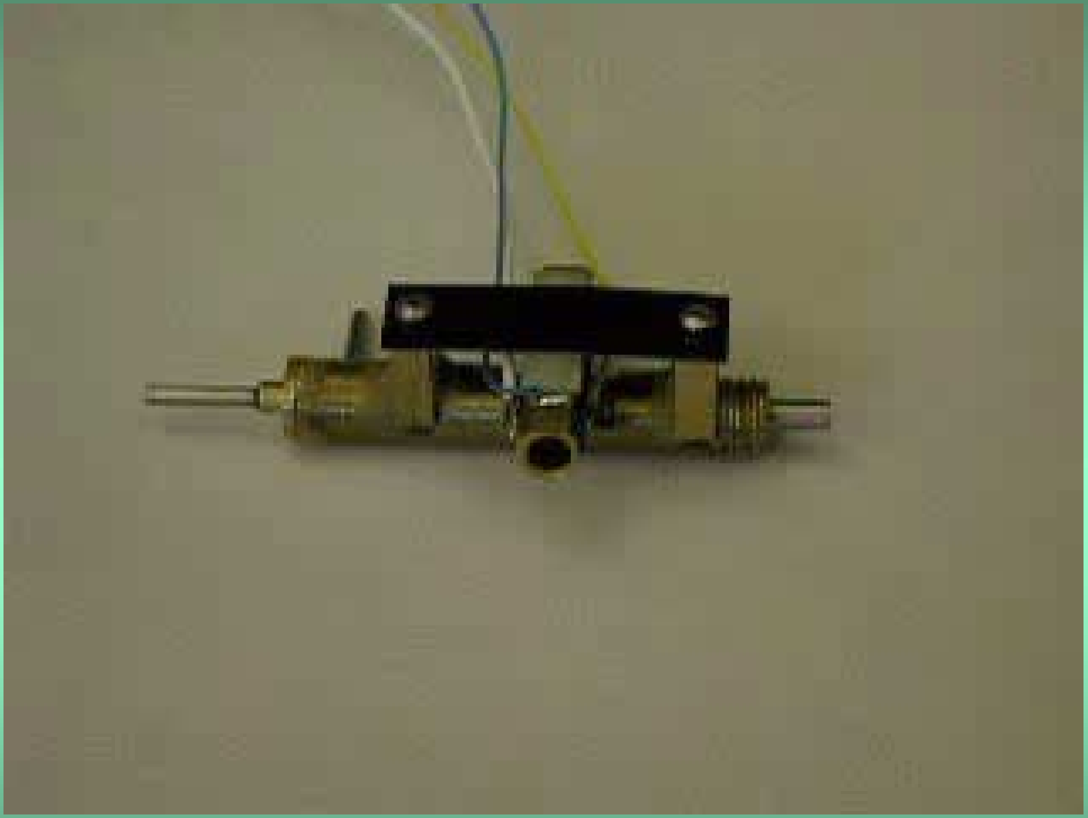

Micro gas valve using a metal tube USM

Piezoelectric Transformer

Conventional Electromagnetic Transformer

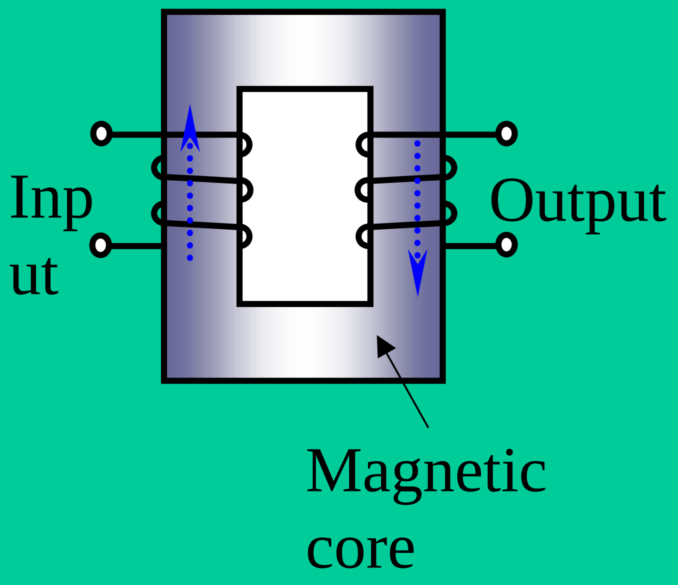

Piezoelectric Transformer

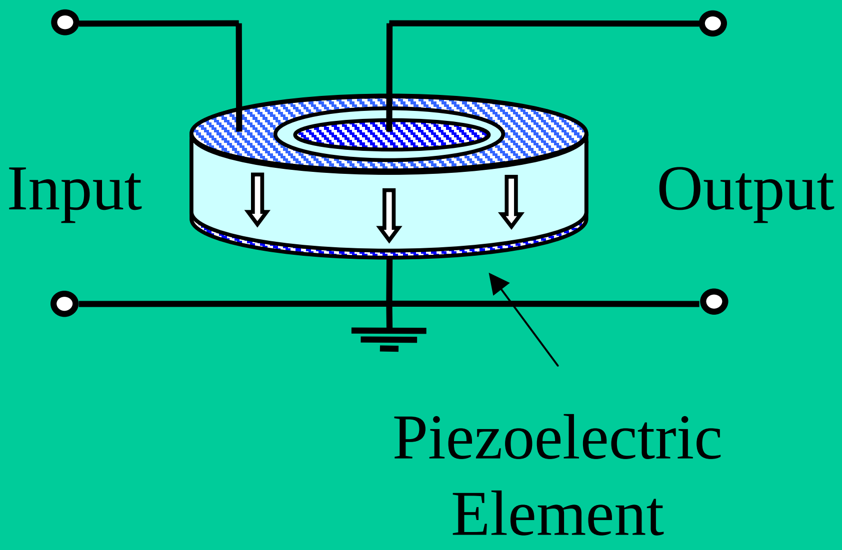

-Compact size and light weight
-High efficiency
-Non-flammable (no wire)
-No electromagnetic noise generation

Piezoelectric Transformer

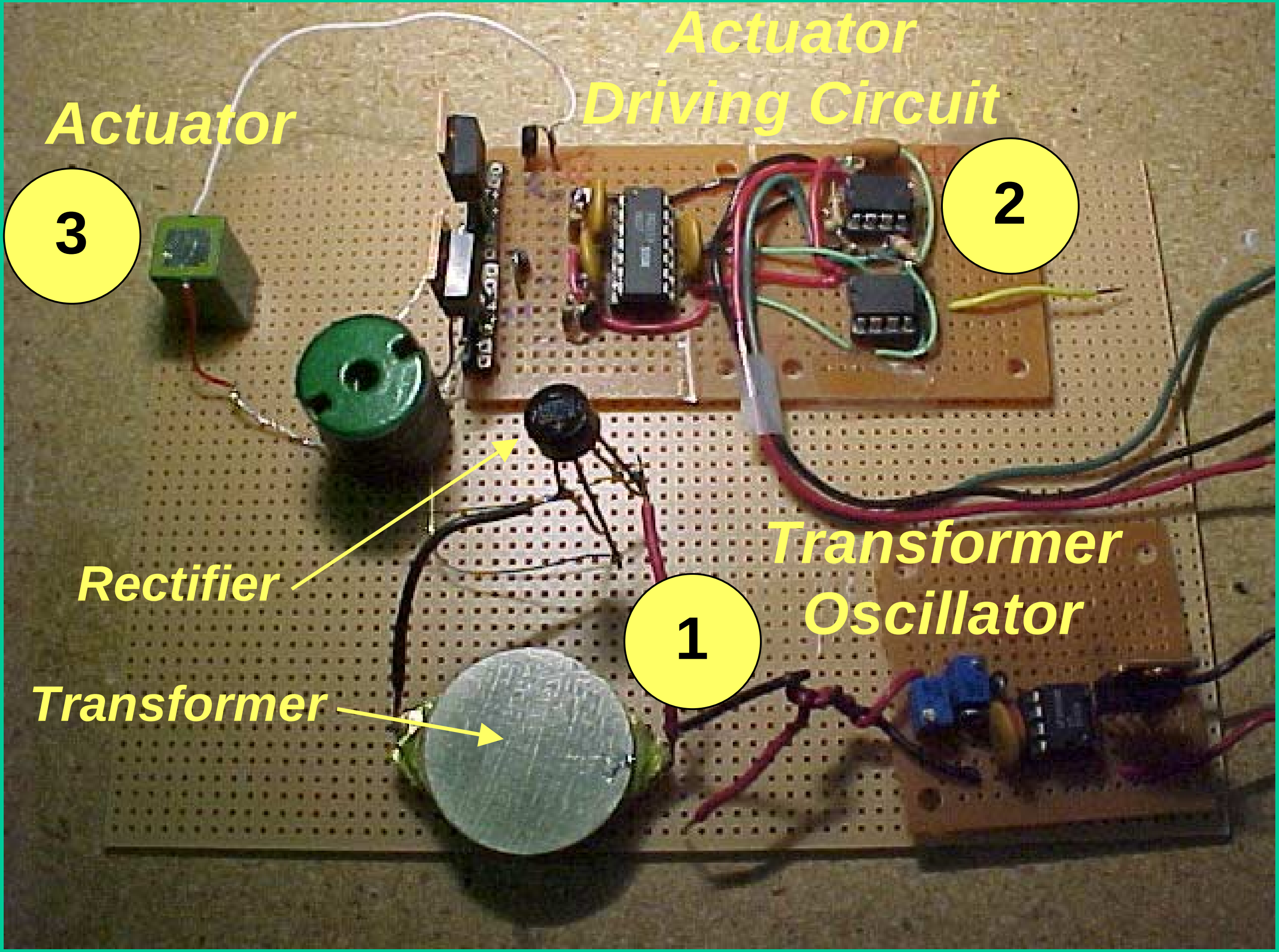

New Actuator Materials

Growth of PZN-PT Single Crystals

Mn-doped

- Modified and pure PZN-PT (8-9 mol%) single crystals are grown by self flux method.
- Crystals are <001> oriented along crystallographic direction using Laue technique.
- High Power samples have dimensions as per IEEE standard.

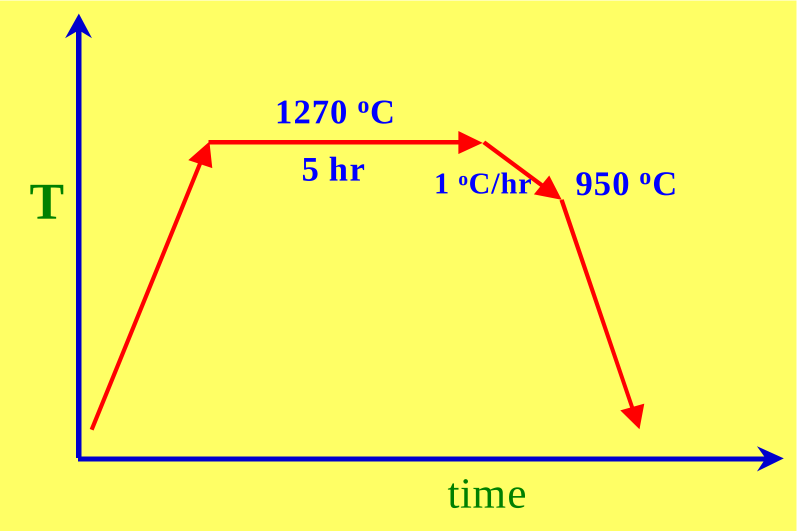

Photo-Driven Micro Walking Device

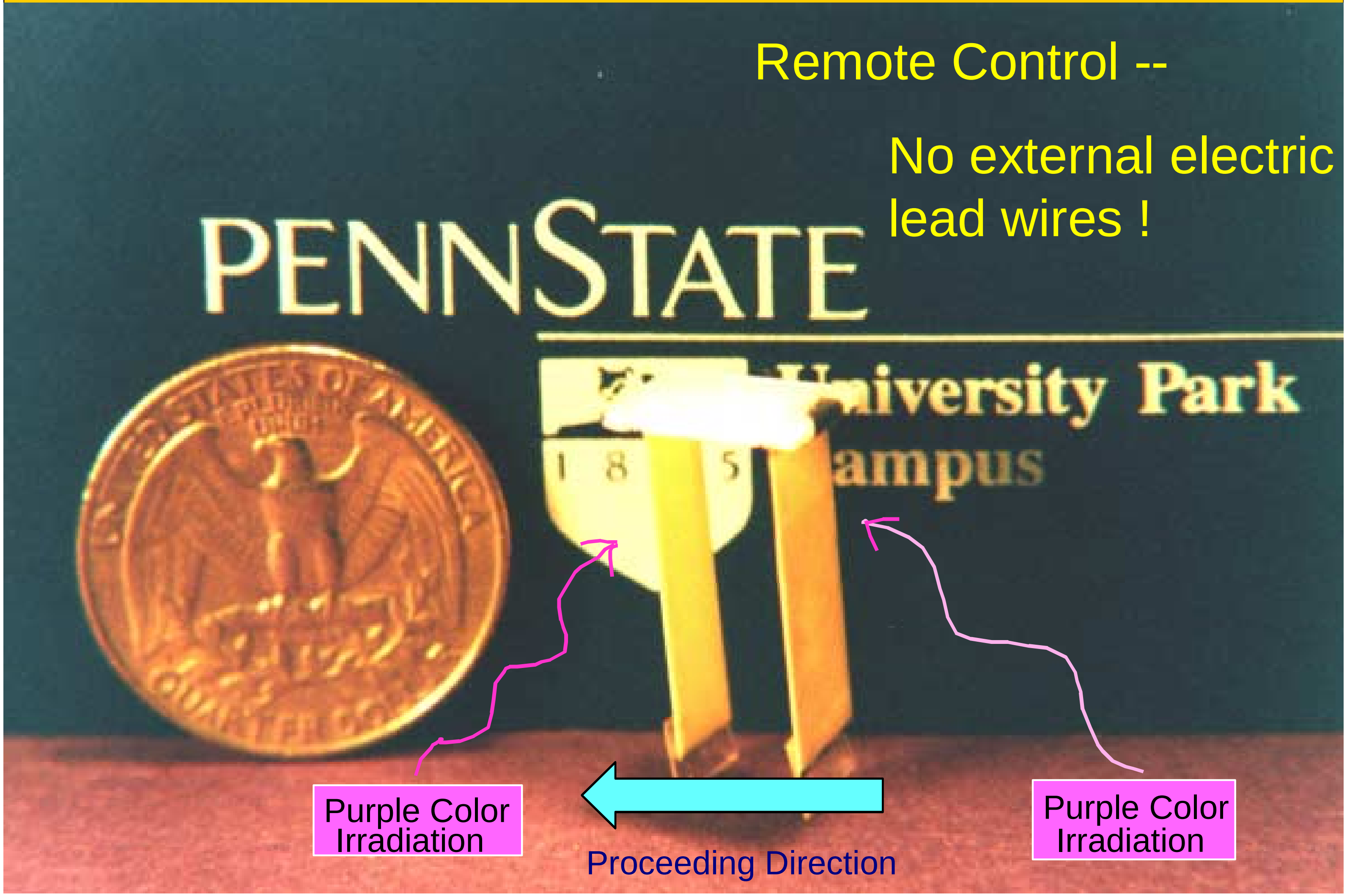

Remote Control --

No external electric lead wires !

Purple Color Irradiation

Purple Color Irradiation

Proceeding Direction

Reliability of Actuators

Loss and Heat Generation

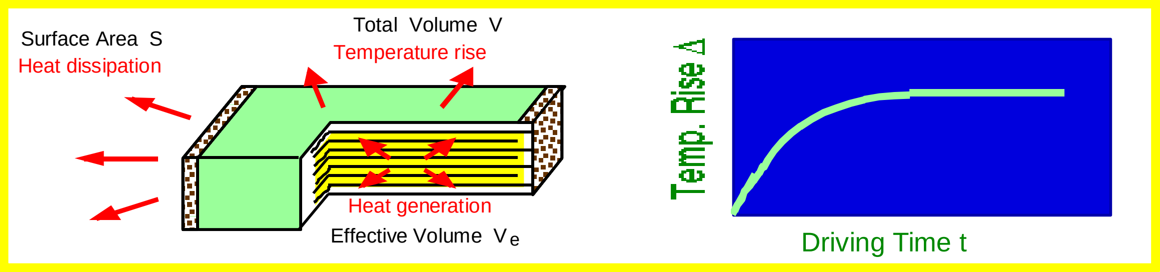

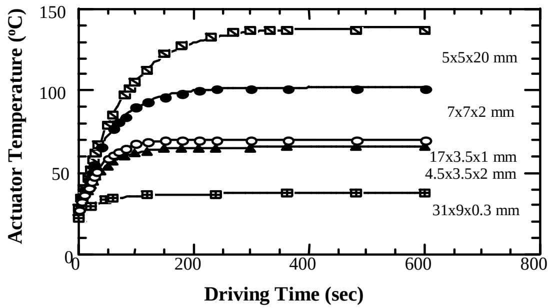

Fig. 1. Heat generation for various actuators (driven at 3 kV/mm, 300 Hz)

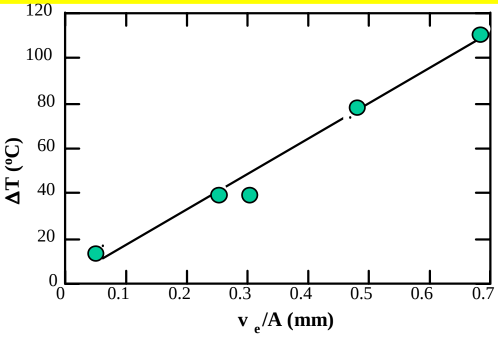

Fig. 2. Temperature rise vs v_e/A (3 kV/mm, 300 Hz).

Table I Loss and overall heat transfer coefficient for PZT multilayer samples (E = 3 kV/mm, f = 300 Hz).

Actuator	4.5x3.5x2 mm	7x7x2 mm	17x3.5x1 mm
Total loss (x10^{3}J/m^3)	19.2	19.9	19.7
P-E hysteresis loss (x10^{3}J/m^3) $u = \frac{\rho cv}{f v_e}\left(\frac{dT}{dt}\right)_{t\to 0}$	18.5	17.8	17.4
k(T) (W/m^{2}K)	38.4	39.2	34.1

Intensive dielectric loss tan δ'

High-Power Piezo-Materials (Cont.)

PZT-$Pb(Mn_{1/3}Sb_{2/3})O_3$

[Takahashi,Sasaki,Hirose and Uchino, Mat.Res.Soc.Proc. Vol.360,305, 1995]

Yb,Eu, Ce Doping

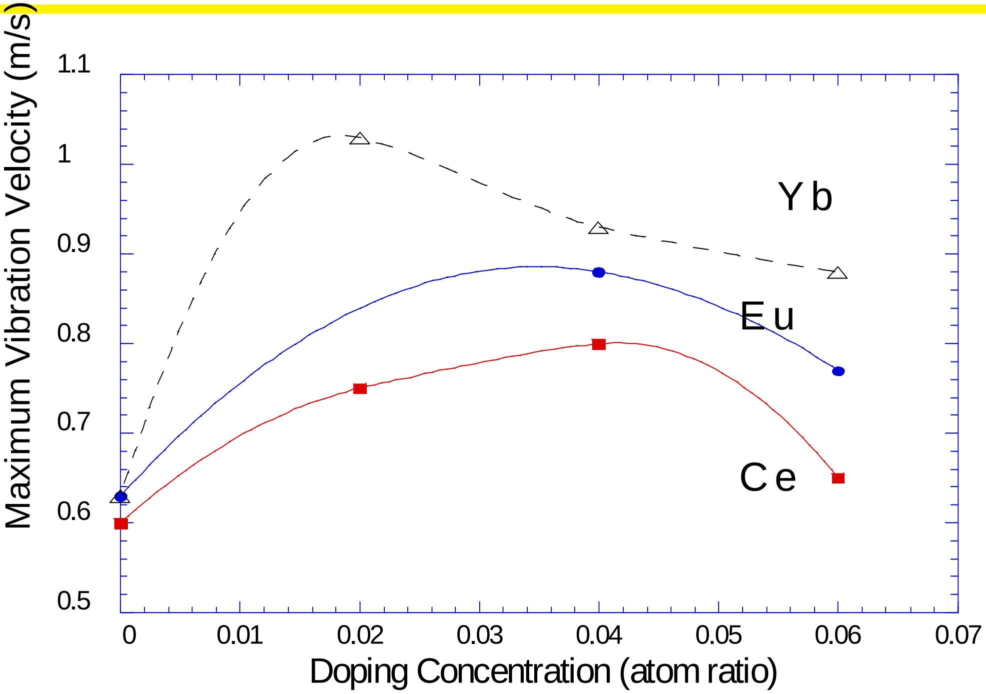

Piezoelectric Thin Films

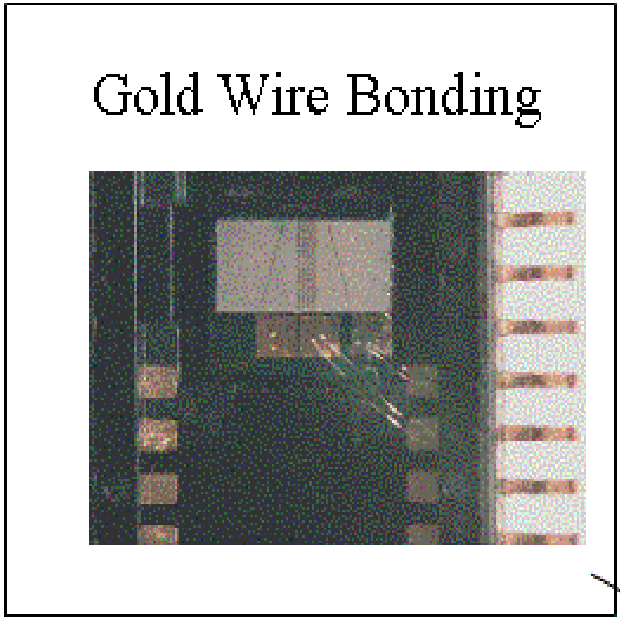

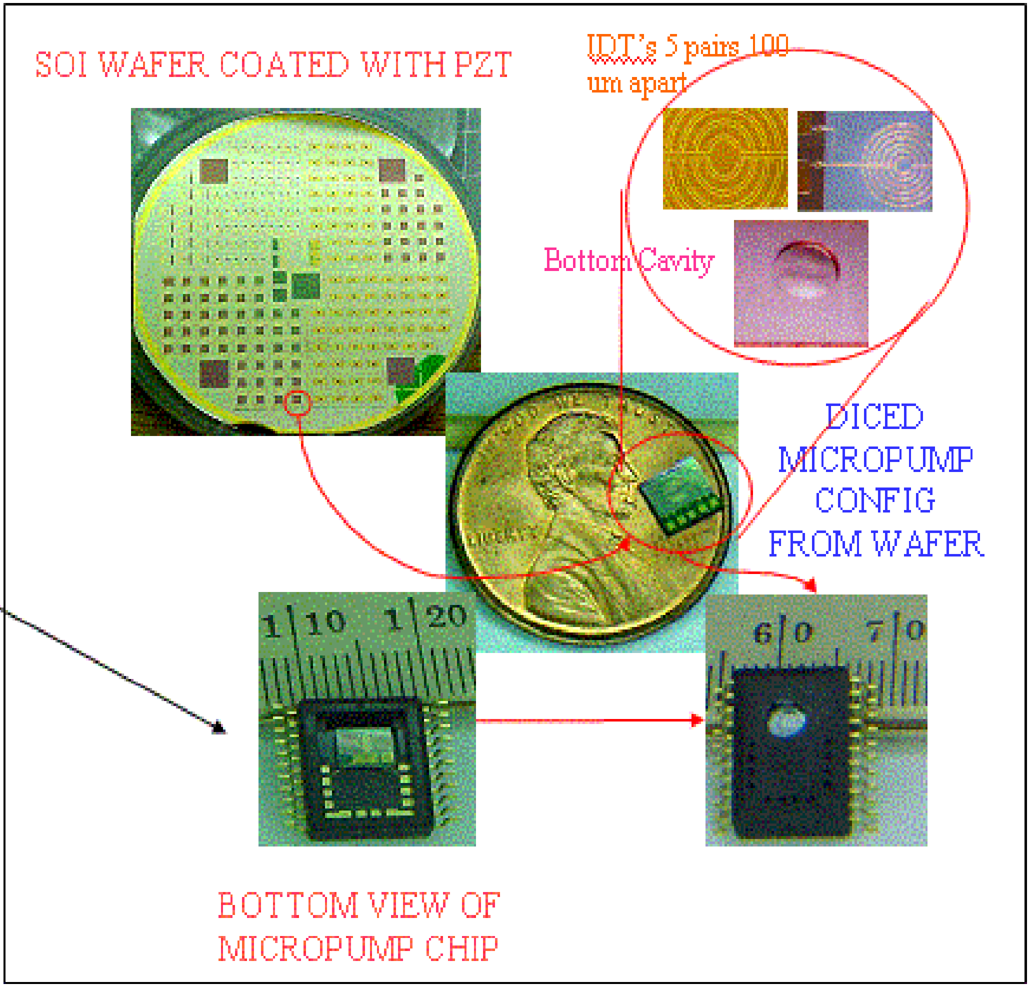

Composite Transducers

Flextensional Transducers

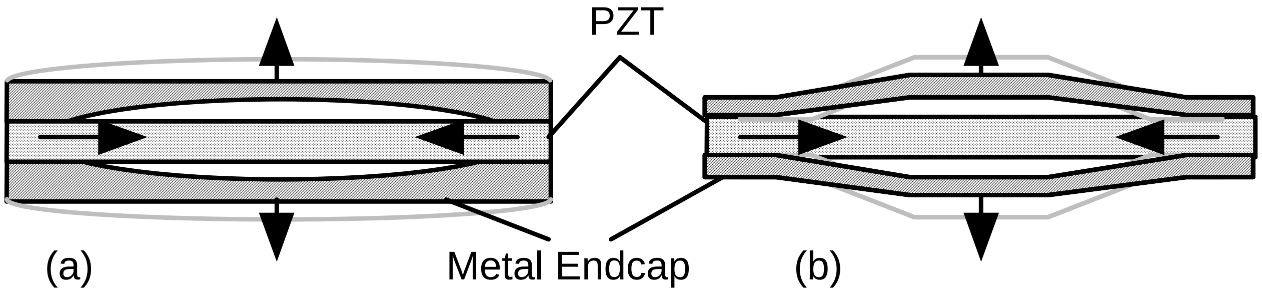

Comparison of the structures for a Moonie (a) and a Cymbal (b).

(0,1) mode, 17kHz

Application with ATILA Windmill Motor

Application with ATILA
Piezo Transformer

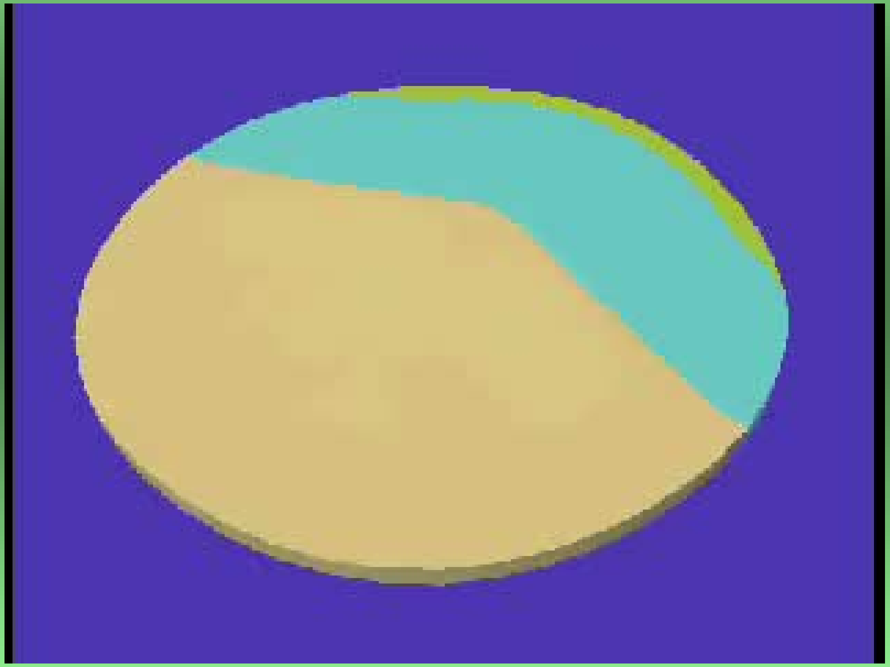

Introduction to Micromechatronics

K. Uchino, International Center for Actuators and Transducers, Penn State University
University Park, PA 16802, USA

1. THE NEED FOR NEW ACTUATORS

An *actuator* is a transducer that transforms drive energy into a mechanical displacement or force. The demand for new actuators has increased significantly in recent years especially for *positioner*, *mechanical damper*, and *miniature motor* applications. These devices are used in a variety of fields such as optics, astronomy, fluid control, and precision machining.

Sub-micrometer fabrication, common in the production of electronic chip elements, is also becoming important in mechanical engineering. The trends depicted in Figure 1 show how machining accuracy has improved over the years.[1] One of the primary reasons for the improved accuracy is the development of more precise position sensors. Sensors utilizing lasers can easily detect nanometer scale displacements. This could be regarded as another instance of "the chicken or the egg" issue, however, as the fabrication of such precise optical instruments can only be achieved with the submicrometer machining equipment the sensors are designed to monitor.

In an actual machining apparatus comprised of translational components (the joints) and rotating components (the gears and motor) error due to backlash will occur. Machine vibration will also lead to unavoidable position fluctuations. Furthermore, the deformations due to machining stress and thermal expansion also cannot be ignored. The need for submicron displacement positioners to improve cutting accuracy is apparent. One example is a prototype for a lathe machine that uses a ceramic multilayer actuator and can achieve cutting accuracy of 0.01μm.[2]

The concept of *"adaptive optics"* has been applied in the development of sophisticated new optical systems. Earlier systems were generally designed such that parameters like position, angle, or the focal lengths of mirror and lens components remained essentially fixed during operation. Newer systems incorporating adaptive optical elements respond to a variety of conditions to essentially adjust the system parameters to maintain optimum operation. The original "lidar" system (a radar system utilizing light waves) was designed to be used on the NASA space shuttle for monitoring the surface of the earth.[3] A laser beam is projected towards the earth's surface, and the reflected light is received by a reflection telescope, amplified by a photomultiplier, and the resulting signal is processed to produce an image. The vibration noise and temperature fluctuations of the shuttle make it difficult for a sharp image to be obtained, however, and the use of a responsive positioner was considered to compensate for the detrimental effects.

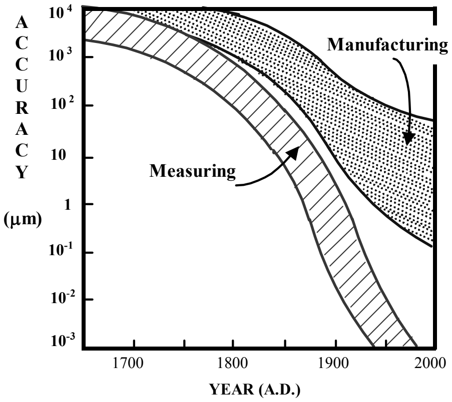

Figure 1 Obtainable accuracies in manufacturing and measurement over time. Note that current accuracies tend to be on the micrometer and nanometer scales, respectively.

Active and passive vibration suppression by means of piezoelectric devices is also promising technology for use in space structures and military and commercial vehicles. Mechanical vibration in a structure traveling through the vacuum of space is not readily damped and a 10 m long array of solar panels can be severely damaged simply by the repeated impact of space dust with the structure. Active dampers using shape memory alloys or piezoelectric ceramics are currently under investigation to remedy this type of problem. A variety of *smart skins* designed for military tanks or submarines are illustrated in Figure 2. A signal is generated in the sensitive skin with perhaps the impact of a missile on the tank or the complex forces applied to a submarine through turbulent flow, which is fed back to an actuator. The actuator responds by changing its shape to effectively minimize the impact damage on the tank (*structure protection*) or the drag force on the submarine.

The demand for other applications in the field of mechanical engineering is also increasing rapidly. One important class of devices that meets these demands is the "*solid-state motor*." Market research focused on just office equipment needs, such as printers and floppy disk drives, indicates that tiny motors smaller than 1 cm will be in increasing demand over the next ten years. Conventional electromagnetic motor designs, however, do not provide sufficient energy efficiency for these applications. Piezoelectric *ultrasonic motors*, whose efficiency is insensitive to size, are superior to the conventional devices when motors of millimeter size are required.

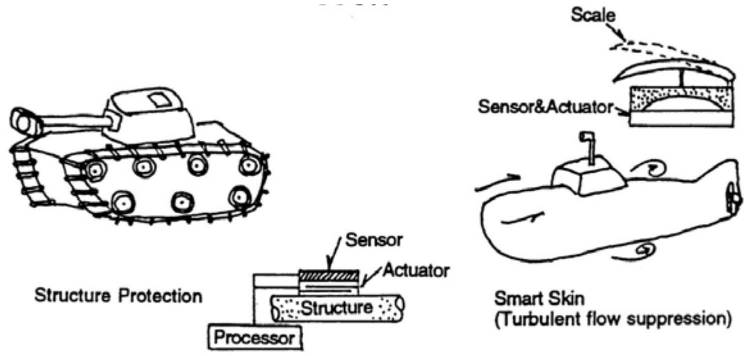

Figure 2 Smart skin structures for military tanks and submarines.

2. CONVENTIONAL METHODS FOR MICROPOSITIONING

A classification of actuators, is presented in Table 1. This classification is based on the features of the actuator that relate to micropositioning controllability. Electrically controlled types are generally preferred for applications where miniature devices are needed. A few of the relevant specifications for the solid-state actuators included in this classification also appear in the table. Compared with conventional devices, the new principle actuators provide much quicker response, smaller size, higher resolution, and a higher power-to-weight ratio.

Conventional methods for micropositioning usually include displacement reduction mechanisms to suppress mechanical backlash, which are categorized into three general groups: (1) oil/air pressure displacement reduction, (2) the electromagnetic rotary motor with a gear, and (3) the voice coil motor.[4] A brief description of each follows.

(1) Oil Pressure Type Displacement Reduction Mechanism

Changing the diameter of an oil-filled cylinder as illustrated in Figure 3 effectively reduces the resulting displacement at the output. Devices utilizing this oil pressure mechanism are generally large and have slow responses. Transducers of this type are sometimes used in the reverse mode for amplifying the displacement produced by a solid-state actuator.

(2) Combination of a Motor and a Displacement Reduction Mechanism

Screw transfer mechanisms are typically used when the moving distance is long (see Figure 4). Using very precise ball screws, positioning accuracy of less than 5 μm can be obtained for a 100 mm motion. When higher accuracies are required, additional displacement reduction mechanisms are necessary.

Table 1 Displacement characteristics of various types of actuators.

Drive	Device	Displacement	Accuracy	Torque/ Generative Force	Response Time
Air pressure	**Motor**	**Rotation**	**degrees**	**50 Nm**	**10 sec**
	Cylinder	**100 mm**	**100 μm**	**10^{-1} N/mm^2**	**10 sec**
Oil pressure	**Motor**	**Rotation**	**degrees**	**100 Nm**	**1 sec**
	Cylinder	**1000 mm**	**10 μm**	**100 N/mm^2**	**1 sec**
Electricity	**AC Servo Motor**	**Rotation**	**minutes**	**30 Nm**	**100 msec**
	DC Servo Motor	**Rotation**	**minutes**	**200 Nm**	**10 msec**
	Stepper Motor	**1000 mm**	**10 μm**	**300 N**	**100 msec**
	Voice Coil Motor	**1 mm**	**0.1 μm**	**300 N**	**1 msec**
	New Piezoelectric	**100 μm**	**0.01 μm**	**30 N/mm^2**	**0.1 msec**
	Magnetostrictor	**100 μm**	**0.01 μm**	**100 N/mm^2**	**0.1 msec**
	Ultrasonic Motor (piezoelectric)	**Rotation**	**minutes**	**1 Nm**	**1 msec**

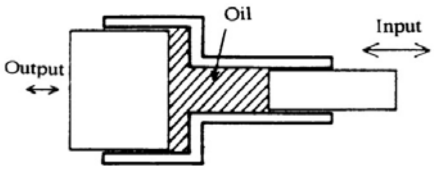

Figure 3 Schematic representation of an oil pressure displacement reduction mechanism.

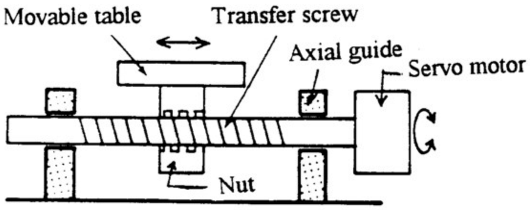

Figure 4 Illustration of a screw positioning mechanism.

There are several other commonly used displacement reduction mechanisms. The mechanisms highlighted in Figure 5 illustrate the action of a spring constant difference, a hinge lever, and a wedge. The combination of a motor with a ball screw or a displacement reduction mechanism has the advantages of quick response, a substantial generative force, and good controllability, but is generally difficult to fabricate in miniature form due to its structural complexity. In addition, the manufacturing tolerances of a typical transfer screw tend to promote backlash in positioning even when displacement reduction mechanisms are implemented.

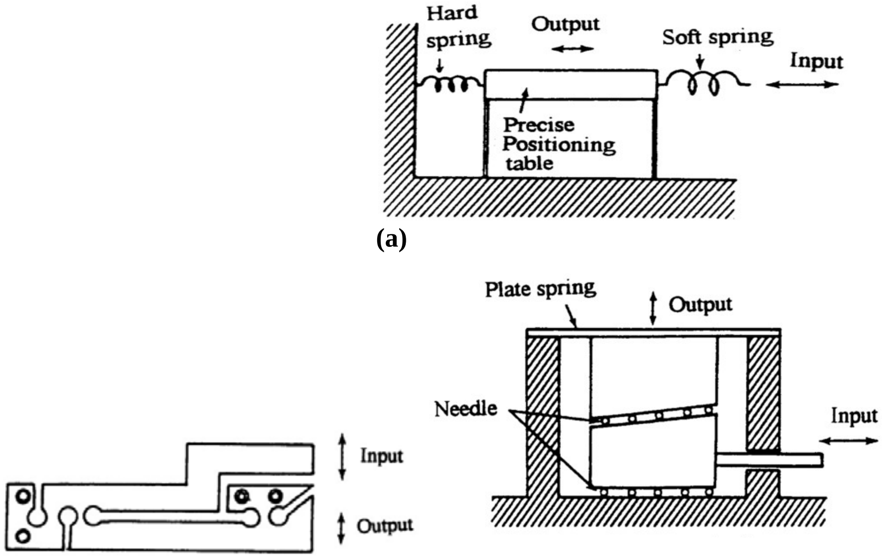

(a)

(b)

(c)

Figure 5 Illustrations of several displacement reduction mechanisms utilizing the action of: (a) a spring constant difference, (b) a hinge lever, and (c) a wedge.

The minimum size of an electromagnetic motor is generally limited to about 1 cm, as motors smaller than this will not provide adequate torque and efficiency. One of the smallest electromagnetic motors to be fabricated is shown in Figure 6.[5] A micromotor with a diameter of 1.9 mm typically generates a torque of only 7.5 μNm and rotational speeds of 100,000 rpm. An optional microgearbox with a reduction ratio of 47 can be used with this motor so that the drive can deliver an enhanced torque of up to 300 μNm. Use of this gearbox, however, reduces the efficiency of the motor significantly. Further, as the size of electromagnetic motor is reduced the winding wire thickness must also be reduced, which leads to a significant increase in the electrical resistance and Joule heating.

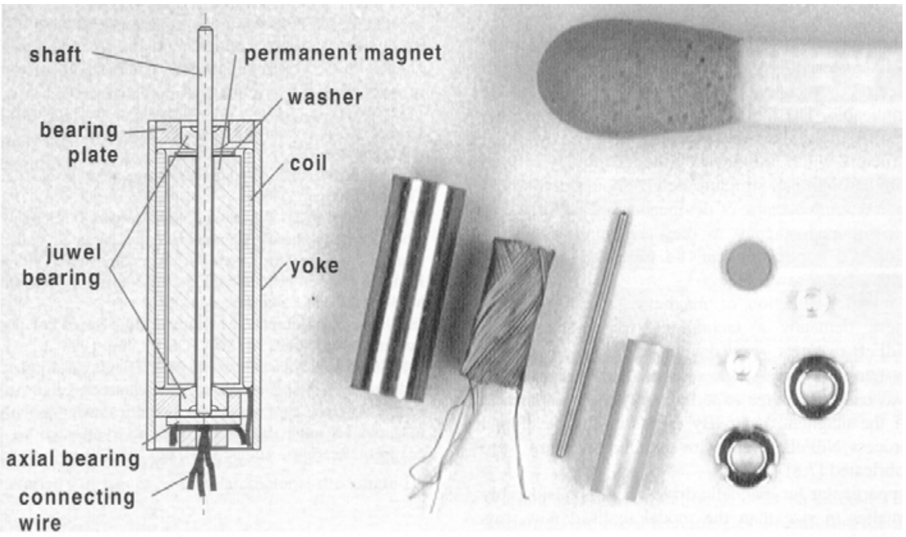

Figure 6 An electromagnetic micromotor with a diameter of 1.9 mm, developed by the Institute of Microtechnique, Mainz GmbH.[5]

(3) Voice Coil Motors

The structure of a voice coil motor is shown schematically in Figure 7. Among the three displacement control devices described here, this motor achieves the most precise positioning. It requires relatively large input electrical energy, however, has a slow response, and produces rather low generative forces.

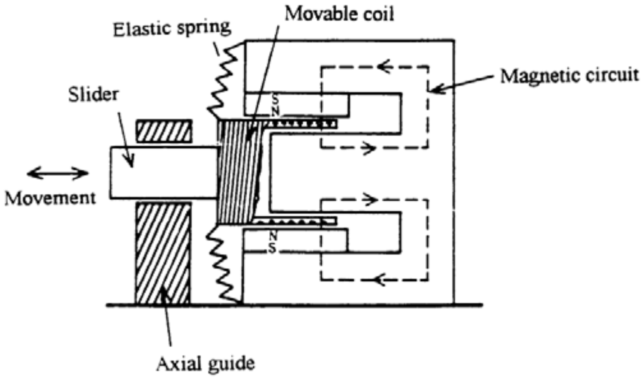

Figure 7 Schematic representation of a voice coil motor.

The search for new solid-state actuators that do not use springs or gear mechanisms has thus developed in recent years to more effectively and reliably provide the displacements required for micropositioning applications. A review of the current technology related to state-of-the-art solid-state actuators is presented in the next section.

3. AN OVERVIEW OF SOLID-STATE ACTUATORS

(1) Smart Actuators

Let us now consider the "smartness" of a material. The various properties relating the input parameters of electric field, magnetic field, stress, heat and light with the output parameters, charge/current, magnetization, strain, temperature and light are listed in Table 2. Conducting and elastic materials, which generate current and strain outputs, respectively, with input, voltage or stress (diagonal couplings), are sometimes referred to as *"trivial" materials*. High temperature superconducting ceramics are also considered trivial materials in this sense, but the figure of merit (electrical conductivity) exhibited by some new compositions has been exceptionally high in recent years making them especially newsworthy.

On the other hand, pyroelectric and piezoelectric materials, which generate an electric field with the input of heat and stress, respectively, are called *smart materials*. These off-diagonal couplings have corresponding converse effects, the electrocaloric and converse piezoelectric effects, so that both "sensing" and "actuating" functions can be realized in the same material. One example is a tooth brace made of a shape memory (super-elastic) alloy. A temperature dependent phase transition in the material responds to variations in the oral temperature, thereby generating a constant stress on the tooth.

"Intelligent" materials must possess a "drive/control" or "processing" function, which is adaptive to changes in environmental conditions in addition to their actuator and sensing functions. Photostrictive actuators belong to this category. Some ferroelectrics generate a high voltage when illuminated (the *photovoltaic effect*). Since the ferroelectric is also piezoelectric, the photovoltage produced will induce a strain in the crystal. Hence, this type of material generates a drive voltage dependent on the intensity of the incident light, which actuates a mechanical response. The self-repairing nature of partially stabilized zirconia can also be considered an intelligent response. Here, the material responds to the stress concentrations produced with the initial development of the microcrack (sensing) by undergoing a local phase transformation in order to reduce the concentrated stress (control) and stop the propagation of the crack (actuation).

If one could incorporate a somewhat more sophisticated mechanism for making complex decisions to its "intelligence," a *wise material* might be created. Such a material might be designed to determine that "this response may cause harm" or "this action will lead to environmental destruction," and respond accordingly. It would be desirable to incorporate such fail-safe mechanisms in actuator devices and systems. A system so equipped would be able to monitor for and detect the symptoms of wear or damage so as to shut itself down safely before serious damage or an accident occurred.

Table 2 Various basic and cross-coupled properties of materials.

OUTPUT INPUT	CHARGE/ CURRENT	MAGNETI-ZATION	STRAIN	TEMPERATURE	LIGHT
ELECTRIC FIELD	Permittivity Conductivity	Electromagnetic Effect	Converse Piezoelectric Effect	Electrocaloric Effect	Electrooptic Effect
MAGNETIC FIELD	Magnetoelectric Effect	Permeability	Magnetostriction	Magnetocaloric Effect	Magnetooptic Effect
STRESS	Piezoelectric Effect	Piezomagnetic Effect	Elastic Constants	****	Photoelastic Effect
HEAT	Pyroelectric Effect	****	Thermal Expansion	Specific Heat	****
LIGHT	Photovoltaic Effect	****	Photostriction	****	Refractive Index

Diagonal Coupling: ▨ **Sensor**: ▭

Off-Diagonal Coupling: Smart Material **Actuator**: ▭

(2) New Actuators

Actuators that operate by means of a mechanism different from those found in the conventional AC/DC electromagnetic motors and oil/air pressure actuators are generally classified as "*new actuators*." Some recently developed new actuators are classified in Table 3 in terms of input parameter. Note that most of the new actuators are made from some type of solid material with properties specifically tailored to optimize the desired actuating function. That is why these actuators are sometimes referred to as just *solid-state actuators*. We will examine in this section some of the most popular and useful types of materials utilized for this class of actuators and their associated properties.

The displacement of an actuator element must be controllable by changes in an external parameter such as temperature, magnetic field or electric field. Actuators activated by changes in temperature generally operate through the *thermal expansion* or dilatation associated with a phase transition, such as the ferroelectric and martensitic transformations. *Shape memory alloys*, such as Nitinol, are of this type. Magnetostrictive materials, such as Terfenol-D, respond to changes in an applied magnetic field. *Piezoelectric* and *electrostrictive* materials are typically used in electric field-controlled actuators. In addition to these, we will consider silicon-based micro-electro-mechanical-systems (MEMS), polymer artificial muscles, light activated actuators (for which the displacements occur through the photostrictive effect or a photoinduced phase transformation), and electro/magnetorheological fluids.

Table 3 New actuators classified in terms of input parameter.

Input Parameter	Actuator Type/Device
Electric Field	Piezoelectric/Electrostrictive Electrostatic (Silicon MEMS) Electrorheological Fluid
Magnetic Field	Magnetostrictive Magnetorheological Fluid
Stress	Rubbertuator
Heat	Shape Memory Alloy Bubble Jet
Light	Photostrictive Laser Light Manipulator
Chemical	Mechanochemical Metal-Hydrite

The desired general features for an actuator element include:

1) large displacement (sensitivity = displacement/ driving power),
2) good positioning reproducibility (low hysteresis),
3) quick response,
4) stable temperature characteristics,
5) low driving energy,
6) large generative force and failure strength,
7) small size and light weight,
8) low degradation/aging in usage,
9) minimal detrimental environmental effects (mechanical noise, electro-magnetic noise, heat generation, etc.).

(3) MEMS: MicroElectromechanical Systems

Silicon has become almost synonymous with integrated electronic circuitry. Due to its favorable mechanical properties, silicon can also be micromachined to create microelectromechanical systems (MEMS).[6] The techniques for micromachining silicon have developed over the past ten years in a variety of industries for a wide range of applications. Pressure and acceleration sensors are produced for application in medical instrumentation and automobiles. One important example is the acceleration sensor used to trigger an air bag in an automobile crash. The generative force/displacement levels produced by MEMS devices are, however, generally too small to be useful for many actuator applications.

In *bulk micromachining*, mechanical structures are fabricated directly on a silicon wafer by selectively removing wafer material. Etching is the primary technique for bulk micromachining, and is either isotropic, anisotropic, or a combination of the two states. The etch rate for anisotropic etching depends on the crystallographic orientation; for example, an anisotropy ratio of 100:1 is possible in the <100> direction relative to the <111> direction. Etch processes can be made selective by using dopants (heavily doped regions etch slowly), or may be halted electrochemically (etching stops in a region of different polarity in a biased p-n junction). After the etching process is complete, the silicon wafer is anodically bonded to Pyrex and finally diced into individual devices. This has been a standard technique for fabricating silicon pressure sensors and micropumps for many years.

Recently, however, *surface micromachining*, *silicon fusion bonding*, and a process called *LIGA* (Lithographie, Galvanoformung, Abformung) have also emerged as major fabrication techniques. Surface micromachining of a wafer involves selectively applying or removing thin film layers. Thin film deposition and wet and dry etching techniques are the primary tools for this. Thin films of polysilicon, silicon oxide, and silicon nitride are used to produce sensing elements, electrical interconnections, and the structural, mask, and sacrificial layers. Silicon epitaxial layers, grown and deposited silicon oxide layers and photoresist are used as sacrificial materials.

A typical surface micromachining process is depicted in Figure 8.[6] A sacrificial layer is applied (grown or deposited) in an appropriate pattern on the wafer and then removed from the areas where a mechanical structure will be attached to the substrate. Then, the mechanical layer is applied and patterned. Finally, the underlying sacrificial layer is etched away to release the mechanical structure. This process can produce structures on a scale of a few hundred micrometers, such as the microgripper appearing in Figure 9. This microgripper was fabricated by Berkeley Sensor and Actuator Center, CA using released-polysilicon suface micromachining and is activated by electrostatic forces.[6]

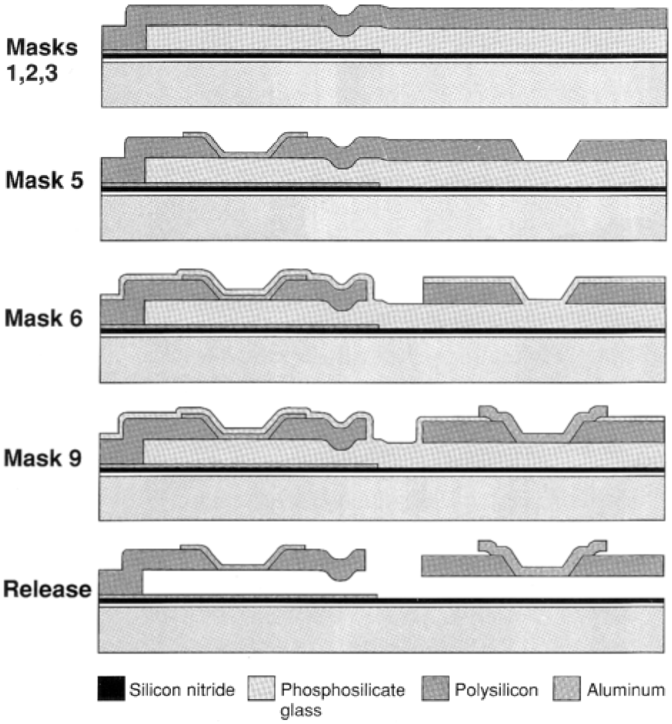

Figure 8 A typical surface micromachining process. The phosphosilicate glass layer is sacrificial in this process.[6]

The first step of the LIGA process involves generating a photoresist pattern on a conductive substrate using deep x-ray lithography. The gaps between the resist patterns can be fully electroplated, yielding a highly accurate negative replica of the original resist pattern. This can be used as a mold for plastic resins such as polyimide and polymethyl methacrylate or for ceramic slurries. Once the material has been cured, the mold is removed, leaving behind microreplicas of the original pattern. An epicyclic microgearbox appears in Figure 10 that is to be fitted onto the micromotor pictured in Figure 6. It contains seventeen microinjection-molded components made from the polymer POM.[5] Note that the chief disadvantage of this process is the need for a short-wavelength, highly collimated x-ray source, ideally a synchrotron. Few MEMS manufacturers can afford their own synchrotron.

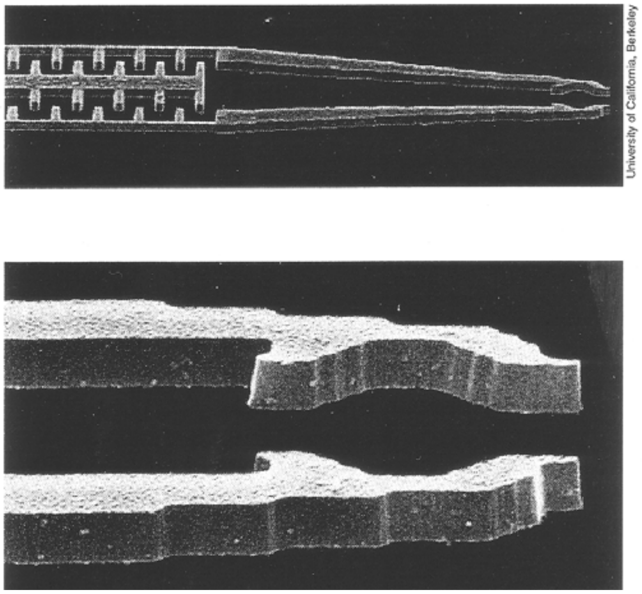

Figure 9 A microgripper fabricated by Berkeley Sensor and Actuator Center, CA using released-polysilicon suface micromachining.[6]

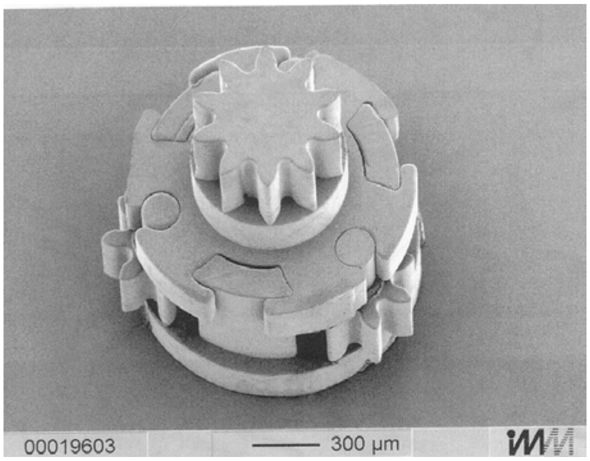

Figure 10 A microgearbox made of polymer POM using a LIGA technique. It will be fitted onto the micromotor pictured in Figure 6.[5]

(4) Artificial Muscle

In a manner similar to the silicon MEMS devices, the operation of polymer film actuators is based on electrostatic principles. The artificial muscle described here, developed at the University of Tokyo, makes use of this type of actuator.[7]

The basic design and operation of the polymer film actuator is depicted in Figure 11. Two polymer films with embedded electrodes are placed adjacent to each other. When three-phase voltages (+V, -V, 0) are applied in succession to every three embedded electrodes in the stator film [Figure 11a], charges of -Q, +Q and 0 are induced on the opposing slider film [Figure 11b]. Then, when the three voltages are switched to –V, +V and –V [Figure 11c], a repulsive force is generated between the stator and slider films, and an attractive force is generated between the adjacent electrodes on the two films. This produces an electrode pitch displacement (in this case a shift of the slider to the right) [Figure 11d]. The electrostatic force generated increases significantly as the electrode gap is reduced.

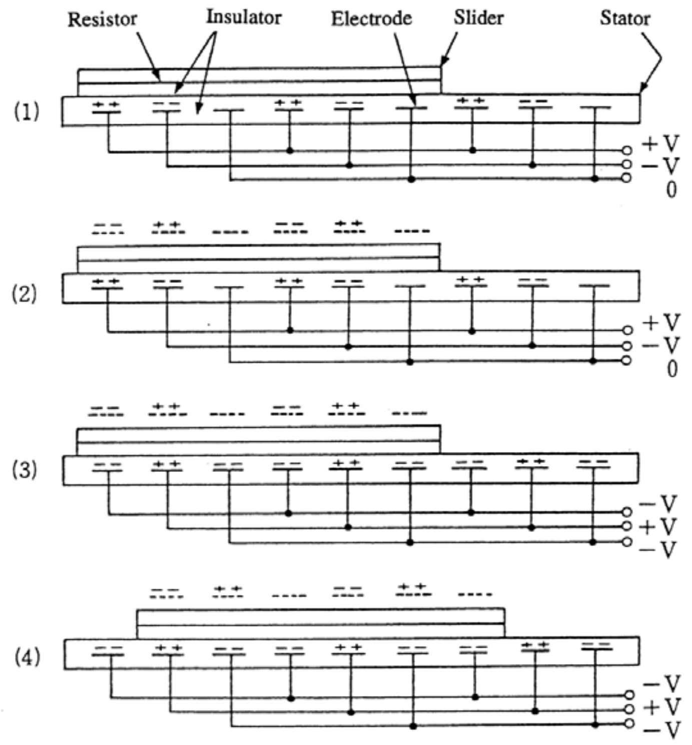

Figure 11 The basic design and operation of a polymer film actuator.[7]

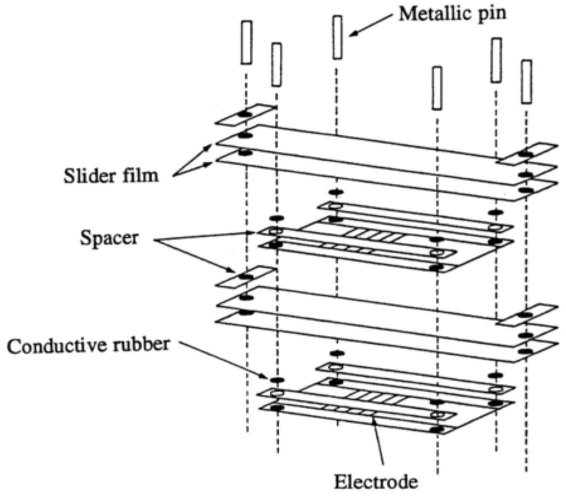

Figure 12 Construction of the electrostatic polymer artificial muscle.[7]

The construction of the electrostatic polymer artificial muscle is illustrated in Figure 12. A thin film of PET, 12 μm in thickness, is used for the slider, to which a polyimide film with surface line electrodes is laminated which serves as the stator. Spacers are included in the structure as shown to maintain the proper separation between electroded surfaces. Five stator/slider pairs, 34 mm in width and 80 mm in length, are stacked together with a 0.35 mm gap between them. The prototype structure, which weighs 43 g is then dipped into "Fluorinat (3M)." When three-phase voltage at 10 Hz is applied with a pitch range of 0.1–1.0 mm, a speed of 1 m/sec is achieved without load. A propulsive force (thrust) of 1–3 N is possible with an applied root-mean-square voltage of 2.5 kV. The relatively high voltage required for operation is a major drawback of this artificial muscle.

A robot arm driven by the electrostatic artificial muscles is shown in Figure 13. A 40-layer electrostatic actuator (generating 320 N) works in conjunction with a 20-layer actuator (generating 160 N) via a pulley mechanism.[8]

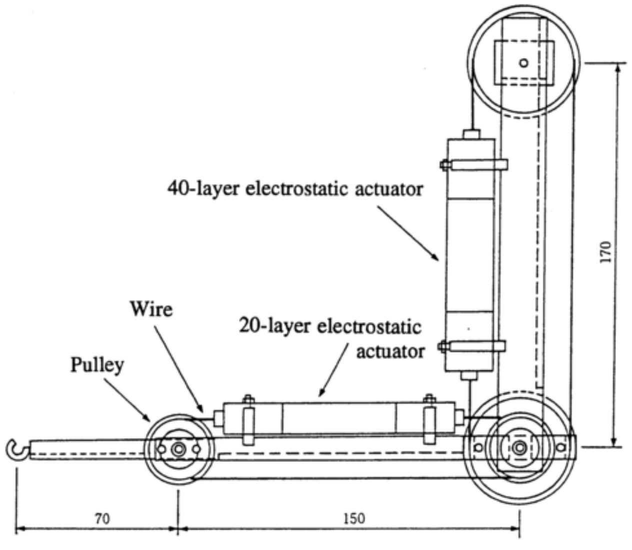

Figure 13 Schematic representation of a robot arm incorporating two artificial muscles.[8]

(5) Shape Memory Alloys

Many materials exhibit large mechanical deformations when undergoing a structural phase transition. This phase transition may be induced by temperature, stress, or electric field. In some materials, once the mechanical deformation is induced, some deformation may be retained with the release of the load and applied stress, but the original form may be restored with the application of heat. This type of action is called *shape memory*.

The stress versus strain curves for typical shape memory and super-elastic alloys and a normal metal are shown in Figure 14.[9] When the stress applied to a normal metal exceeds the elastic limit, irreversible (non-recoverable) plastic deformation results. A super-elastic alloy subjected to the same level of stress, on the other hand, will become elastically soft at a level beyond the elastic deformation limit, due to a stress-induced phase transformation. The deformation that occurs in this case, however, is reversible and the original form is recovered as the load is removed and the stress is released. Finally, we see in the case of the shape memory alloy, a response quite similar to the normal metal except that for these materials the original form may be recovered after the load has been removed by heating the alloy at the appropriate temperature.

Depending on the temperature at which it is deformed, a shape memory alloy may exhibit one of two different types of mechanical behavior: *superelastic* or *pseudoplastic*. When Nitinol (a Ni-Ti alloy) is behaving as a *superelastic* material, reversible deformation of up to 10% may be obtained with a very small effective modulus, which is several orders of magnitude smaller than the modulus of the parent phase. When the material is *pseudoplastic*, the deformation occurs with some slight hardening accompanied by very large strains. The pseudoplastically deformed alloy can then be restored to its initial shape by heating. The generative force may be as high as 10^8 N/m^2 during the recovery process.

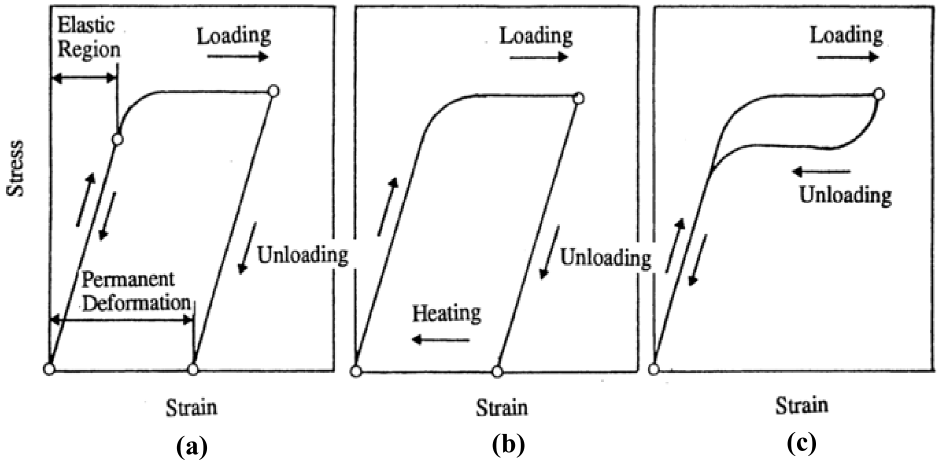

Figure 14 Typical stress versus strain curves for: (a) normal, (b) shape memory, and (c) super-elastic materials.[9]

The *shape memory* and *superelastic* mechanisms are considered from a crystallographic viewpoint in Figure 15.[10] In a normal metal, atomic shifts occur above a certain critical stress, leading to a shear strain, which remains as a permanent residual strain even after the stress is removed [Figure 15(a)]. In a shape memory alloy, a *Martensitic phase transformation* occurs under these conditions; if the parent phase (Austenite) is below the transition temperature, the Martensite phase will be induced. Macroscopically the material will retain the same shape, but on a microscopic level many twin structures will have been generated. Since the twin planes are easily moved, the Martensite material is readily deformed by the external stress [Figure 15(b)]. However, when the deformed material is heated to a temperature higher than the reverse phase transition temperature, A_f, the parent phase (*Austenite*) is induced and the initial shape is recovered. This is the *shape memory effect*. If stress is applied to a shape memory alloy above the transition temperature, A_f, (that is, in the Austenite phase), above a certain stress level the Martensite phase is induced gradually, leading to a pseudo-plastic response. The material is very compliant under these conditions. As the applied stress is decreased, the reverse phase transformation (Martensite to Austenite) occurs and the material returns to its original elastically stiff state. This elastic phenomenon, which is similar to what is observed for rubber, is called *superelasticity*.

Interestingly, one of the first commercial successes involving the shape memory alloy was in women's lingerie. One brassiere design incorporating the alloy exploited the material's superelastic properties to help maintain a comfortable fit while providing adequate support. Another big market has been for pipe couplers and electrical connectors.[11] The couplings are made by machining a cylinder of the alloy while it is in the Austenite phase, usually with circumferential sealing bands on the inner diameter. A second, slightly wider cylinder is then inserted into the shape memory cylinder as it cools in order to force it to expand as the material transforms to the Martensite phase. When the coupling is brought back to room temperature, the outer cylinder contracts as it reverts to the Austenite phase, tightly clamping the inner cylinder.

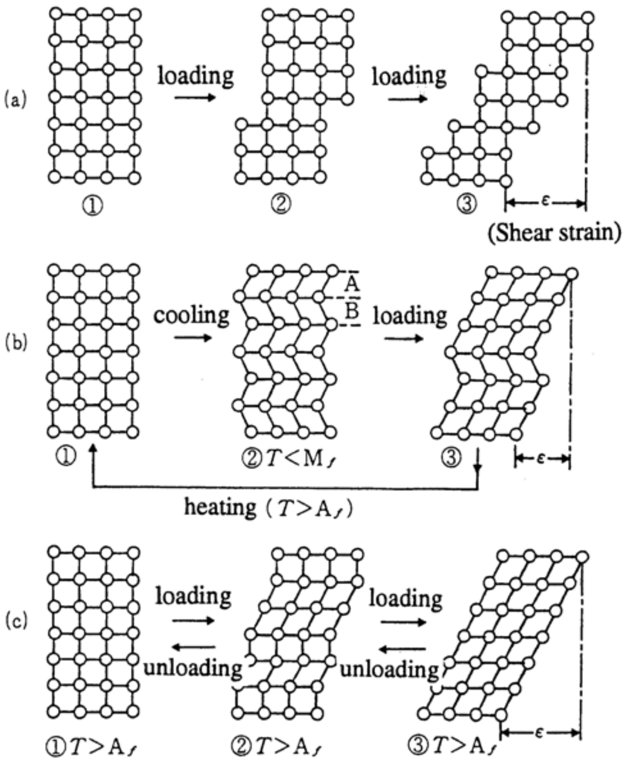

Figure 15 Microscopic lattice distortions for: (a) normal, (b) shape memory, and (c) super-elastic metals.[10]

An actuator incorporating a shape memory spring is shown in Figure 16. A normal steel spring and a shape memory alloy (Ni-Ti or Nitinol) spring, which will "remember" its fully extended form, are included in the design. At low operating temperatures, the shaft will be pushed to the right as the shape memory spring becomes soft. When the temperature is raised (for example, by means of an electric current), the spring constant of the shape memory actuator will increase significantly, causing the shaft to be pushed to the left.

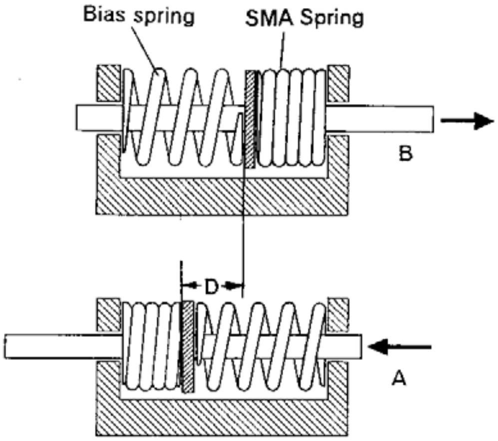

Figure 16 A two-way actuator incorporating shape memory alloy (SMA) and normal metal (Bias) springs.

A similar mechanism is utilized in the flapper control unit for an air conditioning system. The temperature of the air passing from the air conditioner is constantly changing and can sometimes become uncomfortably cold. One solution to this problem is to adjust the air flow direction using a flap mounted on the front of the air conditioner that is actuated by a shape memory alloy as shown in Figure 17.[12] When the flowing air is cold, the flap will move so as to direct the air upward, and when the air temperature exceeds body temperature, it will move so as to direct the air downward. The link mechanism and the rocking motion of the flap are illustrated in Figure 17(a). The shape memory spring and bias spring act on the ends of the flapper to swing it like a seesaw about the pivot, thus redirecting the air flow as the temperature changes.

(6) Magnetostrictive Actuators

Magnetostrictive materials convert magnetic energy into mechanical energy and vice versa. A magnetostrictive material becomes strained when it is magnetized. Conversely, when either an applied force or torque produces a strain in a magnetostrictive material, the material's magnetic state (magnetization and permeability) will change.

Magnetostriction is an inherent material property that depends on electron spin, the orientation and interaction of spin orbitals, and the molecular lattice configuration. It is also affected by domain wall motion and rotation of the magnetization under the influence of an applied magnetic field or stress.[13]

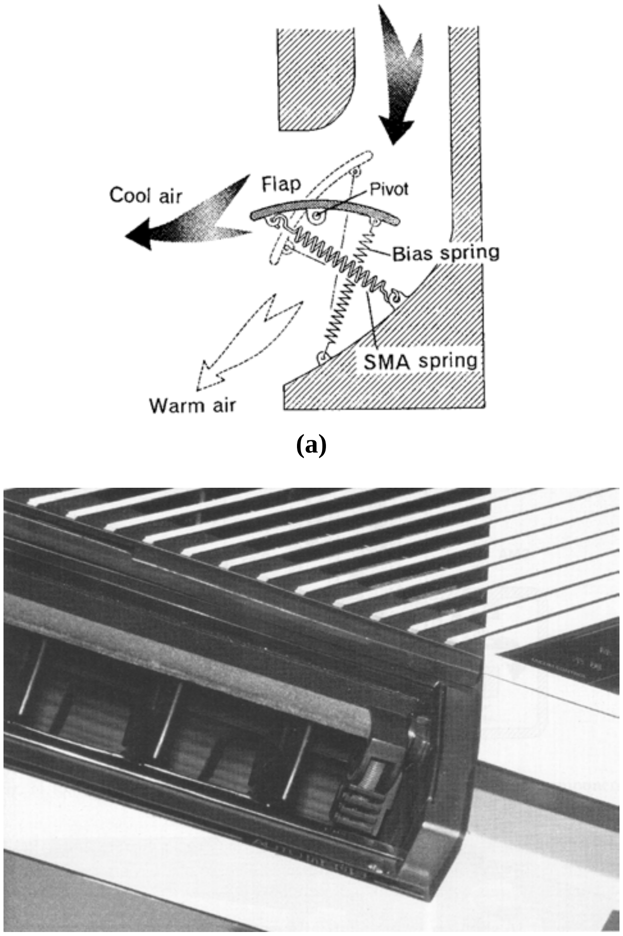

(a)

(b)

Figure 17 An air conditioning system with a shape memory flapper control mechanism: **(a)** schematic representation of the flapper control mechanism and **(b)** the flapper control unit as it appears in an actual air conditioner.[12]

Research on giant magnetostriction began with studies on Terfenol-D (a Tb-Dy-Fe alloy) conducted by Clark et al.[14] Longitudinally and transversely induced strain curves at various temperatures for Terfenol-D appear in Figure 18. The domain wall motion induced with the application of a small magnetic field occurs due to the growth of domains having magnetization aligned with the applied field, at the expense of domains with magnetization opposing the field. At moderate field strengths, the magnetic moments within unfavorably oriented domains overcome the anisotropy energy and suddenly rotate such that one of their crystallographic easy axes is more closely aligned with the external field direction. This sudden rotation is generally accompanied by a large change in strain. As the field is increased further, the magnetic moments undergo coherent rotation until they are completely aligned with the applied field. At this point the material is single-domain and the strain curve becomes saturated.

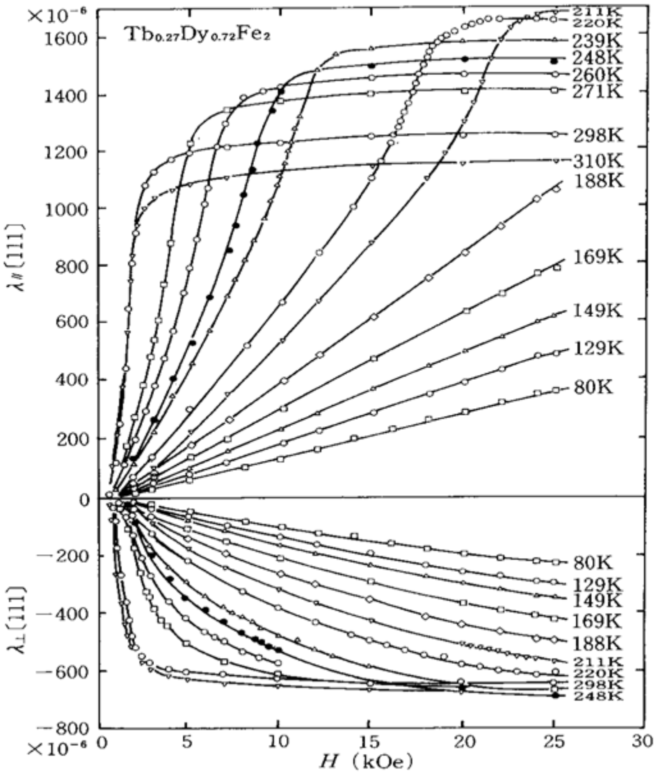

Figure 18 Longitudinally and transversely induced strains in Terfenol-D at various temperatures.[14]

Although one can attain strains exceeding 0.17 % and sufficiently large generative stresses with magnetostrictive materials of this type, problems similar to those encountered with electromagnetic motors arise. These are related to the need for a magnetic coil and high field strengths to drive the devices. A typical design for a giant magnetostrictive actuator is depicted in Figure 19.[15] Two noteworthy features of this actuator are the pre-stressing mechanism and the magnetic coil and shield, which significantly increase the overall volume and weight of the system. The extensional pre-stress is important for optimum performance of the magnetostrictive alloy, and in some cases, a bias magnetic field must be maintained because the induced strain tends to be rather insensitive to the external field at low field strengths.

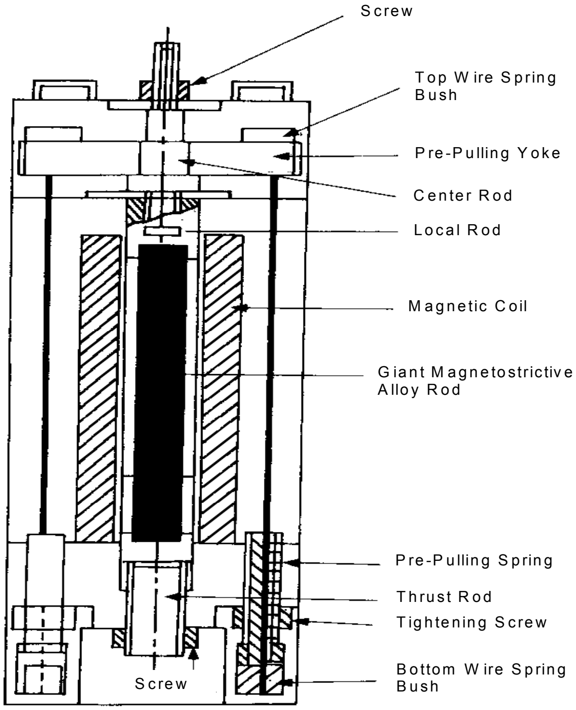

Figure 19 A typical design for a giant magnetostrictive actuator.[15]

The sonar device depicted in Figure 20 includes a square array of four magnetostrictive (Terfenol-D) rods mounted in a metal ring.[16] The magnetostrictive rods are 6 mm in diameter and 50 mm in length, and have a free resonance frequency of 7.4 kHz. The resonance frequency of the entire ring device is 2.0 kHz.

In general, magnetostrictive actuators such as these are bulky due to the magnetic coil and shield required for their operation, and, hence, are difficult to miniaturize. On the other hand, since they can generate relatively large forces and their efficiency increases with increasing size, they tend to be especially suitable for applications often reserved for electromagnetic motors, such as in construction/demolition machines and for vibration control in large structures. Another intriguing application can be found in surgery, where miniature magnetostrictive actuators, controlled with external magnetic fields provided by means of technology similar to what is currently used in MRI machines, can be used for specialized procedures.

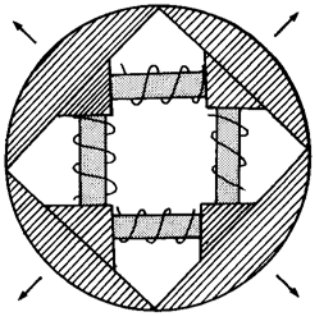

Figure 20 A high power acoustic transducer incorporating four magneto-strictive actuators.[16]

(7) Piezoelectric/Electrostrictive Actuators

When an electric field is applied to an insulating material, strain will be induced in the material either through the piezoelectric effect, electrostriction, or a combination of the two effects. The *converse piezoelectric effect* is a primary electromechanical effect, where the induced strain is proportional to the applied electric field, while the electrostrictive effect is a secondary phenomenon, whereby the induced strain is proportional to the square of the applied field. A brief introduction to this class of devices is given here. A more thorough description of the piezoelectric effect and electrostriction will be presented in the next chapter.

Electric field-induced strain curves are shown for piezoelectric lanthanum-doped lead zirconate titanate (PLZT) and electrostrictive lead magnesium niobate (PMN)-based ceramics in Figure 21.[17] The piezoelectric response shows the characteristic linear strain versus field relation with a noticeable hysteresis, while the electrostrictive response exhibits no hysteresis and a non-linear relation between the induced strain and the applied electric field is apparent. Due to this non-linear behavior, a sophisticated drive circuit is generally needed for electrostrictive actuators. Note that the maximum strain and stress levels for the piezoelectric ceramics are around 0.1 % and 4 x 10^7 N/m^2, respectively.

Among all the solid-state varieties, piezoelectric actuators have undergone the most advanced development and remain the most commonly employed type for many applications at this time. The dot matrix printer head pictured in Figure 22, which operates by means of a multilayer piezoelectric actuator with sophisticated displacement amplification mechanisms, is one earlier application that was commercialized by NEC of Japan in 1987.[18]

Piezoelectric ultrasonic motors have also been developed intensively. Electronic component industries have currently focused their attention on the development of these devices, mainly because the piezoelectric motors offer distinct advantages of superior efficiency, miniature size (5-8 mm), and ease of manufacturing over conventional electromagnetic motors. Microultrasonic motors developed and commercialized by SEIKO Instruments, Japan for wristwatch applications appear in Figure 23.[19] The 8 mm diameter motor is used as a silent alarm, and the 4 mm diameter motor is part of a date change mechanism.

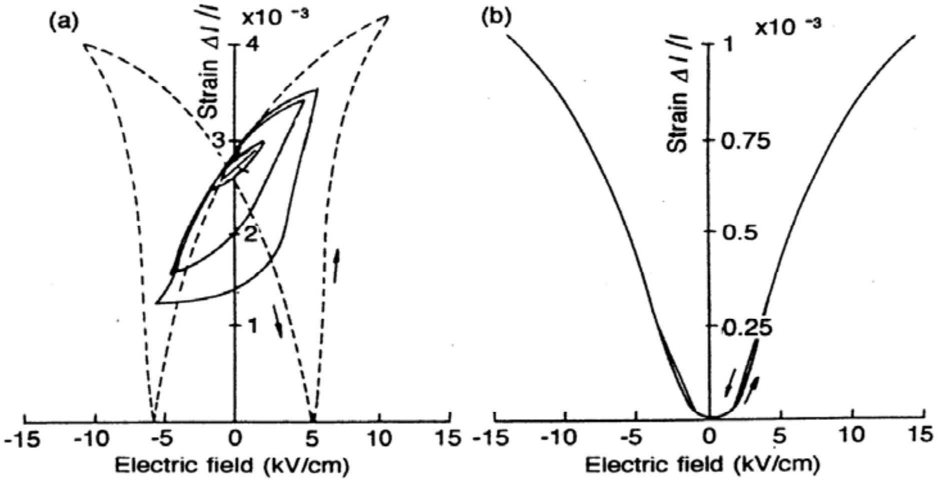

Figure 21 Electric field-induced strains in (a) piezoelectric lanthanum-doped lead zirconate titanate, and (b) electrostrictive lead magnesium niobate-based ceramics.[17]

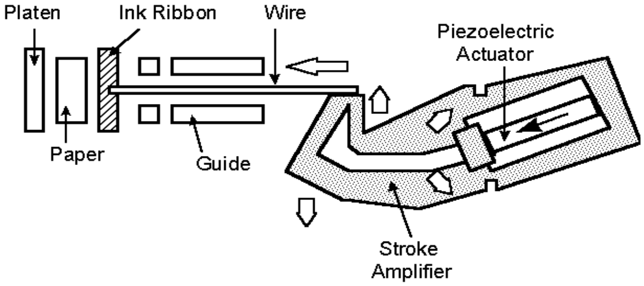

Figure 22 A dot matrix printer head incorporating a multilayer piezoelectric actuator and a hinge-lever type displacement amplification mechanism (NEC, Japan).[18]

Figure 23 Micro-ultrasonic motors utilized for silent alarm (8 mm diameter, left-side) and date change (4 mm diameter, right-side) mechanisms in a wristwatch (SEIKO, Japan).[19]

(8) Polymer/Elastomer Actuators

Large strains can be generated in polymer materials without causing mechanical damage because of their high elastic compliance. Polymer actuator materials can be classified according to two general types: *polyvinylidene difluoride (PVDF)-based piezoelectric polymers* and *electret/elastomer* types.

Copolymers from the system polyvinylidene difluoride trifluoroethylene [P(VDF-TrFE)] are well-known as piezoelectric materials. The strain induced in these materials is not very large, however, due to the very high coercive field. An electron irradiation treatment has been applied to materials from this system by Zhang et al. which significantly enhances the magnitude of the induced strain.[20] A 68/32 mole percent P(VDF-TrFE) copolymer film is irradiated by a 1.0 MeV electron beam at 105°C. The 70 Mrad exposure results in a diffuse phase transition and a decrease in the transition temperature as compared with the non-irradiated material. It is believed that the observed changes in the phase transition are due to the development of a microdomain state, similar to that associated with relaxor ferroelectrics, which effectively interrupts the long-range coupling of ferroelectric domains. The strain curve pictured in Figure 24 for an irradiated P(VDF-TrFE) specimen demonstrates that induced strains as high as 5% are possible with an applied field strength of 150 MV/m.

Elastomer actuators operate through the *Maxwell force* that occurs in an electrostatic capacitor. Considering a capacitor with an area, S, and electrode gap, t, filled with a dielectric material with a dielectric constant, K, the capacitance, C, and the stored energy, U, will be given by:

$$C = \varepsilon_o K\,(S/t), \tag{1}$$

$$U = (1/2)CV^2 \tag{2}$$

Note that an attractive force described by

$$F = \left(\partial U / \partial t \right) = - (1/2)\, \varepsilon_o \kappa\, S(V/t)^2 \qquad (3)$$

will be induced between the electrodes, which will lead to a decrease in the inter-electrode distance. Hence, we see that a larger displacement can be obtained by increasing the elastic compliance and the effective permittivity (and, therefore, the stored electric charge) of the material. A hybrid elastomer structure has been developed whereby a porous PTFE and a stiff PFCB phase are incorporated in the configuration depicted in Figure 25.[21] The stiffer PFCB phase serves to store the charge while the porous PTFE phase effectively increases the overall compliance of the structure. An effective piezoelectric d_{33} strain coefficient of around 600 pC/N, has been obtained for this composite structure, which is 20 times larger than that obtained for pure PVDF. In theory, one can reasonably predict a strain level as high as 100% (a twofold enhancement) for this material when a sufficiently soft polymer is used as the porous phase. It is important to note that even though one might feasibly anticipate large displacements for a polymer, they will be realized only at the expense of the generative force and responsivity of the device.

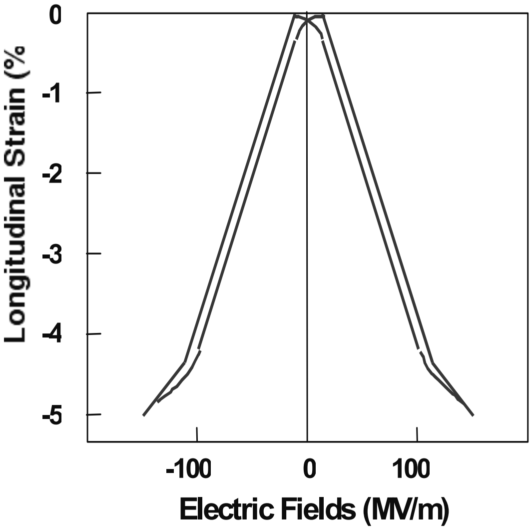

Figure 24 The electric field-induced strain curve for an irradiated polyvinylidene difluoride-based copolymer.[21]

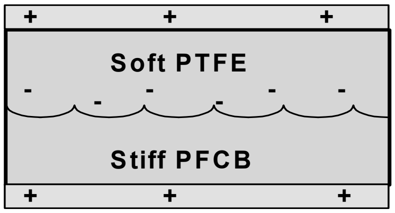

Figure 25 Schematic representation of a hybrid elastomer structure incorporating a porous PTFE and a stiff PFCB phase.[21]

(9) Photostriction

The ongoing emphasis on miniaturization and the integration of microrobotics and microelectronics has resulted in significant development of new ceramic actuators. Those utilizing wavelength-dependent optical actuation mechanisms are especially attractive at this time. *Photostrictive actuators*, which convert the photonic energy into mechanical motion, are of interest for their potential use in microactuation and microsensing applications. Optical actuators are also attractive for use as the driving component in optically controlled electromagnetic noise-free systems. The photostrictive effect has also been used recently for a photophonic device, in which light is transformed into sound through the mechanical vibration induced by intermittent illumination.

In principle, the *photostrictive effect* arises from a superposition of the photovoltaic effect (the generation of a potential difference in response to illumination), and the converse piezoelectric effect (strain induce by an applied electric field).[22] The photostrictive effect has been studied mainly in ferroelectric polycrystalline materials. Lanthanum-modified lead zirconate titanate (PLZT) ceramic is one of the most promising photostrictive materials due to its relatively high piezoelectric coefficient and ease of fabrication. The origin of the photovoltaic effect in (PLZT) is not yet clear, although several models for possible mechanisms have been proposed. Key issues in understanding the mechanisms behind the effect are both impurity doping and crystal asymmetry. One model has been proposed that describes the effect in terms of the electron energy band structure for PLZT ceramics.[23] According to this model, the donor impurity level associated with the lanthanum doping will occur slightly above the valence band as depicted in Figure 26. The asymmetric potential due to crystallographic anisotropy is expected to facilitate the transition of the electron between these levels by providing it with *preferred momentum*. An asymmetric crystal exhibiting a photovoltaic response should also be piezoelectric and, therefore, a photostrictive response is also expected through the coupling of the two effects.

Application of the photostriction effect has been demonstrated with the PLZT ceramic photo-driven relay and microwalking devices developed by Uchino et al.[24] These devices are activated entirely by the incident light and require no drive circuitry.

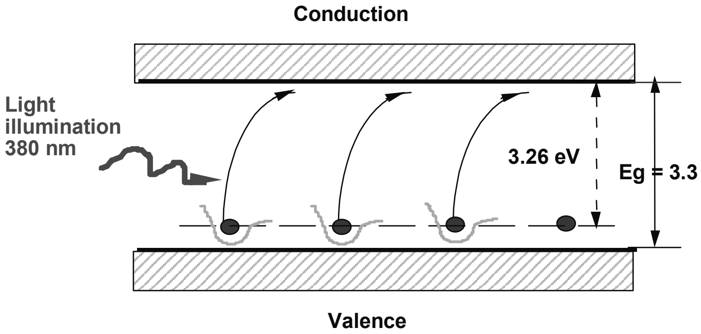

Figure 26 A current source model for the photovoltatic effect in PLZT.[23]

Recently, a new application for highly efficient photostrictive PLZT films on flexible substrates has been proposed for use in a new class of small exploratory land vehicles for future space missions.[25] The original π-shaped design of the micro-walking device can be modified to assume the arch shape pictured in Figure 27. It is comprised of a photoactuating composite film, similar to that conventionally used for unimorphs, fabricated in the form of an arch on which the triangular top piece is attached. The device executes the motion depicted in the figure when illuminated. Optimum photostrictive response has been observed for devices incorporating PLZT films approximately 30 μm in thickness. The device is driven at resonance with chopped illumination. Photomechanical resonance has been demonstrated in a PLZT bimorph.[26] Photoactuating films have been produced from PLZT solutions and applied to one side of a suitable flexible substrate designed to assume a curvature of 1 cm^{-1}. The walking device is designed to have a small difference in length between the right and left legs in order to establish a slight difference between their resonance frequencies. A chopped light source operating near these resonance frequencies is used to illuminate the device in order to induce the optimum vibration of the bimorph. Rotation of the walker in either the clockwise or counterclockwise directions is achieved by tuning the source to match the resonance frequency of one or the other leg.

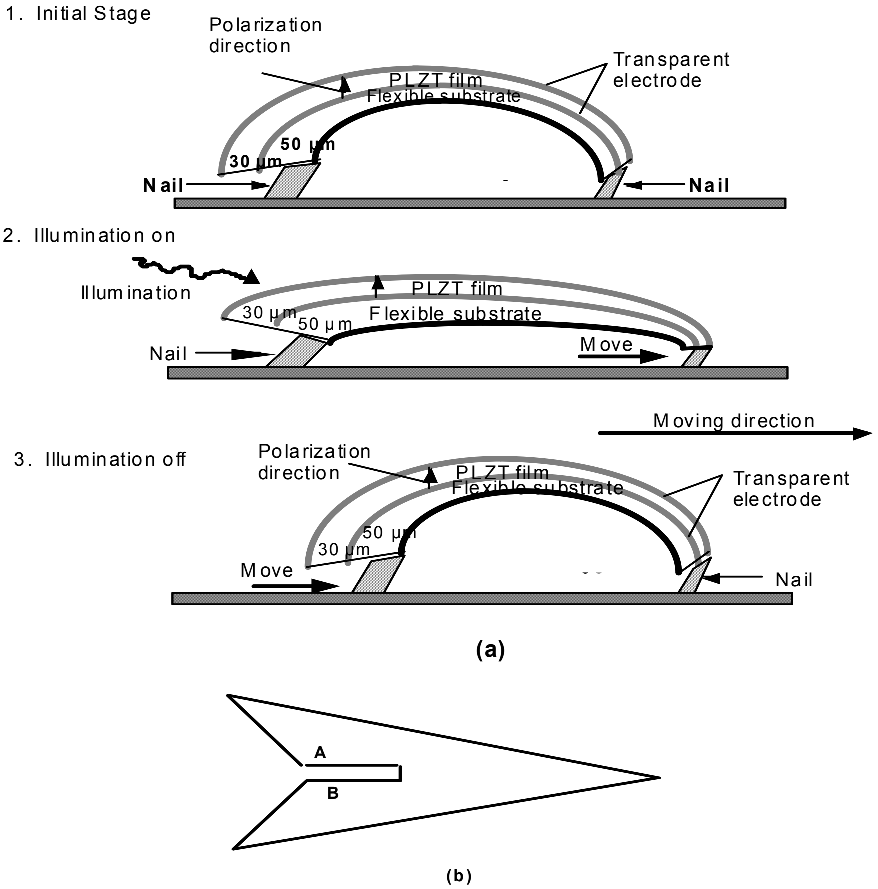

Figure 27 Schematic representation of an arch-shaped photoactuating film device: (a) action sequence and (b) the triangular top piece.[25]

(10) Electro/magnetorheological Fluids

Composite materials whose rheological properties can be changed with the application of an electric or a magnetic field are referred to as *electrorheological* (ER) or *magnetorheological* (MR) materials, respectively. The ER and MR materials are generally in the liquid state. The rheological state of such fluids is affected when dipoles are induced in the suspension by the applied field. The dipoles interact to form columnar structures parallel to the applied field as depicted in Figure 28. These chain-like structures restrict the flow of the fluid, thereby increasing the viscosity of the suspension.

Electrorheological (ER) fluids are composed of electrically polarizable particles suspended in an insulating medium. Ferroelectric particles, such as barium titanate and strontium titanate, are typically used in ER fluids because they have relatively high dielectric constants. On the other hand, magnetorheological (MR) fluids have a high concentration of magnetizable particles in a nonmagnetic medium. Spherical iron particles obtained from the thermal decomposition of iron pentacarbonyl are commonly used.[27]

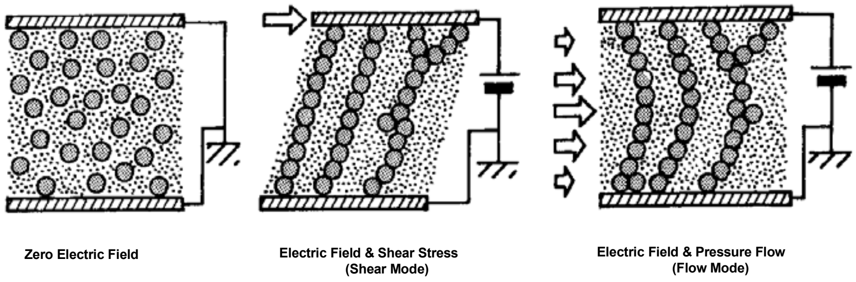

Zero Electric Field

Electric Field & Shear Stress
(Shear Mode)

Electric Field & Pressure Flow
(Flow Mode)

Figure 28 Schematic representation of the response of an electrorheological fluid to applied electric field and stress.

The properties of typical ER and MR fluids are summarized in Table 4. In general, ER and MR fluids are almost identical in terms of their rheological characteristics. However, from a production point of view, the MR fluid is preferred over the ER variety, because its properties are less affected by impurities.

Table 4 Properties of typical ER and MR fluids.

Property	ER Fluid	MR Fluid
Maximum Yield Strength	2-5 (kPa)	50-100 (kPa)
Maximum Field	4 (kV/mm)	250 (kN/Am)
Plastic Viscosity	0.1-1.0 (Pa-s)	0.1-1.0 (Pa-s)
Temperature Range	+10–90 (^{o}C) [dc] -10–125 (^{o}C) [ac]	-40–150 (^{o}C)
Response Time	msec	msec
Density	1-2 (g/cm^{3})	3-4 (g/cm^{3})
Maximum Energy Density	0.001 (J/cm^{3})	0. 1 (J/cm^{3})
Typical Power Supply	2-5 (kV)/1-10 (mA)	2-25 (kV)/1-2 (mA)
Impurity Sensitivity	intolerant	unaffected

The yield stress and apparent viscosity of the fluids increase with the applied field because the mechanical energy required to induce and to maintain these chain-like structures increases with increasing field strength. The storage modulus is plotted as a function of applied electric field for silicone elastomers containing 20-30% iron in Figure 29.[28] These elastomers exhibit significant variations in modulus with increasing electric field. The shear storage modulus was also found to be dependent on the alignment of the particles in the elastomer.

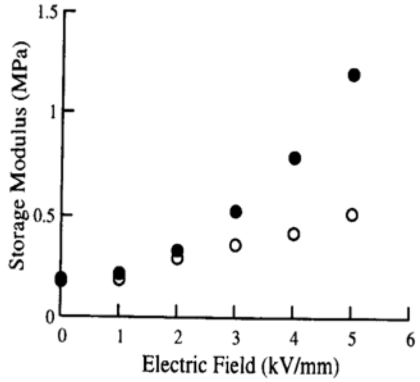

Figure 29 The storage modulus plotted as a function of applied electric field for silicone elastomers containing 20-30% iron.[28] [Random (o) and Aligned (●) particle orientation states]

The basic modes of operation for ER and MR fluids are illustrated in Figure 30. Magnetorheological fluid foam dampers are effective and exhibit long life. Little wear of the foam matrix occurs as the stresses are carried by the field-induced chain structure of iron particles in the MR fluid. A caliper type MR fluid brake design is depicted in Figure 31. Rather than a fully enclosed housing, the absorbent foam filled with MR fluid is attached to the pole faces of the steel yoke. These magnetorheological fluid-based devices have been successfully commercialized for use in exercise equipment[29] and in vehicle seat vibration control.[30]

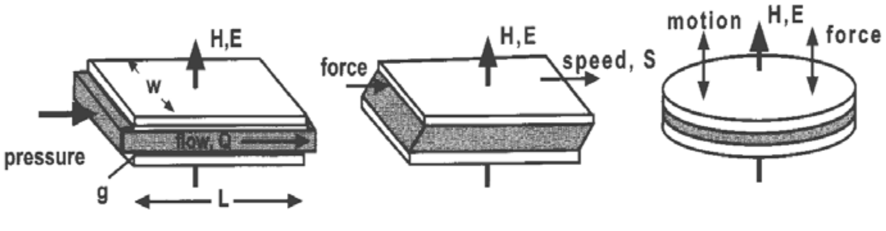

(a) **(b)** **(c)**

Figure 30 Basic modes of operation for ER and MR fluids: (a) valve mode, (b) direct shear mode, and (c) squeeze mode.

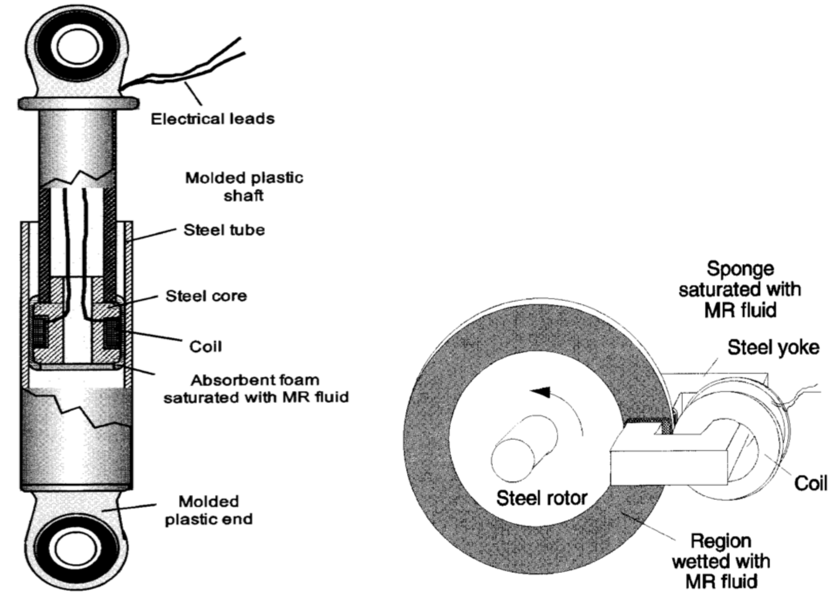

Figure 31 Construction of two simple, low cost magnetorheological (MR) foam devices: (a) a vibration damper[30] and (b) a rotary caliper brake[29]. (Lord Corp.)

(11) Comparison among the Solid-State Actuators

The specifications for shape memory, magnetostrictive, piezoelectric and electrostrictive actuators are listed in Table 5. Certain characteristic features of each type become evident upon examining these data. The *shape memory actuators*, which operate in response to a temperature change, require a relatively large amount of input energy and typically have rather slow response speeds. A flat strip of Ni-Ti alloy, which alternates in form between an arc shape and an unbent strip to transfer energy to a spring, however, can be deformed repeatedly by heating and cooling via an electric current.

The magnetostrictive actuator likewise demonstrates some advantages and disadvantages. Although some magnetic alloys (such as Terfenol-D) may exhibit relatively large induced strains, more commonly, the strain induced in this class of actuator is small. An additional drawback to this variety is the need for a driving coil, which in many applications can be troublesome; Joule heating is inevitable, and magnetic field leakage prevents it from being used adjacent to an operational amplifier or some other type of integrated circuit.

On the other hand, piezoelectric strain and electrostriction is induced by an electric field, and relatively large strains can be obtained in a variety of materials. Hence, the *piezoelectric* and *electrostrictive actuators* are considered the most promising. Lead zirconate titanate (PZT)-based piezoelectric ceramics are most commonly used due to their availability, linear characteristics, low driving energy (low permittivity), and temperature stability at room temperature, as compared to the electrostrictive devices. Electrostrictive actuators are preferred for applications where there may be significant temperature variations (such as experienced by components used on the space shuttle) or high stress conditions (as occur for cutting machine devices). In terms of their reliability, electrostrictive materials are considered better than piezoelectrics in these cases, because they exhibit significantly less degradation and aging under severe conditions.

Table 5 Specifications for shape memory, magnetostrictive, piezoelectric and electrostrictive actuators.

	Shape Memory	Magnetostrictive	Piezoelectric	Electrostrictive
Strain ($\Delta l/ l$)	10^{-3}-10^{-2}	10^{-4}-10^{-3}	10^{-3}-10^{-2}	10^{-4}-10^{-3}
Hysteresis	Large	Large	Large	Small
Aging	Large	Small	Large	Small
Response	sec	μsec	msec	μsec
Drive Source	Heat	Magnetic Coil	Electric Field	Electric Field

4. CRITICAL DESIGN CONCEPTS

(1) Design Concepts Involving Smart Actuators

The performance of smart actuators is dependent on complex factors, which can be divided into three major categories: (1) the material properties, (2) the device design, and (3) the drive technique. The devices and systems to be presented in the following chapters will be described and characterized in terms of these primary factors.

In order to illustrate the significance of these factors with regard to the design of a device or system, let us focus for the moment just on piezoelectric devices. One material-related concern of primary importance will be the optimization of the piezoceramic or single crystal composition, which may involve the incorporation of dopants. The orientation of a single crystal material is also of importance. Control of material parameters such as these are necessary in order to optimize the strains induced under high stroke level drive and to stabilize temperature and external stress dependences. The design determines to a large extent the performance, durability, and lifetime of the device. The inclusion of some failure detection or "health" monitoring mechanism in the actuator is expected to increase its reliability significantly. When considering drive techniques, the pulse drive and ac drive modes require special attention. The vibration overshoot that occurs after applying an abrupt leading edge step/pulse voltage to the actuator will cause a large tensile force and a sustained applied AC voltage will generate considerable heat within the device. The product of such a design will be one for which all of these parameters have been optimized.

(2) Future Trends of Smart Actuators

Much of the current interest in ceramic actuators stems from the development of smart materials and structures. The evolution of this family of materials is gradually progressing through stages ranging from trivial functionality to *smart* to *intelligent* and finally to a more "*wise*" mode of operation. As already discussed, the off-diagonal couplings listed in Table 2 all have corresponding converse effects (such as, the piezoelectric and converse-piezoelectric effects) so that both "sensing" and "actuating" functions can be realized in the same materials. One example of such a material is that employed in the electronic modulated automobile shock absorber developed by

Toyota Motors, which is pictured in Figure 32.[31] The sensor used to detect the road roughness and the actuator used to modify the valve position to change the shock absorbing rate are both multilayer piezoelectric devices. The soft absorbing mode of operation provides the comfortable ride one expects in a vehicle such as a luxury limousine, while the hard absorbing mode provides the good steering control one might desire in a truck or sport utility vehicle. This smart suspension system can also provide both controllability and comfort simultaneously, depending on road conditions.

Mohandas Gandhi, a famous Indian leader, compiled the "The Seven Blunders of the World," in which we find very important principles that also apply in developing new devices. "Science without Humanity" is one of them. We have referred to the fact that in the future we may need to incorporate fail-safe mechanisms or some other "wise" function in our devices or systems to determine whether "this response may cause harm to humans" or "this action will lead to environmental destruction," and to respond accordingly.

In addition to the fail-safe mechanisms referred to earlier in this chapter, we can consider this idea of a "wise" system in a somewhat broader sense. Not long ago, the author met an enthusiastic, middle-aged researcher in Tokyo. He was working on a piezoelectric actuator system for artificial insemination and proudly declared that their system could impregnate cows precisely and quickly, at the rate of some two hundred per hour. One question that might come to mind in considering such a system is: What are the moral/ethical implications of this sort of mass production of cows? While some may recognize that this system for artificial insemination has some utility in agriculture and might even potentially be of vital importance to humans who can conceive by no other means, others may regard it as morally or ethically unacceptable. Thus, in addition to the good, practical considerations that arise in designing and implementing a new system, moral and ethical concerns may also need to be considered for certain applications. Even if the appropriate "wise" function is not actually incorporated in a given device or system, one would hope that the wisdom of the designer(s) would ultimately prevail in situations where such issues apply.

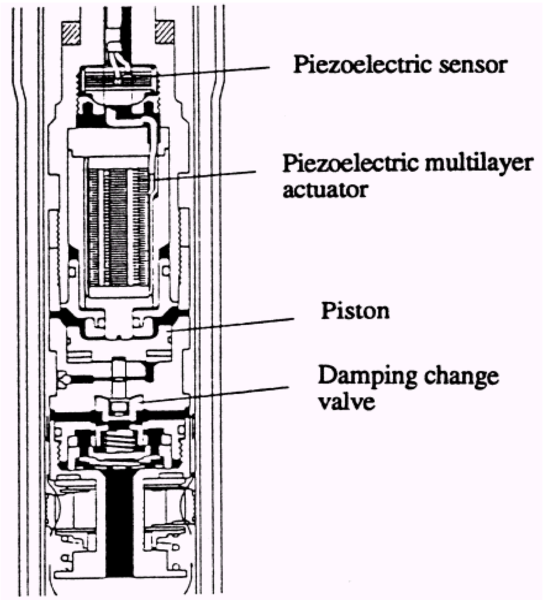

Figure 32 An electronic modulated automobile shock absorber developed by Toyota Motors using a both a multilayer piezoelectric sensor and actuator.[31]

REFERENCES

1) I. Inazaki: Sensor Technology **2**, No.2, 65 (1982).
2) K. Uchino: Ultrasonic Techno, No. 8, 19 (1993).
3) Optical Spectra, March, p.46 (1979).
4) S. Moriyama: Mechanical Design **27**, No.1, 32 (1983).
5) U. Berg, M. Begemann, B. Hagemann, K.-P. –Kamper, F. Michel, C. Thurigen, L. Weber and Th. Wittig: *Proc. 6th Int'l Conf. New Actuators*, p.552 (1998).
6) J. Bryzek, K. Petersen and W. McCulley: IEEE Spectrum, No. 5, p.20 (1994).
7) S. Egawa, T. Niino and T. Higuchi: *Proc. 1991 IEEE Workshop on Micro Electro Mechanical Systems*, p.9 (1991).
8) T. Higuchi: *New Actuator Handbook for Precision Control*, p.182, Fuji Techno System, Tokyo (1994).
9) H. Horikawa and K. Otsuka: *New Actuator Handbook for Precision Control*, p.454, Fuji Techno System, Tokyo (1994).
10) K. Otsuka and C. M. Wayman: *Shape Memory Materials*, Chap.1, p.1, Cambridge University Press, UK (1998).
11) K.N. Nelton: *Shape Memory Materials*, Chap.10, Cambridge Univ. Press, UK (1998).
12) T. Todoroki, K. Fukuda and T. Hayakumo: Industrial Materials, **32**, No.7, 85 (1984).
13) A. B. Flatau, M. J. Dapino and F. T. Calkins: Magnetostrictive Composites, *Comprehensive Composite Materials*, Chapter 5.26, p.563 (2000).
14) A. E. Clark and H. S. Belson: US Patent 4,378,258 (1983).
15) H. Eda: Giant Magnetostrictive Actuators, *New Actuator Handbook for Precision Control*, p.90, Fuji Techno System, Tokyo (1994).
16) J. L. Butler: Edge Technologies, Ames, IA (1988).
17) K. Uchino: *Ferroelectric Devices*, p.11, Marcel Dekker, NY (2000).
18) K. Yano, T. Hamatsuki, I. Fukui and E. Sato: *Proc. Annual Mtg. EE Japan*, p.1-157 (Spring, 1984).
19) M. Kasuga, T. Satoh, N. Tsukada, T. Yamazaki, F. Ogawa, M. Suzuki, I. Horikoshi and T. Itoh: J. Soc. Precision Eng., **57**, 63 (1991).
20) V. Bharti, H.S. Xu, G. Shanti, Q.M. Zhang and K. Liang: J. Appl. Phys. **87**,452 (2000).
21) S. Bauer: *Proc. Int'l Symp. Smart Actuators*, ICAT/Penn State, PA (April, 1999).
22) K. Uchino: Mat. Res. Innovat., **1**, 163 (1997).
23) M. Tanimura and K. Uchino: Sensors and Mater., **1**, 47 (1988).
24) K. Uchino: J. Rob. Mech., **1**(2), 124 (1989).
25) S. Thakoor, J. M. Morookian, and J. A. Cutts: *Conf. Proc. 10th IEEE Int'l Symp. on Appl. Ferroelectrics*, **1**, 205 (1996).
26) P. Poosanaas, K. Tonooka, and K. Uchino, Mechatronics **10**, 467 (2000).
27) M. R. Jolly and J. D. Carlson: Composites with Field-Responsive Rheology, *Comprehensive Composite Materials*, Chapter 5.27, p.575 (2000).
28) T. Shiga, A. Okada and T. Kurauchi: Macromolecules, **26**, 6958 (1993).
29) V. D. Chase: Appliance Manufacturer, May, p.6 (1996).
30) J. D. Carlson and K. D. Weiss: US Patent 5,382,373 (1995).
31) Y. Yokoya: Electronic Ceramics **22**, No.111, 55 (1991).

The following review papers and books are recommended for further study:

32) K. Uchino:*Piezoelectric/Electrostrictive Actuators*, Morikita Publishing, Tokyo (1986).
33) K. Uchino: Ceramic Actuators: Principles & Applications, MRS Bull. **18**(4), 42 (1993).
34) S. Ueha, Y. Tomikawa, M.Kurosawa and N.Nakamura: *Ultrasonic Motors:Theory and Applications*, Oxford Science Publ., Monographs in EE. Eng. 29 (1993).
35) K. Uchino: *Ferroelectric Devices*, VCH, Materials Sci. and Tech. Vol.11, Chap.12 (1994).
36) K. Uchino: Proc. Electroceramics IV, Vol.1, p.179, RWTH, Aachen (1994).
37) K. Uchino: *Piezoelectric Actuators and Ultrasonic Motors*, Kluwer Academic Publishers, MA (1996).
38) K. Uchino: *Ferroelectric Devices*, Marcel Dekker, NY (2000).

Introduction to Piezoelectric Actuators and Transducers

Kenji Uchino, International Center for Actuators and Transducers, Penn State University
University Park, PA 16802

Abstract

Certain materials produce electric charges on their surfaces as a consequence of applying mechanical stress. The induced charges are proportional to the mechanical stress. This is called the direct piezoelectric effect and was discovered in quartz by Piere and Jacques Curie in 1880. Materials showing this phenomenon also conversely have a geometric strain proportional to an applied electric field. This is the converse piezoelectric effect. The root of the word "piezo" means "pressure"; hence the original meaning of the word piezoelectricity implied "pressure electricity."

Piezoelectricity is extensively utilized in the fabrication of various devices such as transducers, actuators, surface acoustic wave devices, frequency control and so on. In this chapter we describe the piezoelectric materials that are used, and various potential applications of piezoelectric materials.$^{1-4)}$

1. PIEZOELECTRIC MATERIALS AND PROPERTIES

1.1 Piezoelectric Figures of Merit

There are five important figures of merit in piezoelectrics: the piezoelectric strain constant d, the piezoelectric voltage constant g, the electromechanical coupling factor k, the mechanical quality factor Q_M, and the acoustic impedance Z. These figures of merit are considered in this section.

Piezoelectric Strain Constant d

The magnitude of the induced strain x by an external electric field E is represented by this figure of merit (an important figure of merit for actuator applications):

$$x = d\,E\,. \tag{1}$$

Piezoelectric Voltage Constant g

The induced electric field E is related to an external stress X through the piezoelectric voltage constant g (an important figure of merit for sensor applications):

$$E = g\,X. \tag{2}$$

Taking into account the relation, P = d X, we obtain an important relation between g and d:

$$g = d / \varepsilon_0 \varepsilon\,. \qquad (\varepsilon : \text{permittivity}) \tag{3}$$

Electromechanical Coupling Factor k

The terms, electromechanical coupling factor, energy transmission coefficient, and efficiency are sometimes confused.$^{5)}$ All are related to the conversion rate between electrical energy and mechanical energy, but their definitions are different.$^{6)}$

(a) The electromechanical coupling factor k

$$k^2 = (\text{Stored mechanical energy / Input electrical energy}) \tag{4}$$

or

$$k^2 = (\text{Stored electrical energy / Input mechanical energy}) \tag{5}$$

Let us calculate Eq. (4), when an electric field E is applied to a piezoelectric material. Since the input electrical energy is $(1/2)\ \varepsilon_0\varepsilon\ E^2$ per unit volume and the stored mechanical energy per unit volume under zero external stress is given by $(1/2)\ x^2 / s = (1/2)\ (d\ E)^2 / s$, k^2 can be calculated as

$$k^2 = [(1/2)\,(d\,E)^2 / s] / [(1/2)\,\varepsilon_0\varepsilon\,E^2]$$
$$= d^2 / \varepsilon_0\varepsilon\cdot s. \tag{6}$$

(b) The energy transmission coefficient λ_{max}

Not all the stored energy can be actually used, and the actual work done depends on the mechanical load. With zero mechanical load or a complete clamp (no strain) zero output work is done.

$$\lambda_{max} = (\text{Output mechanical energy / Input electrical energy})_{max} \tag{7}$$

or

$$\lambda_{max} = (\text{Output electrical energy / Input mechanical energy})_{max} \tag{8}$$

Let us consider the case where an electric field E is applied to a piezoelectric under constant external stress X (< 0, because a compressive stress is necessary to work to the outside). As shown in Fig. 1, the output work can be calculated as

$$\int (-X)\,dx = -(d\,E + s\,X)\,X, \tag{9}$$

while the input electrical energy is given by

$$\int E\,dP = (\varepsilon_0\varepsilon\,E + d\,X)\,E. \tag{10}$$

We need to choose a proper load to maximize the energy transmission coefficient. From the maximum condition of

$$\lambda = -(d\,E + s\,X)\,X / (\varepsilon_0\varepsilon\,E + d\,X)\,E, \tag{11}$$

we can obtain

$$\lambda_{max} = [(1/k) - \sqrt{(1/k^2) - 1}\,]^2$$
$$= [(1/k) + \sqrt{(1/k^2) - 1}\,]^{-2}. \tag{12}$$

Notice that

$$k^2/4 < \lambda_{max} < k^2/2 \tag{13}$$

depending on the k value. For a small k, $\lambda_{max} = k^2/4$, and for a large k, $\lambda_{max} = k^2/2$.

It is also worth noting that the maximum condition stated above does not agree with the condition which provides the maximum output mechanical energy. The maximum output energy can be obtained when the load is half of the maximum generative stress: $-(d\,E - s\,(d\,E / 2s))\,(-d\,E / 2s) = (d\,E)^2/ 4s$. In this case, since the input electrical energy is given by $(\varepsilon_0\varepsilon\,E + d\,(-d\,E / 2s))\,E$,

$$\lambda = 1 / 2[(2/k^2) - 1], \tag{14}$$

which is close to the value λ_{max}, but has a different value that is predicted theoretically.

(c) The efficiency η

$$\eta = (\text{Output mechanical energy}) / (\text{Consumed electrical energy}) \tag{15}$$

or

$$\eta = (\text{Output electrical energy}) / (\text{Consumed mechanical energy}). \tag{16}$$

In a work cycle (e.g., an electric field cycle), the input electrical energy is transformed partially into mechanical energy and the remaining is stored as electrical energy (electrostatic energy like a capacitor) in an actuator. In this way, the ineffective energy can be returned to the power source, leading to near 100% efficiency, if the loss is small. Typical values of dielectric loss in PZT are about 1 - 3%.

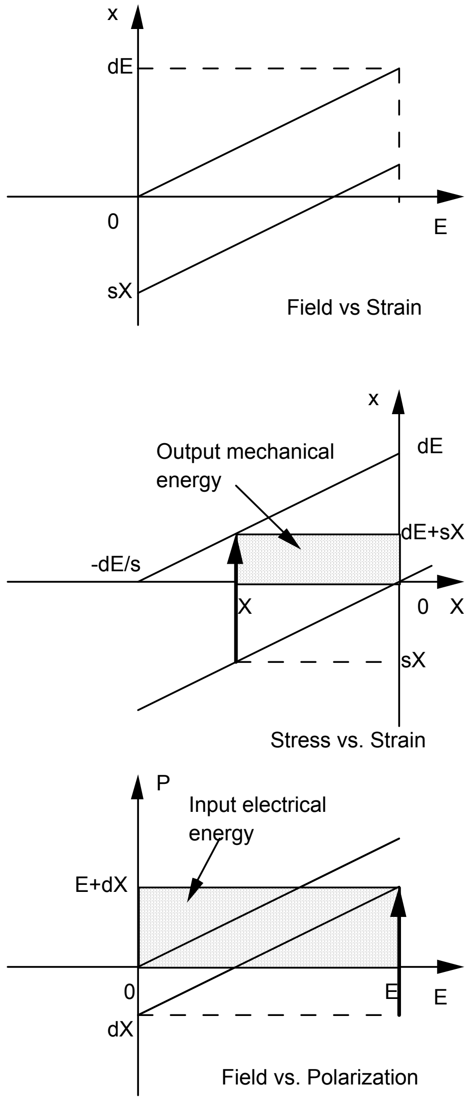

Fig. 1 Calculation of the input electrical and output mechanical energy.

Mechanical Quality Factor Q_M

The mechanical quality factor, Q_M, is a parameter that characterizes the sharpness of the electromechanical resonance spectrum. When the motional admittance Y_m is plotted around the resonance frequency ω_0, the mechanical quality factor Q_M is defined with respect to the full width at $Y_m/\sqrt{2}$ $[2\Delta\omega]$ as :

$$Q_M = \omega_0 / 2\Delta\omega. \tag{17}$$

Also note that Q_M^{-1} is equal to the mechanical loss ($\tan \delta_m$). The Q_M value is very important in evaluating the magnitude of the resonant strain. The vibration amplitude at an off-resonance frequency (d E L, L: length of the sample) is amplified by a factor proportional to Q_M at the resonance frequency. For a longitudinally vibration rectangular plate through d_{31}, the maximum displacement is given by $(8/\pi^2)\, Q_M\, d_{31}\, E\, L$.

Acoustic Impedance Z

The acoustic impedance Z is a parameter used for evaluating the acoustic energy transfer between two materials. It is defined, in general, by

$$Z^2 = \text{(pressure/volume velocity)}. \tag{18}$$

In a solid material,

$$Z = \sqrt{\rho c}\ , \tag{19}$$

where ρ is the density and c is the elastic stiffness of the material.

In more advanced discussions, there are three kinds of impedances; specific acoustic impedance (pressure/particle speed), acoustic impedance (pressure/volume speed) and radiation impedance (force/speed). See Ref. 6) for the details.

Table 1 Piezoelectric properties of representative piezoelectric materials. 7,8)

Parameter	Quartz	$BaTiO_3$	PZT 4	PST5H	$(Pb,Sm)TiO_3$	PVDF-TrFE
d_{33} (pC/N)	2.3	190	289	593	65	33
g_{33} (10^{-3}Vm/N)	57.8	12.6	26.1	19.7	42	380
k_t	0.09	0.38	0.51	0.50	0.50	0.30
k_p		0.33	0.58	0.65	0.03	
$\varepsilon_3{}^T/\varepsilon_0$	5	1700	1300	3400	175	6
Q_m	$> 10^5$		500	65	900	3 - 10
T_C (°C)		120	328	193	355	

1.2 Piezoelectric Materials7)

This section summarizes the current status of piezoelectric materials: single-crystal materials, piezoceramics, piezopolymers, piezocomposites and piezofilms. Table 1 shows the material parameters of some of the piezoelectric materials.8)

Single Crystals

Although piezoelectric ceramics are widely used for a large number of applications, single crystal materials retain their utility, being essential for applications such as frequency stabilized oscillators and surface acoustic devices. The most popular single-crystal piezoelectric materials are quartz, lithium niobate ($LiNbO_3$), and lithium tantalate ($LiTaO_3$). The single crystals are anisotropic, exhibiting different material properties depending on the cut of the materials and the direction of bulk or surface wave propagation.

Quartz is a well-known piezoelectric material. α-quartz belongs to the triclinic crystal system with point group 32 and has a phase transition at 537°C to its β-form which is not piezoelectric. Quartz has a cut with a zero temperature coefficient. For instance, quartz oscillators, operated in the thickness shear mode of the AT-cut, are used extensively for clock sources in computers, frequency stabilized ones in TVs and VCRs. On the other hand, an ST-cut quartz substrate with X-propagation has a zero temperature coefficient for surface acoustic wave and so is used for SAW devices with high-stabilized frequencies. The another distinguished characteristic of quartz is an extremely high mechanical quality factor $Q_m > 10^5$.

Lithium niobate and lithium tantalate belong to an isomorphous crystal system and are composed of oxygen octahedron. The Curie temperatures of $LiNbO_3$ and $LiTaO_3$ are 1210 and 660°C, respectively. The crystal symmetry of the ferroelectric phase of these single crystals is 3m and the polarization direction is along c-axis. These materials have high electromechanical coupling coefficients for surface acoustic wave. In addition, large single crystals can easily be obtained from their melt using the conventional Czochralski technique. Thus both materials occupy very important positions in the SAW device application field.

Polycrystalline Materials

Barium titanate $BaTiO_3$ is one of the most thoroughly studied and most widely used piezoelectric materials. Just below the Curie temperature (120°C), the vector of the spontaneous polarization points in the [001] direction (tetragonal phase), below 5 °C it reorients in the [011] (orthrhombic phase) and below - 90 °C in the [111] direction (rhombohedral phase). The dielectric and piezoelectric properties of ferroelectric ceramic $BaTiO_3$ can be affected by its own stoichiometry, microstructure, and by dopants entering onto the A or B site in solid solution. Modified ceramic $BaTiO_3$ with dopants such as Pb or Ca ions have been developed to stabilize the tetragonal phase over a wider temperature range and are used as commercial piezoelectric materials. The initial application was for Langevin-type piezoelectric vibrators.

Piezoelectric $Pb(Ti,Zr)O_3$ solid solutions [PZT] ceramics have been widely used because of their superior piezoelectric properties. The phase diagram for the PZT system ($PbZr_xTi_{1-x}O_3$) is shown in Fig. 2. The crystalline symmetry of this solid-solution system is determined by the Zr content. Lead titanate also has a tetragonal ferroelectric phase of perovskite structure. With increasing Zr content, x, the tetragonal distortion decreases and at $x > 0.52$ the structure changes from the tetragonal 4mm phase to another ferroelectric phase of rhombohedral 3m symmetry. The line dividing these two phases is called the *morphotropic phase boundary*. The boundary composition is considered to have both tetragonal and rhombohedral phases coexisting together. Figure 3 shows the dependence of several piezoelectric d constants on composition near the morphotropic phase boundary. The d constants have their highest values near the morphotropic phase boundary. This enhancement in piezoelectric effect is attributed to the increased ease of reorientation of the polarization under an applied electric field.

Doping the PZT material with donor or acceptor ions changes its properties dramatically. Donor doping with ions such as Nb^{5+} or Ta^{5+} provides soft PZTs, like PZT-5, because of the facility of domain motion due to the resulting Pb-vacancies. On the other hand, acceptor doping with Fe^{3+} or Sc^{3+} leads to hard PZTs, such as PZT-8, because the oxygen vacancies will pin domain wall motion.

Subsequently, PZT in ternary solid solution with another perovskite phase has been investigated intensively. Examples of these ternary compositions are: PZTs in solid solution with $Pb(Mg_{1/3}Nb_{2/3})O_3$, $Pb(Mn_{1/3}Sb_{2/3})O_3$, $Pb(Co_{1/3}Nb_{2/3})O_3$, $Pb(Mn_{1/3}Nb_{2/3})O_3$, $Pb(Ni_{1/3}Nb_{2/3})O_3$, $Pb(Sb_{1/2}Sn_{1/2})O_3$, $Pb(Co_{1/2}W_{1/2})O_3$, $Pb(Mg_{1/2}W_{1/2})O_3$, all of which are patented by different companies.

The end member of PZT, lead titanate has a large crystal distortion. $PbTiO_3$ has a tetragonal structure at room temperature with its tetragonality c/a = 1.063. The Curie temperature is 490 °C. Densely sintered $PbTiO_3$ ceramics cannot be obtained easily, because they break up into a powder when cooled through the Curie temperature due to the large spontaneous strain. Lead titanate ceramics modified by adding a small amount of additives exhibit a high piezoelectric anisotropy. Either $(Pb, Sm)TiO_3$9) or $(Pb, Ca)TiO_3$10) exhibits an extremely low planar coupling, that is, a large k_t / k_p ratio. Here, k_t and k_p are thickness-extensional and planar electromechanical coupling factors, respectively. Since these transducers can generate purely longitudinal waves through k_t associated with no transverse waves through k_{31}, clear ultrasonic imaging is expected without “ghost” caused by the transverse wave. $(Pb,Nd)(Ti,Mn,In)O_3$ ceramics with a zero temperature coefficient of surface acoustic wave delay have been developed as superior substrate materials for SAW device applications.11)

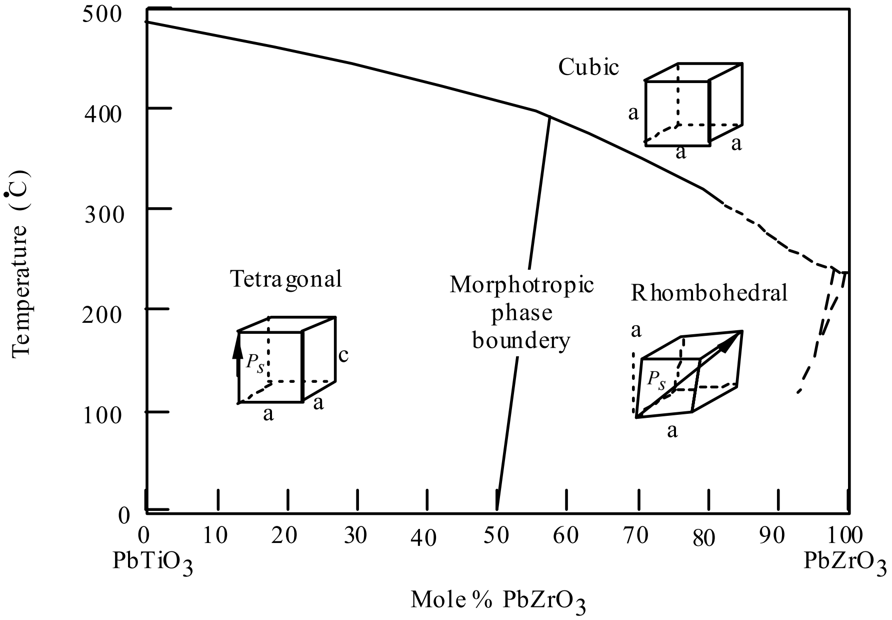

Fig. 2 Phase diagram of lead zirconate titanate (PZT).

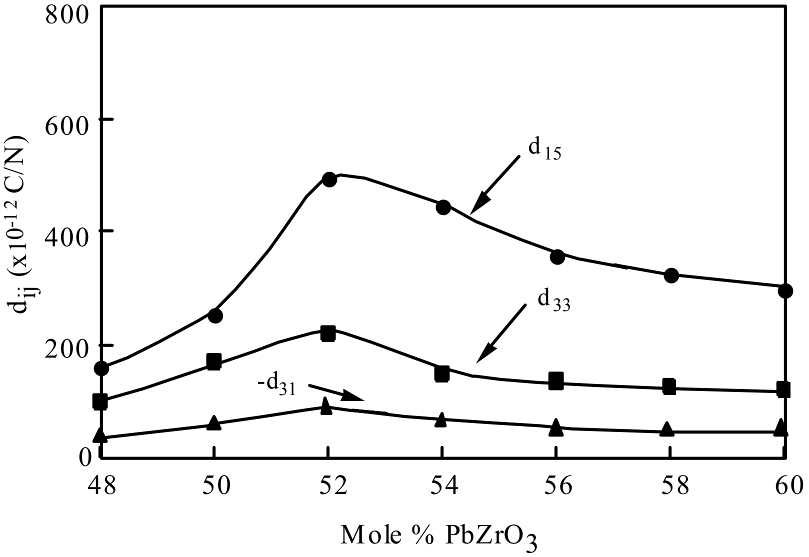

Fig. 3 Dependence of several d constants on composition near the morphotropic phase boundary in the PZT system.

Relaxor Ferroelectrics

Relaxor ferroelectrics can be prepared either in polycrystalline form or as single crystals. They differ from the previously mentioned normal ferroelectrics in that they exhibit a broad phase transition from the paraelectric to ferroelectric state, a strong frequency dependence of the dielectric constant (i.e., dielectric relaxation) and a weak remanent polarization. Lead-based relaxor materials have complex disordered perovskite structures.

Relaxor-type electrostrictive materials, such as those from the lead magnesium niobate - lead titanate, $Pb(Mg_{1/3}Nb_{2/3})O_3$ - $PbTiO_3$ (or PMN-PT), solid solution are highly suitable for actuator applications. This relaxor ferroelectric also exhibits an induced piezoelectric effect. That is, the electromechanical coupling factor k_t

varies with the applied DC bias field. As the DC bias field increases, the coupling increases and saturates. Since this behavior is reproducible, these materials can be applied as ultrasonic transducers which are tunable by the bias field.12)

Recently, single-crystal relaxor ferroelectrics with the morphotropic phase boundary (MPB) composition have been developed which show tremendous promise as ultrasonic transducers and electro-mechanical actuators. Single crystals of $Pb(Mg_{1/3}Nb_{2/3})O_3$ (PMN), $Pb(Zn_{1/3}Nb_{2/3})O_3$ (PZN) and binary systems of these materials combined with $PbTiO_3$ (PMN-PT and PZN-PT) exhibit extremely large electromechanical coupling factors.13,14) Large coupling coefficients and large piezoelectric constants have been found for crystals from the morphotropic phase boundaries of these solid solutions. PZN-8%PT single crystals were found to possess a high k_{33} value of 0.94 for the (001) crystal cuts; this is very high compared to the k_{33} of conventional PZT ceramics of around 0.70-0.80.

Polymers

Polyvinylidene difluoride, PVDF or PVF2, is piezoelectric when stretched during fabrication. Thin sheets of the cast polymer are then drawn and stretched in the plane of the sheet, in at least one direction, and frequently also in the perpendicular direction, to transform the material to its microscopically polar phase. Crystallization from the melt forms the non-polar α-phase, which can be converted into the polar β-phase by a uniaxial or biaxial drawing operation; the resulting dipoles are then reoriented through electric poling (see Fig. 4).

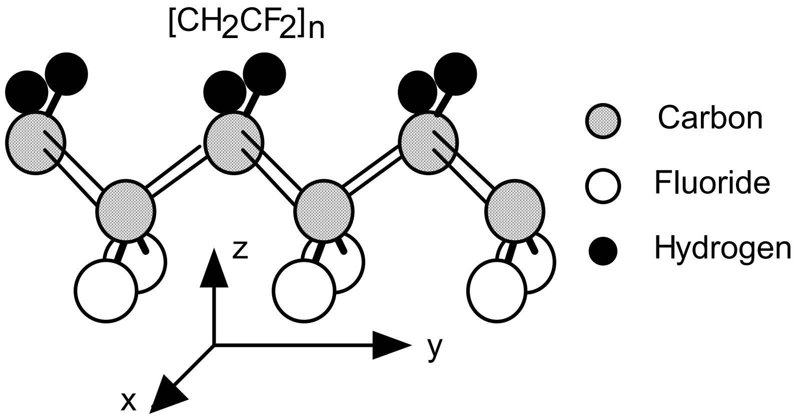

Fig. 4 Structure of polyvinylidene diflouride (PVDF).

Large sheets can be manufactured and thermally formed into complex shapes. The copolymerization of vinilydene difluoride with trifluoroethylene (TrFE) results in a random copolymer (PVDF-TrFE) with a stable, polar β-phase. This polymer need not be stretched; it can be poled directly as formed. A thickness-mode coupling coefficient of 0.30 has been reported. Piezoelectric polymers have the following characteristics : (a) small piezoelectric d constants (for actuators) and large g constants (for sensors), (b) light weight and soft elasticity, leading to good acoustic impedance matching with water or the human body, (c) a low mechanical quality factor Q_M, allowing for a broad resonance band width. Such piezoelectric polymers are used for directional microphones and ultrasonic hydrophones.

Composites

Piezocomposites comprised of a piezoelectric ceramic and a polymer phase are promising materials because of their excellent and readily tailored properties. The geometry for two-phase composites can be classified according to the dimensional connectivity of each phase into 10 structures; 0-0, 0-1, 0-2, 0-3, 1-1, 1-2, 1-3, 2-2, 2-3 and 3-3.15) A 1-3 piezo-composite, such as the PZT-rod / polymer composite is a most promising candidate. The advantages of this composite are high coupling factors, low acoustic impedance, good matching to water or human tissue, mechanical flexibility, broad bandwidth in combination with a low mechanical quality factor and the possibility of making undiced arrays by structuring the electrodes. The thickness-mode electromechanical coupling of the composite can exceed the k_t (0.40-0.50) of the constituent ceramic, approaching almost the value of the rod-mode electromechanical coupling, k_{33} (0.70-0.80) of that ceramic.[16] Acoustic impedance is the square root of the product of its density and elastic stiffness. The acoustic match to tissue or water (1.5 Mrayls) of the typical piezoceramics (20-30 Mrayls) is significantly improved by forming a composite structure, that is, by replacing some of the heavy, stiff ceramic with a light, soft polymer. Piezoelectric composite materials are especially useful for underwater sonar and medical diagnostic ultrasonic transducer applications.

Thin-Films

Both zinc oxide (ZnO) and aluminum nitride (AlN) are simple binary compounds with a Wurtzite-type structure, which can be sputter-deposited as a c-axis oriented thin film on a variety of substrates. ZnO has large piezoelectric coupling and thin films of this material are widely used in bulk acoustic and surface acoustic wave devices. The fabrication of highly oriented (along c) ZnO films have been studied and developed extensively. The performance of ZnO devices is limited, however, due to their low piezoelectric coupling (20 - 30%). PZT thin films are expected to exhibit higher piezoelectric properties. At present the growth of PZT thin films is being carried out for use in micro-transducers and micro-actuators.

2. PRESSURE SENSORS/ACCELEROMETERS/GYROSCOPES

One of the very basic applications of piezoelectric ceramics is a gas igniter. The very high voltage generated in a piezoelectric ceramic under applied mechanical stress can cause sparking and ignite the gas (Fig. 5). There are two means to apply the mechanical force, either by a rapid, pulsed application or by a more gradual, continuous increase.

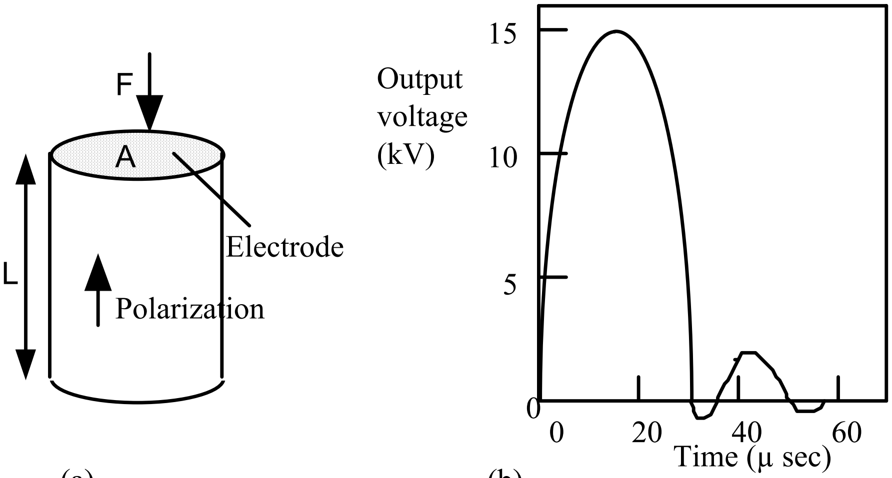

(a) (b)

Fig. 5 (a) Gas igniter and (b) output voltage.

Piezoelectric ceramics can be employed as stress sensors and acceleration sensors, because of the *direct piezoelectric effect*. Figure 6 shows a 3-D stress sensor designed by Kistler. By combining an appropriate number of quartz crystal plates (extensional and shear types), the multilayer device can detect three-dimensional stresses.[17]

Figure 7 shows a cylindrical gyroscope commercialized by Tokin (Japan).[18] The cylinder has six divided electrodes, one pair of which are used to excite the fundamental bending vibration mode, while the other two pairs are used to detect the acceleration. When the rotational acceleration is applied about the axis of this gyro, the voltage generated on the electrodes is modulated by the *Coriolis force*. By subtracting the signals between the two sensor electrode pairs, a voltage directly proportional to the acceleration can be obtained.

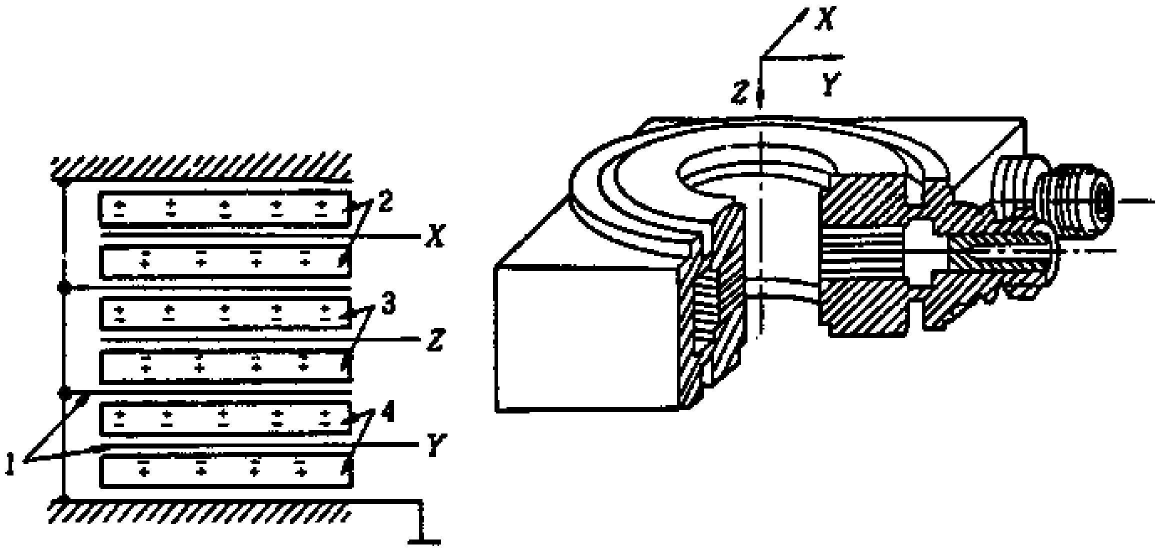

Fig. 6 3-D stress sensor (by Kistler).

The *converse electrostrictive effect* - the stress dependence of the permittivity - is also used in stress sensors.[19] A bimorph structure provides superior stress sensitivity and temperature stability. A measuring system with a bimorph structure, which subtracts the static capacitances of two dielectric ceramic plates, has been proposed.[19] The capacitance changes of the top and bottom plates have opposite signs for uniaxial stress and the same sign for temperature deviation. The response speed is limited by the capacitance measuring frequency to about 1 kHz. Unlike piezoelectric sensors, electrostrictive sensors are effective in the low frequency range, especially DC.

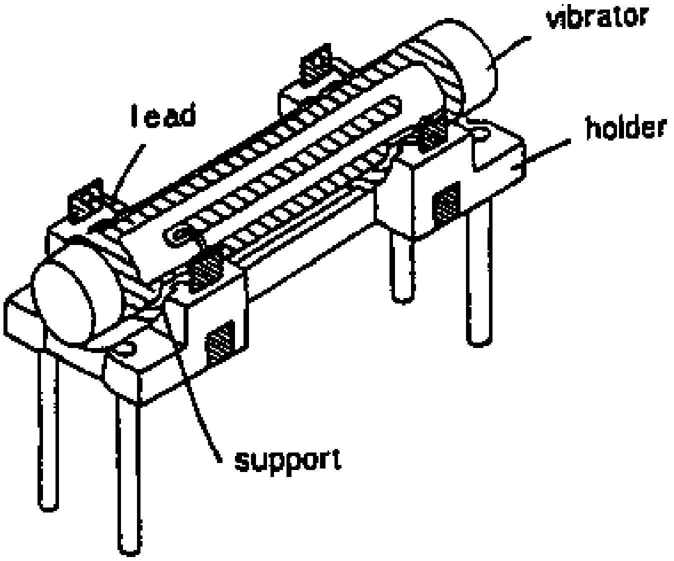

Fig. 7 Cylindrical gyroscope (by Tokin).

3. PIEZOELECTRIC VIBRATORS/ULTRASONIC TRANSDUCERS

3.1 Piezoelectric Resonance

The Piezoelectric Equations

When an electric field is applied to a piezoelectric material, deformation (ΔL) or strain ($\Delta L/L$) arises. When the field is alternating, mechanical vibration is caused, and if the drive frequency is adjusted to a mechanical resonance frequency of the device, large resonating strain is generated. This phenomenon can be understood as a strain magnification due to accumulating input energy, and is called *piezoelectric resonance*. Piezoelectric resonance is very useful for realizing energy trap devices, actuators etc. The theoretical treatment is as follows.

If the applied electric field and the generated stress are not large, the stress X and the dielectric displacement D can be represented by the following equations:

$$x_i = s_{ij}^E X_j + d_{mi} E_m, \qquad (20)$$

$$(i,j = 1,2,...,6 \; ; \; m,k = 1,2,3)$$

$$D_m = d_{mi} X_i + \varepsilon_{mk}^X E_k. \qquad (21)$$

These are called the *piezoelectric equations*. The number of independent parameters for the lowest symmetry trigonal crystal are 21 for s_{ij}^E, 18 for d_{mi} and 6 for ε_{mk}^X. The number of independent parameters decreases with increasing crystallographic symmetry. Concerning the polycrystalline ceramics, the poled axis is usually denoted as the z-axis and the ceramic is isotropic with respect to this z-axis (Curie group $C_{\infty V}$ (∞m)). The number of non-zero matrix elements in this case is 10 (s_{11}^E, s_{12}^E, s_{13}^E, s_{33}^E, s_{44}^E, d_{31}, d_{33}, d_{15}, ε_{11}^X, and ε_{33}^X).

Electromechanical Coupling Factor

Next let us introduce the *electromechanical coupling factor* k, which corresponds to the rate of electro-mechanical transduction. The internal energy U of a piezoelectric vibrator is given by summation of the mechanical energy U_M ($= \int x\, dX$) and the electrical energy U_E ($= \int D\, dE$). U is calculated as follows, when linear relations Eqs. (20) and (21) are applicable :

$$\begin{aligned} U &= U_M + U_E \\ &= \Big[(1/2) \sum_{i,j} s_{ij}^E X_j X_i + (1/2) \sum_{m,i} d_{mi} E_m X_i\Big] \\ &\quad + \Big[(1/2) \sum_{i,j} d_{mi} X_i E_m + (1/2) \sum_{k,m} \varepsilon_{mk}^X E_k E_m\Big] . \end{aligned} \qquad (22)$$

The s and E terms represent purely mechanical and electrical energies (U_{MM} and U_{EE}), respectively, and the d term denotes the energy transduced from electrical to mechanical energy or vice versa through the piezoelectric effect. The coupling factor k is defined by :

$$k = U_{ME} / \sqrt{U_{MM} \cdot U_{EE}}. \qquad (23)$$

The k value varies with the vibrational mode (even in the same ceramic sample), and can have a positive or negative value. Note that this definition is equivalent to the definition provided in Section 1.1:

k^2 = (Stored mechanical energy / Input electrical energy)

or

k^2 = (Stored electrical energy / Input mechanical energy).

Longitudinal Vibration Mode

Let us consider the longitudinal mechanical vibration of a piezoceramic plate through the transverse piezoelectric effect (d_{31}) as shown in Fig. 8. If the polarization is in the z-direction and x-y planes are the planes of the electrodes, the extentional vibration in the x direction is represented by the following dynamic equation :

$$\rho(\partial^2 u/\partial t^2) = F = (\partial X_{11}/\partial x) + (\partial X_{12}/\partial y) + (\partial X_{13}/\partial z), \qquad (24)$$

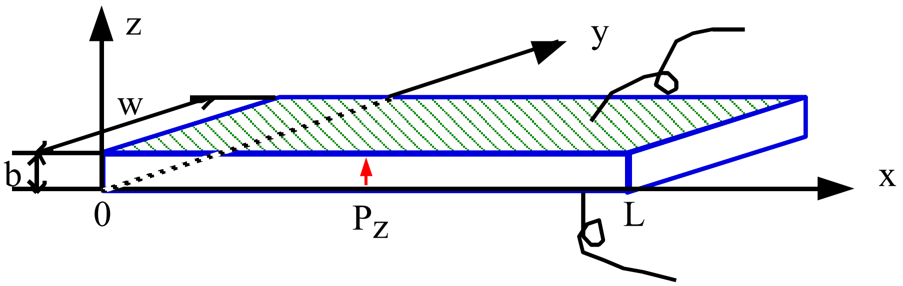

Fig. 8 Longitudinal vibration through the transverse piezoelectric effect (d_{31}) in a rectangular plate.

where u is the displacement of the small volume element in the ceramic plate in the x-direction. The relations between stress, electric field (only E_z exists) and the induced strain are given by :

$$
\begin{aligned}
x_1 &= s_{11}^E X_1 + s_{12}^E X_2 + s_{13}^E X_3 + d_{31} E_z , \\
x_2 &= s_{12}^E X_1 + s_{11}^E X_2 + s_{13}^E X_3 + d_{31} E_z , \\
x_3 &= s_{13}^E X_1 + s_{13}^E X_2 + s_{33}^E X_3 + d_{33} E_z , \\
x_4 &= s_{44}^E X_4 , \\
x_5 &= s_{44}^E X_5 , \\
x_6 &= 2(s_{11}^E - s_{12}^E) X_6 . \qquad (25)
\end{aligned}
$$

When the plate is very long and thin, X_2 and X_3 may be set equal to zero through the plate. Since shear stress will not be generated by the electric field E_z, Eq. (25) is reduced to :

$$X_1 = x_1/s_{11}^E - (d_{31}/s_{11}^E)E_z. \qquad (26)$$

Introducing Eq. (26) into Eq. (24), and allowing for $x_1=\partial u/\partial x$ and $\partial E_z/\partial x=0$ (due to the equal potential on each electrode), leads to a harmonic vibration equation:

$$- \omega^2 \rho\, s_{11}^E\, u = \partial^2 u/\partial x^2 . \qquad (27)$$

Here, ω is the angular frequency of the drive field, and ρ is the density. Substituting a general solution $u=u_1(x)e^{j\omega t}+u_2(x)e^{-j\omega t}$ into Eq. (26), and with the boundary condition $X_1 = 0$ at x = 0 and L (sample length), the following solution can be obtained:

$$\partial u/\partial x = x_1 = d_{31}E_z\, [\sin\omega(L-x)/v + \sin(\omega x/v) /\sin(\omega L/v) . \qquad (28)$$

Here, v is the *sound velocity* in the piezoceramic which is given by

$$v = 1 / \sqrt{\rho\, s_{11}^E} . \qquad (29)$$

When the specimen is utilized as an electrical component such as a filter or a vibrator, the electrical impedance [(applied voltage/induced current) ratio] plays an important role. The current flow into the specimen is described by the surface charge increment, $\partial D_3/\partial t$, and the total current is given by :

$$i = j\omega w \int_0^L D_3\, dx = j\omega w \int_0^L [(\varepsilon_{33}^X - d_{31}^2/s_{11}^E)E_z + (d_{31}/s_{11}^E)x_1]\, dx . \qquad (30)$$

Using Eq. (28), the admittance for the mechanically free sample is calculated to be:

$$
\begin{aligned}
&(1/Z) = (i/V) = (i/E_z t) \\
&\quad = (j\omega wL/t)\, \varepsilon_{33}^{LC}[1 + (d_{31}^2/ \varepsilon_{33}^{LC} s_{11}^E)(\tan(\omega L/2v) / (\omega L/2v)] , \qquad (31)
\end{aligned}
$$

where w is the width, L the length, t the thickness of the sample, and V the applied voltage. ε_{33}^{LC} is the permittivity in a longitudinally clamped sample, which is given by

$$\varepsilon_{33}^{LC} = \varepsilon_{33}^{X} - (d_{31}^{2}/s_{11}^{E}) . \qquad (32)$$

The piezoelectric resonance is achieved where the admittance becomes infinite or the impedance is zero. The resonance frequency f_R is calculated from Eq. (31), and the fundamental frequency is given by

$$f_R = v/2L = 1/(2L\sqrt{\rho\, s_{11}^{E}}). \qquad (33)$$

On the other hand, the antiresonance state is generated for zero admittance or infinite impedance:

$$(\omega_A L/2v) \cot (\omega_A L/2v) = - d_{31}^{2}/ \varepsilon_{33}^{LC} s_{11}^{E} = - k_{31}^{2}/ (1 - k_{31}^{2}). \qquad (34)$$

The final transformation is provided by the definition,

$$k_{31} = d_{31}/ \sqrt{s_{11}^{E}\, \varepsilon_{33}^{X}}. \qquad (35)$$

The resonance and antiresonance states are described by the following intuitive model. In a high electromechanical coupling material with k almost equal to 1, the resonance or antiresonance states appear for $\tan(\omega L/2v) = \infty$ or 0 [i. e., $\omega L/2v = (m-1/2)\pi$ or $m\pi$ (m: integer)], respectively. The strain amplitude x_1 distribution for each state [calculated using Eq. (28)] is illustrated in Fig. 9. In the resonance state, large strain amplitudes and large capacitance changes (called *motional capacitance*) are induced, and the current can easily flow into the device. On the other hand, at antiresonance, the strain induced in the device compensates completely, resulting in no capacitance change, and the current cannot flow easily into the sample. Thus, for a high k material the first antiresonance frequency f_A should be twice as large as the first resonance frequency f_R.

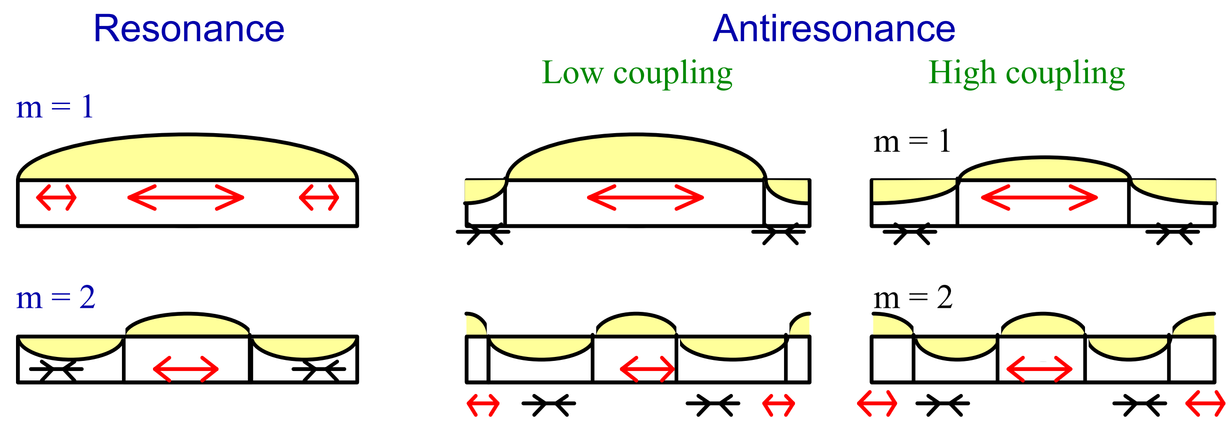

Fig. 9 Strain generation in the resonant or antiresonant state.

In a typical case, where $k_{31} = 0.3$, the antiresonance state varies from the previously-mentioned mode and becomes closer to the resonance mode. The low-coupling material exhibits an antiresonance mode where capacitance change due to the size change is compensated completely by the current required to charge up the static capacitance (called *damped capacitance*). Thus, the antiresonance frequency f_A will approach the resonance frequency f_R.

The general processes for calculating the electromechanical parameters (k_{31}, d_{31}, s_{11}^{E}, and ε_{33}^{X}) are described below:

(1) The sound velocity v in the specimen is obtained from the resonance frequency f_R (refer to Fig. 10), using Eq. (33).

(2) Knowing the density ρ, the elastic compliance s_{11}^E can be calculated.

(3) The electromechanical coupling factor k_{31} is calculated from the v value and the antiresonance frequency f_A through Eq. (34). Especially in low-coupling piezoelectric materials, the following approximate equation is available:

$$k_{31}^2 / (1 - k_{31}^2) = (\pi^2/4)(\Delta f / f_R). \quad (\Delta f = f_A - f_R) \tag{36}$$

(4) Knowing the permittivity ε_{33}^X, the d_{31} is calculated through Eq. (35).

Figure 10 shows observed impedance curves for a typical k material (PZT 5H, $k_{33} = 0.70$) and a high k material (PZN-PT single crystal, $k_{33} = 0.90$). Note a large separation between the resonance and antiresonance peaks in the high k material, leading to the condition $f_A = 2 f_R$.

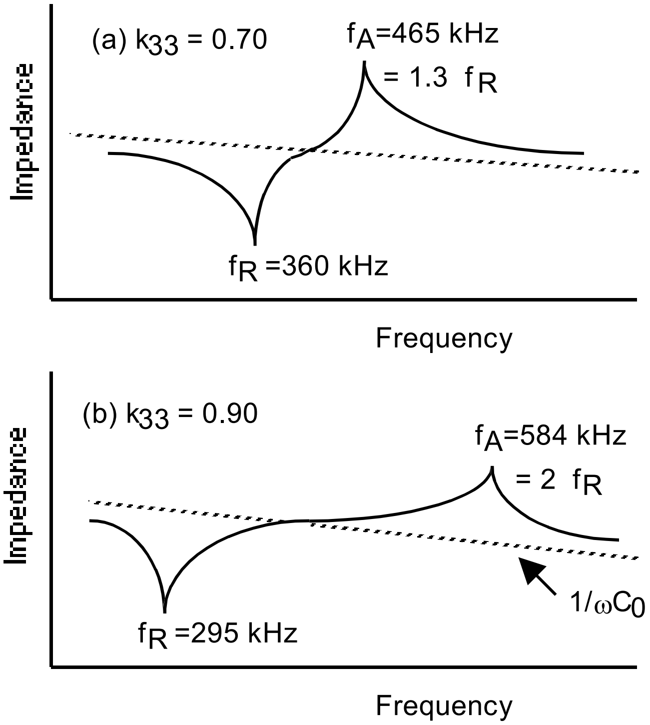

Fig. 10 (a) Impedance curves for a reasonable k material (PZT 5H, $k_{33} = 0.70$), and (b) a high k material (PZN-PT single crystal, $k_{33} = 0.90$).

3.2 Equivalent Circuits of Piezoelectric Vibrators

The *equivalent circuit* for the piezoelectric acuator is represented by a combination of L, C and R. Figure 11(a) shows an equivalent circuit for the resonance state, which has a very low impedance. C_d corresponds to the electrostatic capacitance, and the components L_A and C_A in a series resonance circuit are related to the piezoelectric motion. For example, in the case of the longitudinal vibration of the above rectangular plate through d_{31}, these components are represented by

$$L_A = (\rho / 8)(Lb / w)(s_{11}^{E2} / d_{31}^2), \tag{37}$$

$$C_A = (8 / \pi^2)(Lw / b)(d_{31}^2 / s_{11}^E). \tag{38}$$

The component R_A corresponds to the mechanical loss.

In contrast, the equivalent circuit for the antiresonance state of the same actuator is shown in Fig. 11(b), which has high impedance.

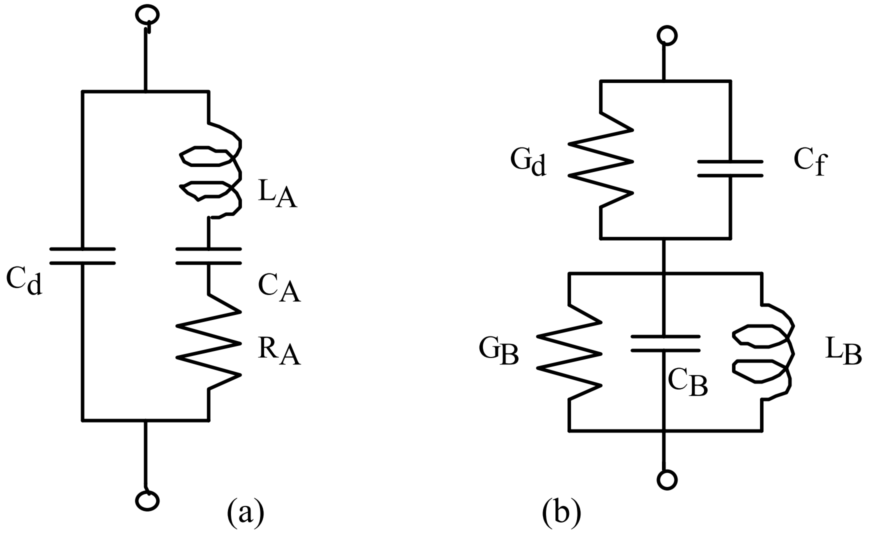

Fig. 11 Equivalent circuit of a piezoelectric device for (a) the resonance and (b) the antiresonance states.

3.3 Piezoelectric Vibrators

In the use of mechanical vibration devices such as filters or oscillators, the size and shape of a device are very important, and both the vibrational mode and the ceramic material must be considered. The resonance frequency of the bending mode in a centimeter-size sample ranges from 100 to 1000 Hz, which is much lower than that of the thickness mode (100 kHz). For these vibrator applications the piezoceramic should have a high mechanical quality factor (Q_M) rather than a large piezoelectric coefficient d; that is, hard piezoelectric ceramics are preferable.

For speakers or buzzers, audible by humans, devices with a rather low resonance frequency are used (kHz range). Examples are a bimorph consisting of two piezo-ceramic plates bonded together, and a piezoelectric fork consisting of a piezo-device and a metal fork. A piezoelectric buzzer is shown in Fig. 12, which has merits such as high electric power efficiency, compact size and long life.

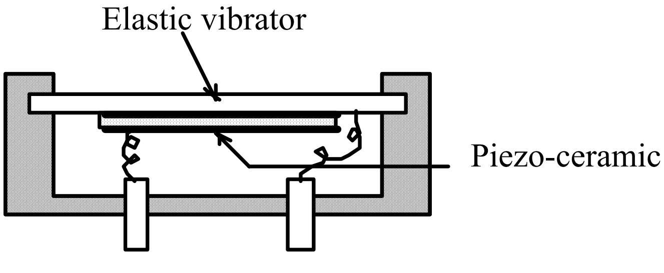

Fig. 12 Piezoelectric buzzer.

3.4 Ultrasonic Transducers

Ultrasonic waves are now used in various fields. The sound source is made from piezoelectric ceramics as well as magnetostrictive materials. Piezoceramics are generally superior in efficiency and in size to magnetostrictive materials. In particular, hard piezoelectric materials with a high Q_M are preferable. A liquid medium is usually used for sound energy transfer. Ultrasonic washers, ultrasonic microphones for short-distance remote control and underwater detection, such as sonar and fish finding, and nondestructive testing are typical applications. Ultrasonic scanning detectors are useful in medical electronics for clinical applications ranging from diagnosis to therapy and surgery.

One of the most important applications is based on ultrasonic echo field.[20,21) Ultrasonic transducers convert electrical energy into mechanical form when generating an acoustic pulse and convert mechanical energy into an electrical signal when detecting its echo. The transmitted waves propagate into a body and echoes are generated which travel back to be received by the same transducer. These echoes vary in intensity according to the type of tissue or body structure, thereby creating images. An ultrasonic image represents the mechanical properties of the tissue, such as density and elasticity. We can recognize anatomical structures in an ultrasonic image since the organ boundaries and fluid-to-tissue interfaces are easily discerned. The ultrasonic imaging process can also be done in real time. This means we can follow rapidly moving structures such as the heart without motion distortion. In addition, ultrasound is one of the safest diagnostic imaging techniques. It does not use ionizing radiation like x-rays and thus is routinely used for fetal and obstetrical imaging. Useful areas for ultrasonic imaging include cardiac structures, the vascular systems, the fetus and abdominal organs such as liver and kidney. In brief, it is possible to see inside the human body without breaking the skin by using a beam of ultrasound.

Figure 13 shows the basic ultrasonic transducer geometry. The transducer is mainly composed of matching, piezoelectric material and backing layers.22) One or more matching layers are used to increase sound transmissions into tissues. The backing is added to the rear of the transducer in order to damp the acoustic backwave and to reduce the pulse duration. Piezoelectric materials are used to generate and detect ultrasound. In general, broadband transducers should be used for medical ultrasonic imaging. The broad bandwidth response corresponds to a short pulse length, resulting in better axial resolution. Three factors are important in designing broad bandwidth transducers; acoustic impedance matching, a high electromechanical coupling coefficient of the transducer, and electrical impedance matching. These pulse echo transducers operate based on thickness mode resonance of the piezoelectric thin plate. Further, a low planar mode coupling coefficient, k_p, is beneficial for limiting energies being expended in nonproductive lateral mode. A large dielectric constant is necessary to enable a good electrical impedance match to the system, especially with tiny piezoelectric sizes.

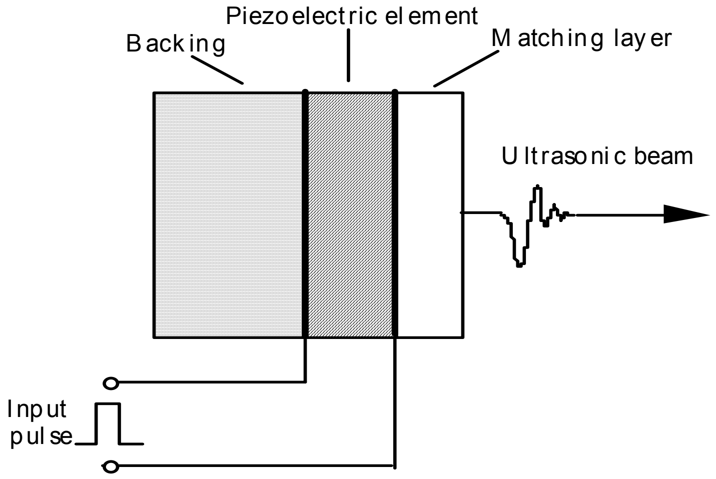

Fig. 13 Basic transducer geometry for acoustic imaging applications.

There are various types of transducers used in ultrasonic imaging. Mechanical sector transducers consist of single, relatively large resonators and can provide images by mechanical scanning such as wobbling. Multiple element array transducers permit discrete elements to be individually accessed by the imaging system and enable electronic focusing in the scanning plane to various adjustable penetration depths through the use of phase delays. Two basic types of array transducers are linear and phased (or sector). A linear array is a collection of elements arranged in one direction, producing a rectangular display (see Fig. 14). A curved linear (or convex) array is a modified linear array whose elements are arranged along an arc to permit an enlarged trapezoidal field of view. The elements of these linear type array transducers are excited sequentially group by group with the sweep of the beam in one direction. These linear array transducers are used for radiological and obstetrical examinations. On the other hand, in a phased array transducer the acoustic beam is steered by signals that are applied to the elements with delays, creating a sector display. This transducer is useful for cardiology applications where positioning between the ribs is necessary.

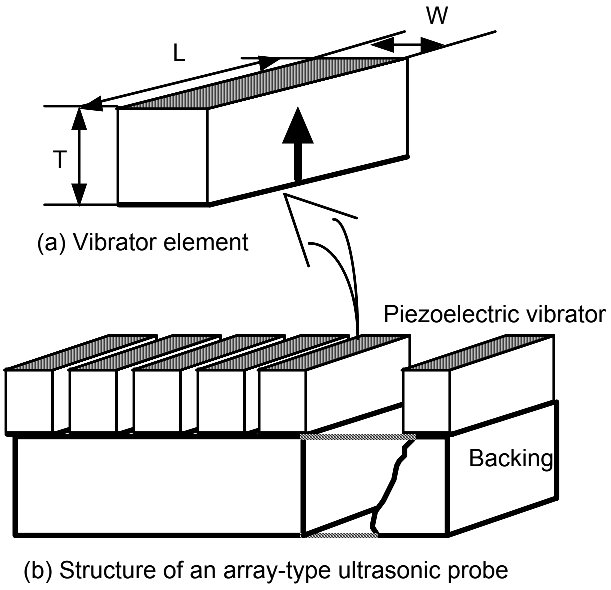

Fig. 14 Linear array type ultrasonic probe.

3.5 Resonators/Filters

When a piezoelectric body vibrates at its resonant frequency it absorbs considerably more energy than at other frequencies resulting in a dramatic decrease in the impedance. This phenomenon enables piezoelectric materials to be used as a wave filter. A filter is required to pass a certain selected frequency band or to block a given band. The band width of a filter fabricated from a piezoelectric material is determined by the square of the coupling coefficient k, that is, it is nearly proportional to k^2. Quartz crystals with a very low k value of about 0.1 can pass very narrow frequency bands of approximately 1% of the center resonance frequency. On the other hand, PZT ceramics with a planar coupling coefficient of about 0.5 can easily pass a band of 10% of the center resonance frequency. The sharpness of the passband is dependent on the mechanical quality factor Q_m of the materials. Quartz also has a very high Q_m of about 10^6 which results in a sharp cut-off to the passband and a well-defined oscillation frequency.

A simple resonator is a thin disc type, electroded on its plane faces and vibrating radially, for filter applications with a center frequency ranging from 200 kHz to 1 MHz and with a bandwidth of several percent of the center frequency. For a frequency of 455 kHz the disc diameter needs to be about 5.6 mm. However, if the required frequency is higher than 10 MHz, other modes of vibration such as the thickness extensional mode are exploited, because of its smaller size. The trapped-energy type filters made from PZT ceramics have been widely used in the intermediate frequency range for applications such as the 10.7 MHz FM radio receiver and transmitter. When the trapped-energy phenomena are utilized, the overtone frequencies are suppressed. The plate is partly covered with electrodes of a specific area and thickness. The fundamental frequency of the thickness mode of the ceramic beneath the electrode is less than that of the unelectroded portion, because of the extra inertia of the electrode mass. The lower-frequency wave of the electroded region cannot propagate into the unelectroded region. The higher-frequency overtones, however, can propagate away into the unelectroded region. This is called the *trapped-energy principle*. Figure 15 shows a schematic drawing of a *trapped-energy filter*. In this structure the top electrode is split so that coupling between the two parts will only be efficient at resonance. More stable filters suitable for telecommunication systems have been made from single crystals such as quartz or $LiTaO_3$.

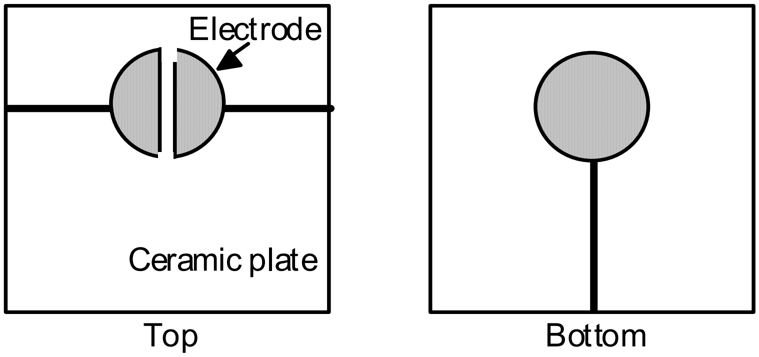

Fig. 15 Schematic drawing of a trapped-energy filter.

4. SURFACE ACOUSTIC WAVE DEVICES

A *surface acoustic wave* (SAW), also called a *Rayleigh wave*, is essentially a coupling between longitudinal and shear waves. The energy carried by the SAW is confined near the surface. An associated electrostatic wave exists for a SAW on a piezoelectric substrate, which allows electroacoustic coupling via a transducer. The advantages of SAW technology are:[23,24)]

(1) The wave can be electroacoustically accessed and tapped at the substrate surface and its velocity is approximately 10^4 times slower than an electromagnetic wave.
(2) The SAW wavelength is on the same order of magnitude as line dimensions produced by photolithography and the lengths for both short and long delays are achievable on reasonably sized substrates.

There is a very broad range of commercial system applications which include front-end and IF (Intermediate Frequency) filters, CATV (Community Antenna Television) and VCR (Video Cassette Recorder) components, synthesizers, analyzers and navigators. In SAW transducers, finger (*interdigital*) electrodes provide the ability to sample or tap the wave and the electrode gap gives the relative delay. A SAW filter is composed of a minimum of two transducers. A schematic of a simple SAW bi-directional filter is shown in Fig. 16. A bi-directional transducer radiates energy equally from each side of the transducer. Energy which is not associated with the received signal is absorbed to eliminate spurious reflection.

Various materials are currently being used for SAW devices. The most popular single-crystal SAW materials are lithium niobate and lithium tantalate. The materials have different properties depending on the cut of the material and the direction of propagation. The fundamental parameters considered when choosing a material for a given device applications are SAW velocity, temperature coefficients of delay (TCD), electromechanical coupling factor and propagation loss. Surface acoustic waves can be generated and detected by spatially periodic, interdigital electrodes on the plane surface of a piezoelectric plate. A periodic electric field is produced when an RF source is connected to the electrode, thus permitting piezoelectric coupling to a traveling surface wave. If an RF source with a frequency, f, is applied to the electrode having periodicity, d, energy conversion from an electrical to mechanical form will be maximum when

$$f = f_0 = v_s / d \ , \qquad (39)$$

where v_s is the SAW velocity and f_0 is the center frequency of the device. The SAW velocity is an important parameter determining the center frequency. Another important parameter for many applications is temperature sensitivity. For example, the temperature stability of the center frequency of SAW bandpass filters is a direct function of the temperature coefficient for the velocity and the delay for the material used. The first-order temperature coefficient of delay is given by:

$$(1/\tau)\cdot(d\tau / dT) = (1/L)\cdot(dL / dT) - (1/v_s)\cdot(dv_s / dT) \ , \qquad (40)$$

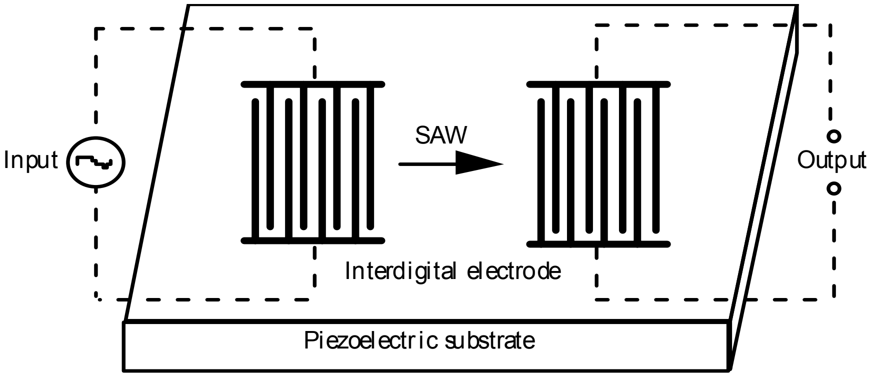

Fig. 16 Fundamental structure of a surface acoustic wave device.

where $\tau = L / v_s$ is the delay time and L is the SAW propagation length. The surface wave coupling factor, k_s^2 , is defined in terms of the change in SAW velocity which occurs when the wave passes across a surface coated with a thin massless conductor, so that the piezoelectric field associated with the wave is effectively short-circuited. The coupling factor, k_s^2 , is expressed by :

$$k_s^2 = 2\,(v_f - v_m) / v_f \ , \qquad (41)$$

where v_f is the free surface wave velocity and v_m the velocity on the metallized surface. In actual SAW applications, the value of k_s^2 relates to the maximum bandwidth obtainable and the amount of signal loss between input and output, which determines the fractional bandwidth as a function of minimum insertion loss for a given material and filter. Propagation loss is one of the major factors that determines the insertion loss of a device and is caused by wave scattering at crystalline defects and surface irregularities. Materials which show high electromechanical coupling factors combined with small temperature coefficients of delay are generally preferred. The free surface velocity, v_0, of the material is a function of cut angle and propagation direction. The TCD is an indication of the frequency shift expected for a transducer due to a temperature change and is also a function of cut angle and propagation direction. The substrate is chosen based on the device design specifications which include operating temperature, fractional bandwidth, and insertion loss.

Piezoelectric single crystals such as 128°Y-X (128°-rotated-Y-cut and X-propagation) - $LiNbO_3$ and X-112°Y (X-cut and 112°-rotated-Y-propagation) - $LiTaO_3$ have been extensively employed as SAW substrates for applications in VIF filters. A c-axis oriented ZnO thin film deposited on a fused quartz, glass or sapphire substrate has also been commercialized for SAW devices. Table 2 summarizes some important material parameters for these SAW materials.

A delay line can be formed from a slice of glass such as PbO or K_2O doped SiO_2 glass in which the velocity of sound is nearly independent of temperature. PZT ceramic transducers are soldered on two metallized edges of the slice of glass. The input transducer converts the electrical signal to a shear acoustic wave which travels through the slice. At the output transducer the wave is reconverted into an electrical signal delayed by the length of time taken to travel around the slice. Such delay lines are used in color TV sets to introduce a delay of approximately 64 µsec and are also employed in videotape recorders.

Table 2 SAW material properties.

	Material	Cut - Propagation direction	k^2 (%)	TCD (ppm/ C)	V_0 (m/s)	ε_r
Single crystal	Quartz	ST - X	0.16	0	3158	4.5
	$LiNbO_3$	128°Y - X	5.5.	-74	3960	35
	$LiTaO_3$	X112°-Y	0.75	-18	3290	42
	$Li_2B_4O_7$	(110)-<001>	0.8	0	3467	9.5
Ceramic	PZT-In$(Li_{3/5}W_{2/5})O_3$		1.0	10	2270	690
	(Pb,Nd)(Ti,Mn,In)O_3		2.6	< 1	2554	225
Thin film	ZnO / glass		0.64	-15	3150	8.5
	ZnO / Sapphire		1.0	-30	5000	8.5

5. PIEZOELECTRIC TRANSFORMERS

When input and output terminals are fabricated on a piezo-device and input/output voltage is changed through the vibration energy transfer, the device is called a *piezoelectric transformer*. Piezoelectric transformers were used in color TVs because of their compact size in comparison with the conventional electromagnetic coil-type transformers. Since serious problems were found initially in the mechanical strength (collapse occurred at the nodal point!) and in heat generation, the development approach was the same as that used for fabricating ceramic actuators. Recent lap-top computers with a liquid crystal display require a very thin, no electromagnetic-noise transformer to start the glow of a fluorescent back-lamp. This application has recently accelerated the development of the piezo-transformer.

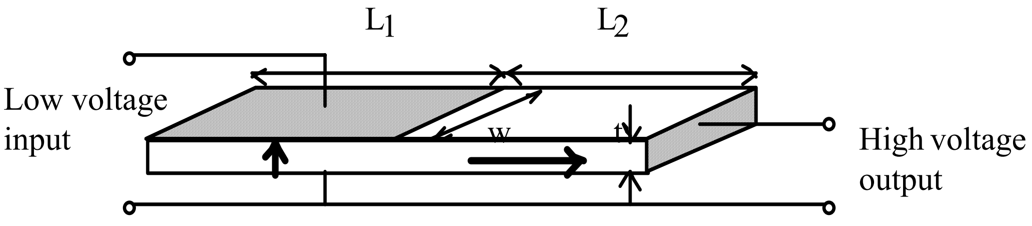

Fig. 17 Piezoelectric transformer proposed by Rosen.

Since the original piezo-transformer was proposed by C. A. Rosen[25)], there have been a variety of such transformers investigated. Figure 17 shows a fundamental structure where two differently-poled parts coexist in one piezoelectric plate. A standing wave with a wavelength equal to the sample length is excited, a half wavelength existing on both the input (L_1) and output (L_2) parts. The voltage rise ratio r (*step-up ratio*) is given for the unloaded condition by :

$$r = (4 / \pi^2)\, k_{31}\, k_{33}\, Q_m\, (L_2 / t)\, [2\sqrt{s_{33}^E / s_{11}^E} / (1 + \sqrt{s_{33}^D / s_{11}^E})]. \qquad (42)$$

The r ratio is increased with an increase of (L_2 / t), where t is the thickness.

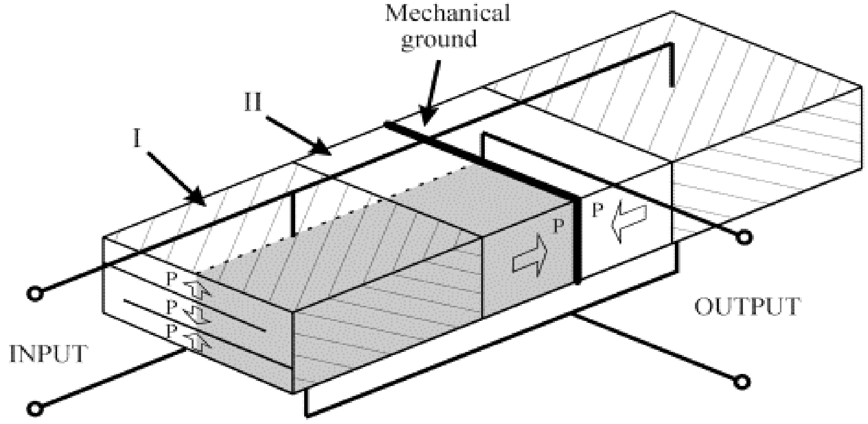

Fig. 18 Multilayer type transformer by NEC.

NEC proposed a multilayer type transformer (Fig. 18) in order to increase the voltage rise ratio.$^{26)}$ Usage of the third order longitudinal mode is another idea to distribute the stress concentration.

6. PIEZOELECTRIC ACTUATORS

Piezoelectric and electrostrictive devices have become key components in smart actuator systems such as precision positioners, miniature ultrasonic motors and adaptive mechanical dampers. This section reviews the developments of piezoelectric and related ceramic actuators with particular focus on the improvement of actuator materials, device designs and applications of the actuators.

Piezoelectric actuators are forming a new field between electronic and structural ceramics.$^{27\text{-}30)}$ Application fields are classified into three categories: positioners, motors and vibration suppressors. The manufacturing precision of optical instruments such as lasers and cameras, and the positioning accuracy for fabricating semiconductor chips, which must be adjusted using solid-state actuators, are generally on the order of 0.1 μm. Regarding conventional electromagnetic motors, tiny motors smaller than 1 cm^3 are often required in office or factory automation equipment and are rather difficult to produce with sufficient energy efficiency. Ultrasonic motors whose efficiency is insensitive to size are considered superior in the mini-motor area. Vibration suppression in space structures and military vehicles using piezoelectric actuators is another promising field of application.

New solid-state displacement transducers controlled by temperature (shape memory alloy) or magnetic field (magnetostrictive alloy) have been proposed, but are generally inferior to the piezoelectric/electrostrictive ceramic actuators because of current technological trends aimed at reduced driving power and miniaturization.$^{30)}$ The shape memory actuator is too slow in response with a very low energy efficiency, while the magnetostrictor requires a driving coil which is very bulky and generates magnetic noise.

6.1 Ceramic Actuator Materials

Actuator materials are classified into three categories; piezoelectric, electrostrictive and phase-change materials. Modified lead zirconate titanate [PZT, $Pb(Zr,Ti)O_3$] ceramics are currently the leading materials for piezoelectric applications. The PLZT [(Pb,La)(Zr,Ti)O_3] 7/62/38 compound is one such composition.31) The strain curve is shown in Fig.19(a) left. When the applied field is small, the induced strain x is nearly proportional to the field E (x = d E, where d is called the piezoelectric constant). As the field becomes larger (i.e., greater than about 1 kV/cm), however, the strain curve deviates from this linear trend and significant hysteresis is exhibited due to polarization reorientation. This sometimes limits the use of such materials for actuator applications that require nonhysteretic response.

An interesting new family of actuators has been fabricated in Germany from the barium stannate titanate system [Ba(Sn,Ti)O_3].32) The useful property of Ba($Sn_{0.15}Ti_{0.85}$)O_3 is its unusual strain curve, in which the domain reorientation occurs only at low fields, and there is then a long linear range at higher fields [Fig.19(a) right]; that is, the coercive field is unusually small. Moreover, this system is particularly intriguing since it contains no Pb ions, an essential feature as ecological concerns grow in the future.

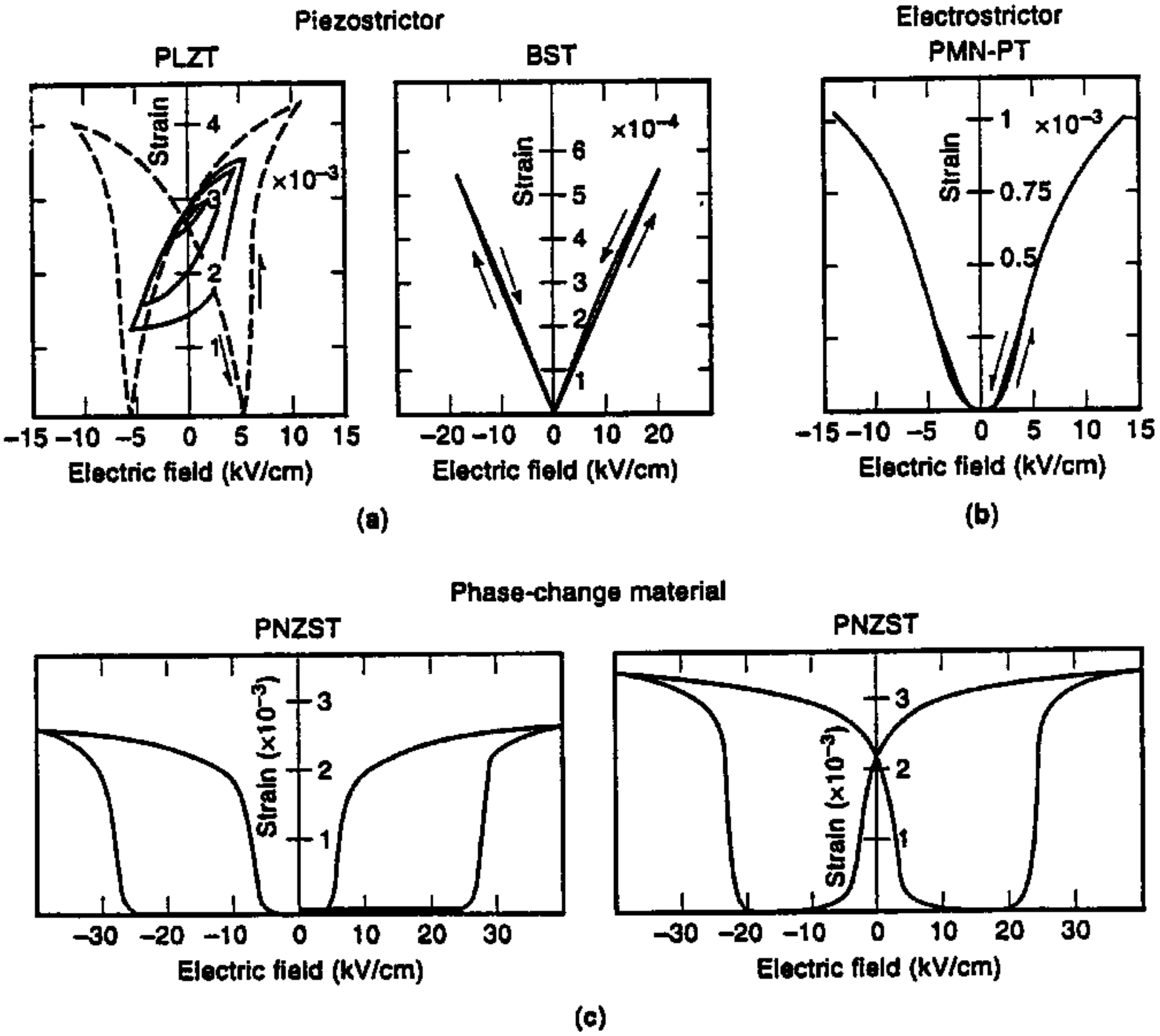

Fig. 19 Electric field-induced strains in ceramics; (a) Piezoelectric (Pb,La)(Zr,Ti)O_3 and Ba(Sn,Ti)O_3, (b) Electrostrictive Pb($Mg_{1/3}Nb_{2/3}$,Ti)O_3, (c) Phase-change material Pb(Zr,Sn,Ti)O_3.

The second category of actuators is based on electrostriction as exhibited by PMN [$Pb(Mg_{1/3}Nb_{2/3})O_3$] based ceramics. Although it is a second-order phenomenon of electromechanical coupling ($x = M E^2$, where M is called the electrostrictive coefficient), the induced strain can be extraordinarily large (more than 0.1 %).33) An attractive feature of these materials is the near absence of hysteresis [Fig.19(b)]. The superiority of PMN to PZT was demonstrated in a Scanning Tunneling Microscope (STM).34) The STM probe was scanned mechanically by a PMN actuator, which produces only extremely small distortion of the image, even when the probe was scanned in the opposite direction due to a negligibly small hysteresis.

The third category is based on phase-change-related strains, that is, polarization-induced by switching from an antiferroelectric to a ferroelectric state.35) Figure 19(c) shows the field-induced strain curves taken for the lead zirconate stannate based system [$Pb_{0.99}Nb_{0.02}((Zr_xSn_{1-x})_{1-y}Ti_y)_{0.98}O_3$]. The longitudinally induced strain reaches more than 0.3%, which is much larger than that exhibited by normal piezostrictors or electrostrictors. A rectangular-shaped hysteresis in Fig. 19(c) left characterizes the response of these devices which are referred to as "digital displacement transducers" because of the two on/off strain states. Moreover, this field-induced transition is accompanied by a shape memory effect for appropriate compositions [Fig. 19(c) right]. Once the ferroelectric phase has been induced, the material "memorizes" its ferroelectric state even under zero-field conditions, although it can be erased with the application of a small reverse bias field.36) This shape memory ceramic is used in energy saving actuators. A latching relay was composed of a shape memory ceramic unimorph and a mechanical snap action switch, which was driven by a pulse voltage of 4 ms duration. Compared with the conventional electromagnetic relays, the new relay was much simpler and more compact in structure with almost the same response time.

6.2 Actuator Designs

Two of the most popular actuator designs are the multilayers37) and bimorphs (see Fig. 20). The multilayer, in which roughly 100 thin piezoelectric/electrostrictive ceramic sheets are stacked together, has the advantages of low driving voltage (100 V), quick response (10 µs), high generative force (1000 N), and high electromechanical coupling. But the displacement, on the order of 10 µm, is not sufficient for some applications. This contrasts with the characteristics of the bimorph which consists of multiple piezoelectric and elastic plates bonded together to generate a large bending displacement of several hundred µm, but has relatively low response time (1 ms) and generative force (1 N).

A 3-D positioning actuator with a stacked structure as pictured in Fig. 21 was proposed by a German company, where shear strain was utilized to generate the x and y displacements.38) Polymer-packed PZT bimorphs have been commercialized by ACX for vibration reduction/control applications in smart structures.39)

A composite actuator structure called the "moonie" (or "cymbal") has been developed to provide characteristics intermediate between the multilayer and bimorph actuators; this transducer exhibits an order of magnitude larger displacement than the multilayer, and much larger generative force with quicker response than the bimorph.40) The device consists of a thin multilayer piezoelectric element and two metal plates with narrow moon-shaped cavities bonded together as shown in Fig. 20. The moonie with a size of 5 x 5 x 2.5 mm^3 can generate a 20 µm displacement under 60 V, eight times as large as the generative displacement produced by a multilayer of the same size.41) This new compact actuator has been utilized in a miniaturized laser beam scanner.

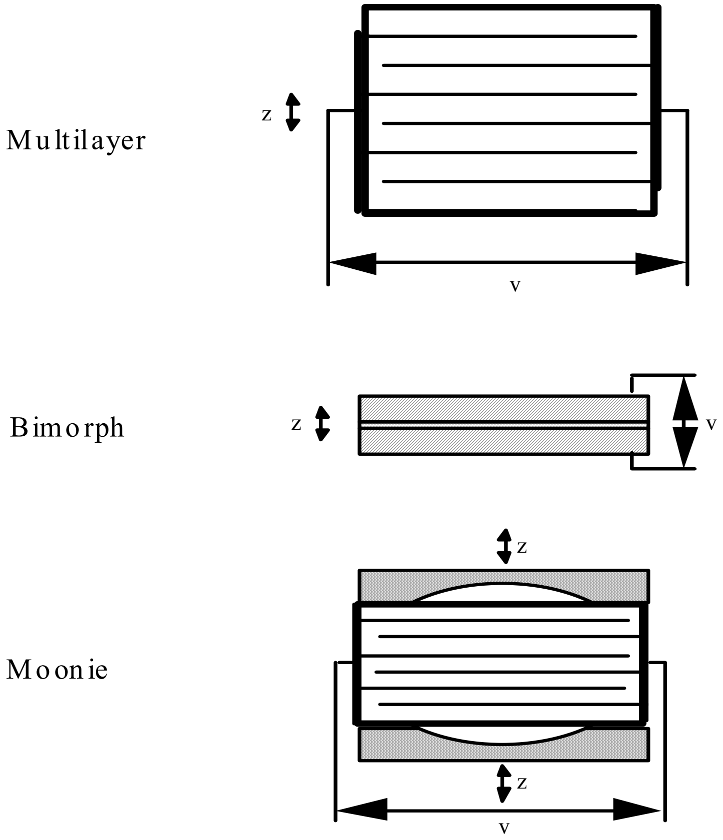

Fig. 20 Typical designs for ceramic actuators: multilayer, bimorph and moonie.

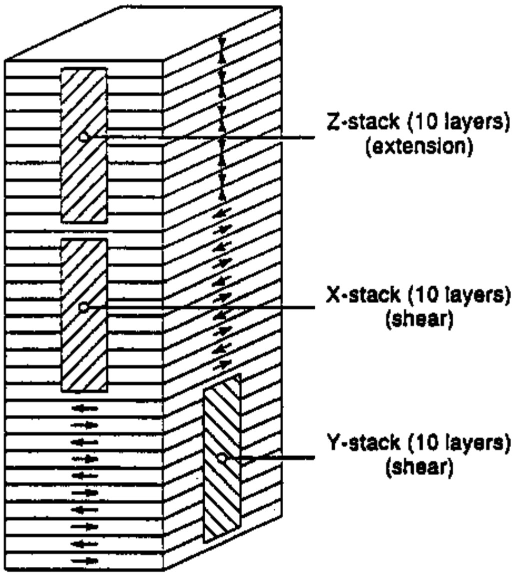

Fig. 21 3-D positioning multilayer actuator. Notice that the x- and y-stacks are using shear mode with the spontaneous polarization perpendicular to the applied electric field direction.

6.3 Drive/Control Techniques

Piezoelectric/electrostrictive actuators may be classified into two categories, based on the type of driving voltage applied to the device and the nature of the strain induced by the voltage (Fig. 22): (1) rigid displacement devices for which the strain is induced unidirectionally along the direction of the applied DC field, and (2) resonating displacement devices for which the alternating strain is excited by an AC field at the mechanical resonance frequency (ultrasonic motors). The first can be further divided into two types: servo displacement transducers (positioners) controlled by a feedback system through a position-detection signal, and pulse drive motors operated in a simple on/off switching mode, exemplified by dot-matrix printers.

The material requirements for these classes of devices are somewhat different, and certain compounds will be better suited to particular applications. The ultrasonic motor, for instance, requires a very hard piezoelectric with a high mechanical quality factor Q_M, to suppress heat generation. Driving the motor at the antiresonance frequency, rather than at resonance, is also an intriguing technique to reduce the load on the piezoceramic and the power supply.42) The servo displacement transducer suffers most from strain hysteresis and, therefore, a PMN electrostrictor is used for this purpose. The pulse drive motor requires a low permittivity material aimed at quick response with a certain power supply rather than a small hysteresis, so soft PZT piezoelectrics are preferred rather than the high-permittivity PMN for this application.

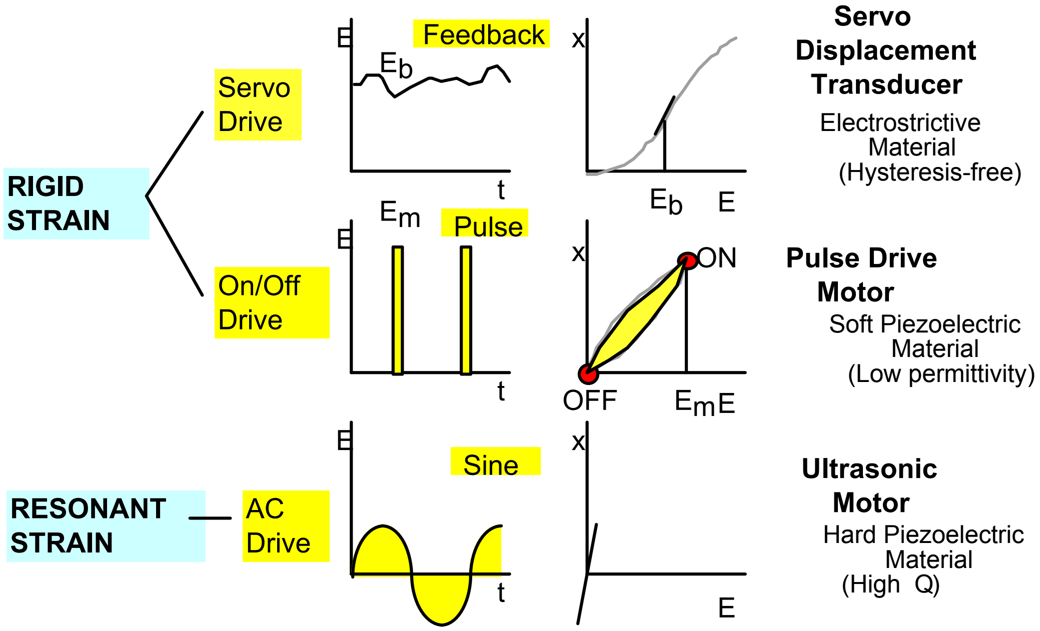

Fig. 22 Classification of piezoelectric/electrostrictive actuators.

Pulse drive techniques for ceramic actuators are very important for improving the response of the device.43,44) Figure 23 shows transient vibrations of a bimorph excited after a pseudo-step voltage is applied. The rise time is varied around the resonance period (n is the time scale with a unit of $T_0/2$, where T_0 stands for the resonance period). It is concluded that the overshoot and ringing of the tip displacement is completely suppressed when the rise time is precisely adjusted to the resonance period of the piezo-device (i.e., for n = 2).43) A flight actuator was developed using a pulse-drive piezoelectric element and a steel ball. A 5 µm rapid displacement induced in a multilayer actuator can hit a 2 mm steel ball up to 20 mm in height. A dot-matrix printer head has been developed using a flight actuator as shown in Fig. 24.45) By changing the drive voltage pulse width, the movement of the armature was easily controlled to realize no vibrational ringing or double hitting.

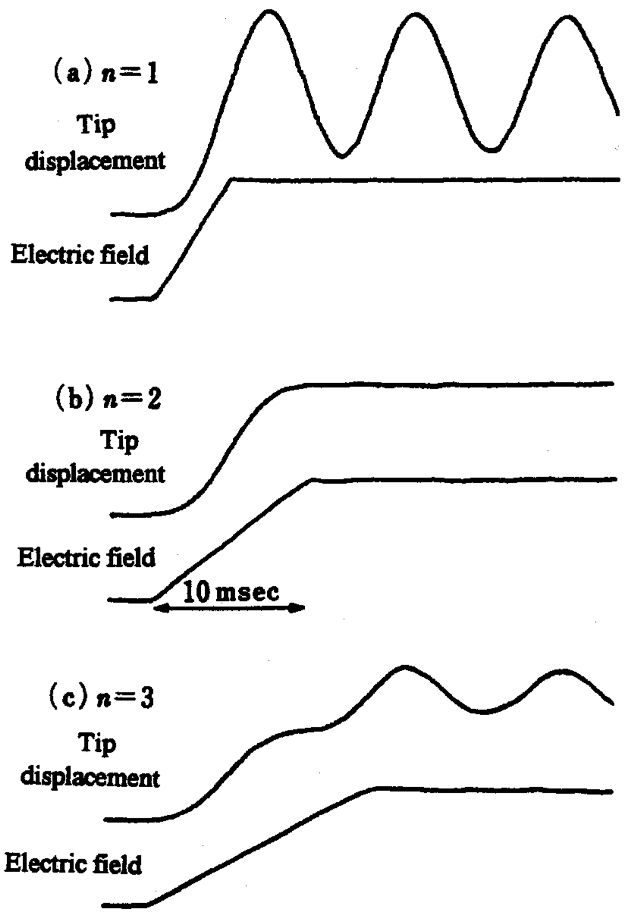

Fig. 23 Transient vibration of a bimorph excited after a pseudo-step voltage applied. n is a time scale with a unit of half of the resonance period, i.e., 2n = resonance period.

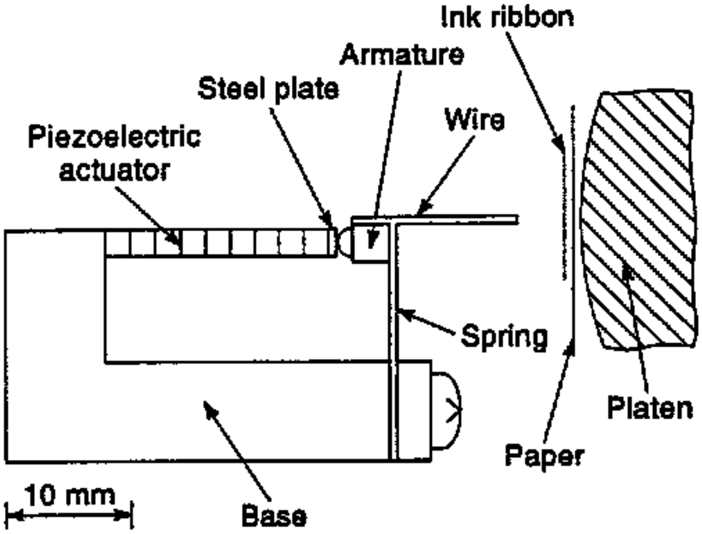

Fig. 24 Dot-matrix printer head using a flight actuator mechanism.

6.4 Device Applications

Servo Displacement Transducers

A typical example is found in a space truss structure proposed by the Jet Propulsion Laboratory.46) A stacked PMN actuator was installed at each truss nodal point and operated so that unnecessary mechanical vibration was suppressed immediately. A "hubble" telescope has also been proposed using multilayer PMN electrostrictive actuators to control the phase of the incident light wave in the field of optical information processing (Fig. 25).47) The PMN electrostrictor provided superior adjustment of the telescope image because of negligible strain hysteresis.

The U.S. Army is interested in developing a rotor control system in helicopters. Figure 26 shows a bearingless rotor flexbeam with attached piezoelectric strips.48) Various types of PZT-sandwiched beam structures have been investigated for such a flexbeam application and for active vibration control.49)

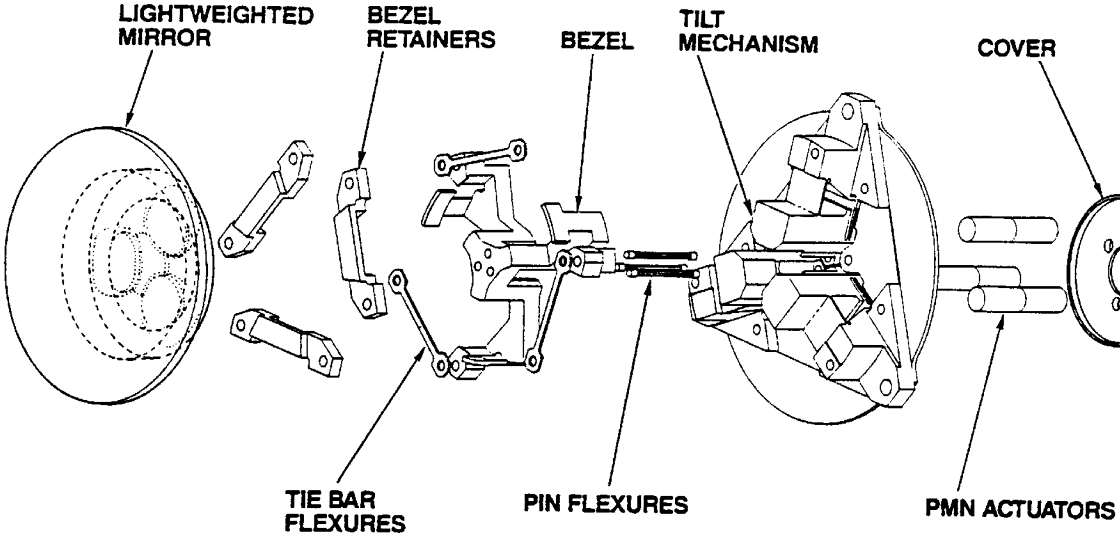

Fig. 25 "Hubble" telescope using three PMN electrostrictive actuators for optical image correction.

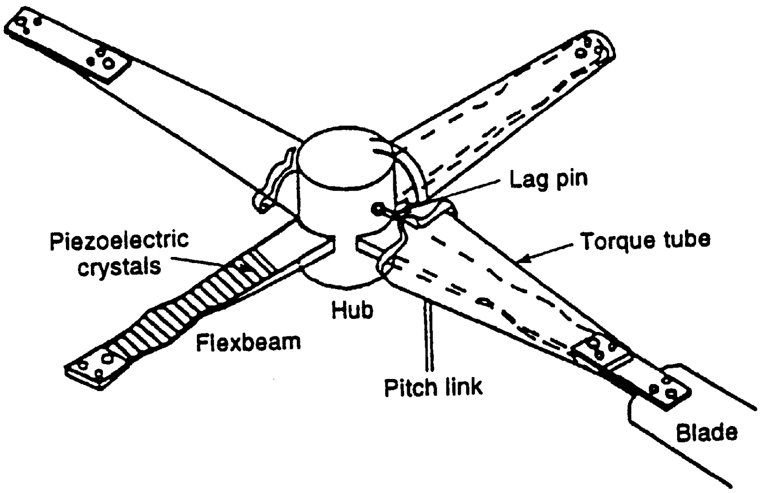

Fig. 26 Bearingless rotor flexbeam with attached piezoelectric strips. A slight change in the blade angle provides for enhanced controllability.

Concerning home appliance applications, there is already a large market in VCR systems. The requirement for high quality images has become very stringent for VCRs especially when played in still, slow or quick mode. As illustrated in Fig. 27, when the tape is running at a speed different from the normal speed, the head trace deviates from the recording track depending on the velocity difference. Thus the head traces on the guard band, generating *guard band noise*.50) The auto tracking scan system by Ampex operates with a piezoelectric actuator so that the head follows the recording track. The piezoelectric device generates no magnetic noise.

Bimorph structures are commonly used for this tracking actuator because of their large displacement. However, special care has been taken not to produce a *spacing angle* between the head and the tape, because a single bimorph exhibits deflection with slight rotation. Various designs have been proposed to produce a completely parallel motion.

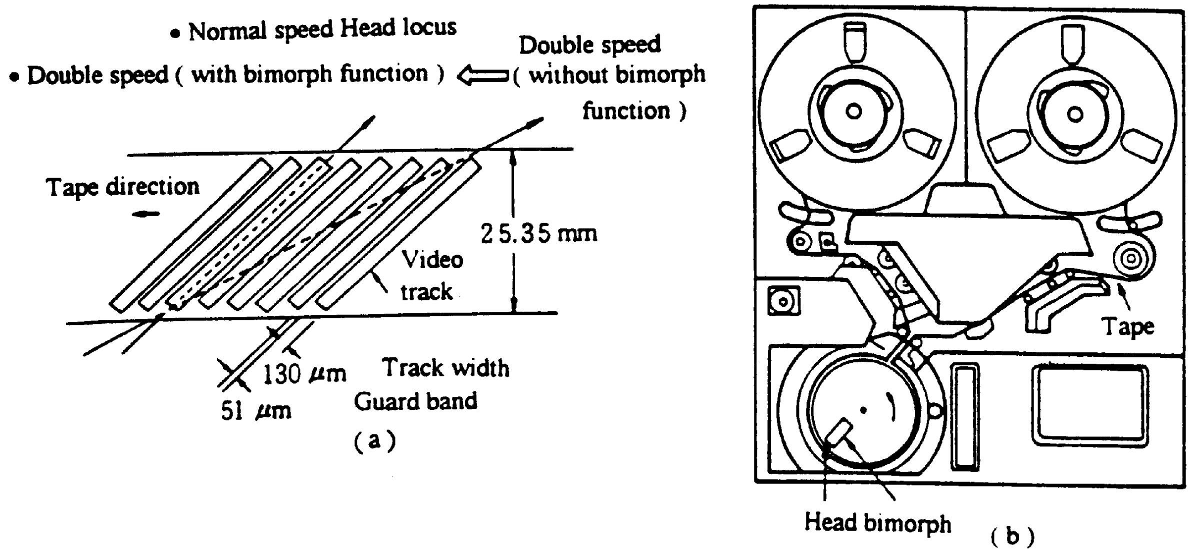

Fig. 27 Locus of the video head and the function of the piezo-actuator.

Pulse Drive Motors

A dot matrix printer is the first widely-commercialized product using ceramic actuators. Each character formed by such a printer is composed of a 24 x 24 dot matrix. A printing ribbon is subsequently impacted by a multiwire array. A sketch of the printer head appears in Fig. 28(a).51) The printing element is composed of a multilayer piezoelectric device, in which 100 thin ceramic sheets 100 μm in thickness are stacked, together with a sophisticated magnification mechanism [Fig. 28(b)]. The magnification unit is based on a monolithic hinge lever with a magnification of 30, resulting in an amplified displacement of 0.5 mm and an energy transfer efficiency greater than 50%.

A piezoelectric camera shutter is currently the largest production item (Fig. 29). A piece of piezoelectric bimorph can open and close the shutter in a milli-second through a mechanical wing mechanism.52)

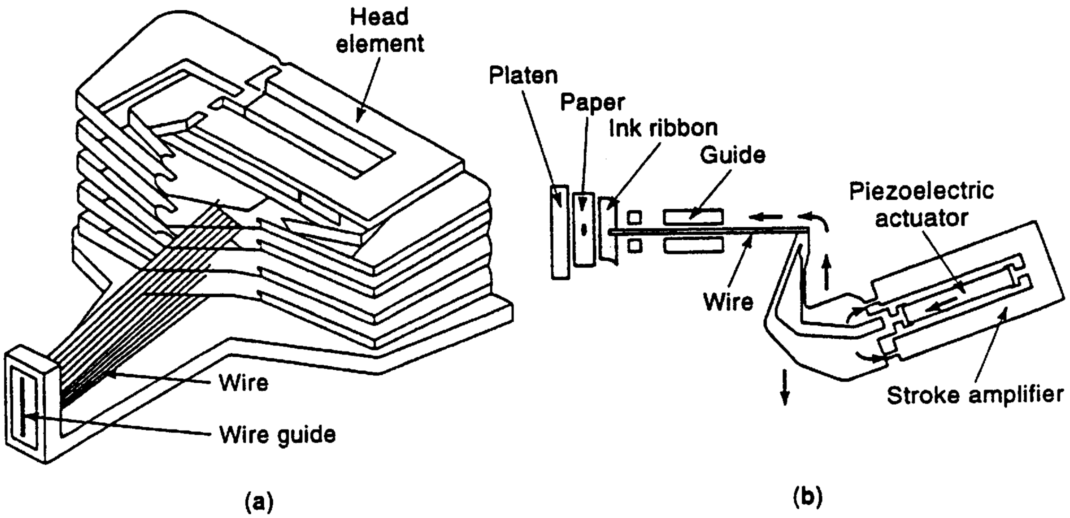

Fig. 28 Structure of a printer head (a), and a differential-type piezoelectric printer-head element (b). A sophisticated monolithic hinge lever mechanism amplifies the actuator displacement by 30 times.

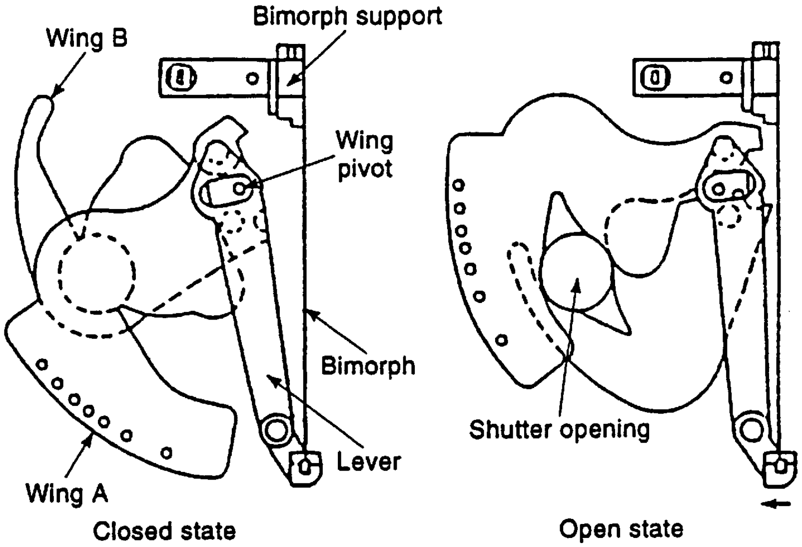

Fig. 29 Camera shutter mechanism using a piezoelectric bimorph actuator.

Toyota developed a Piezo TEMS (Toyota Electronic Modulated Suspension), which is responsive to each protrusion on the road in adjusting the damping condition, and installed it on a "Celcio (equivalent to Lexus, internationally)" in 1989.53) In general, as the damping force of a shock absorber in an automobile is increased (i.e., "hard" damper), the controllability and stability of a vehicle are improved. However, comfort is sacrificed because the road roughness is easily transferred to the passengers. The purpose of the electronically controlled shock absorber is to obtain both controllability and comfort simultaneously. Usually the system is set to provide a low damping force ("soft") so as to improve comfort, and the damping force is changed to a high position according to the road condition and the car speed to improve the controllability. In order to respond to a road protrusion, a very high response of the sensor and actuator combination is required.

Figure 30 shows the structure of the electronically controlled shock absorber. The sensor is composed of 5 layers of 0.5 mm thick PZT disks. The detecting speed of the road roughness is about 2 msec and the resolution of the up-down deviation is 2 mm. The actuator is made of 88 layers of 0.5 mm thick disks. Applying 500 V generates a displacement of about 50 μm, which is magnified by 40 times through a piston and plunger pin combination. This stroke pushes the change valve of the damping force down, then opens the bypass oil route, leading to the decrease of the flow resistance (i.e., "soft").

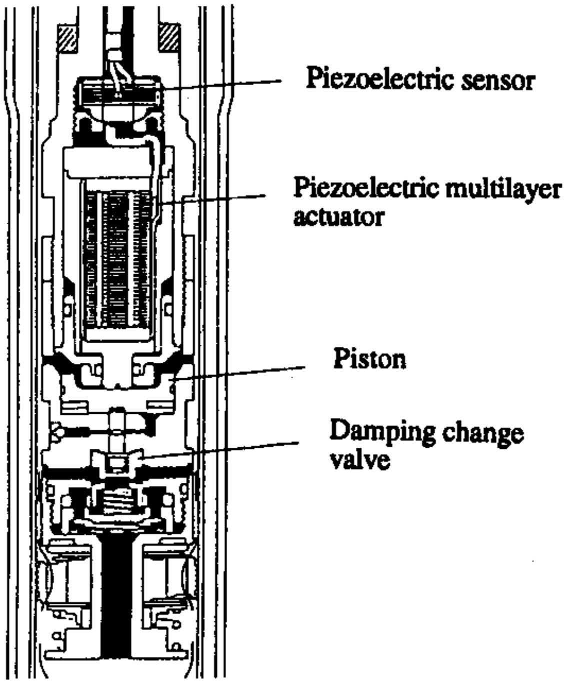

Fig. 30 Electronic modulated suspension by Toyota.

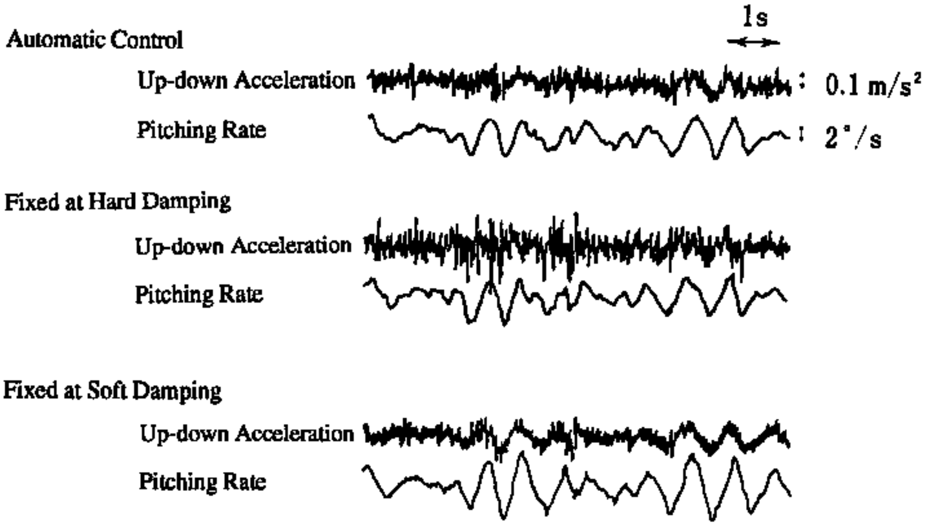

Fig. 31 Function of the adaptive suspension system.

Figure 31 illustrates the operation of the suspension system. The up-down acceleration and pitching rate were monitored when the vehicle was driven on a rough road. When the TEMS system was used (top figure), the up-down acceleration was suppressed to as small as the condition fixed at "soft," providing comfort. At the same time, the pitching rate was also suppressed to as small as the condition fixed at "hard," leading to better controllability.

Figure 32 shows a walking piezo motor with 4 multilayer actuators.54) The two shorter actuators function as clamps and the longer two provide the movement by an inchworm mechanism.

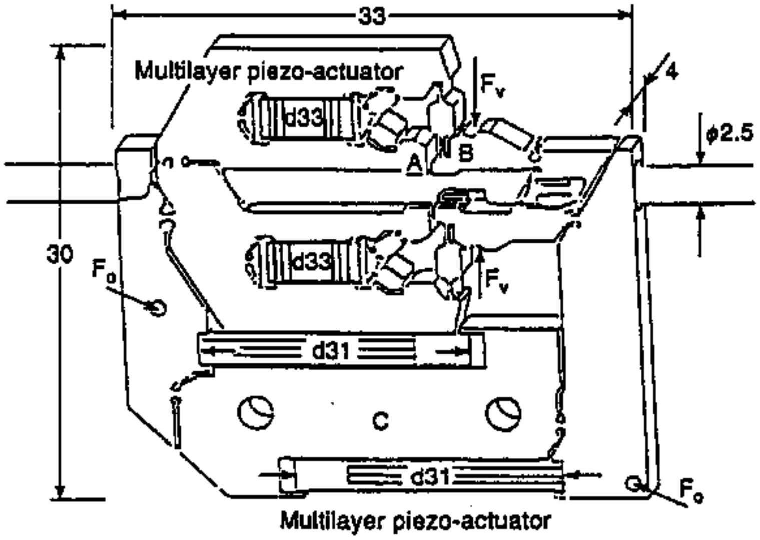

Fig. 32 Walking piezo motor using an inchworm mechanism with 4 multilayer piezoelectric actuators by Philips.

Ultrasonic Motors

(a) Background

Electromagnetic motors were invented more than a hundred years ago. While these motors still dominate the industry, a drastic improvement cannot be expected except through new discoveries in magnetic or superconducting materials. Regarding conventional electromagnetic motors, tiny motors smaller than 1cm^3 are rather difficult to produce with sufficient energy efficiency. Therefore, a new class of motors using high power ultrasonic energy, the ultrasonic motor, is gaining wide- spread attention. Ultrasonic motors made with piezoceramics whose efficiency is insensitive to size are superior in the mini-motor area. Figure 33 shows the basic construction of most ultrasonic motors, which consist of a high-frequency power supply, a vibrator and a slider. The vibrator is composed of a piezoelectric driving component and an elastic vibratory part, and the slider is composed of an elastic moving part and a friction coat.

Although there had been some earlier attempts, the first practical ultrasonic motor was proposed by H. V. Barth of IBM in 1973.55) The rotor was pressed against two horns placed at different locations. By exciting one of the horns, the rotor was driven in one direction, and by exciting the other horn, the rotation direction was reversed. Various mechanisms based on virtually the same principle were proposed by V. V. Lavrinenko56) and P. E. Vasiliev57) in the former USSR. Because of difficulty in maintaining a constant vibration amplitude with temperature rise, wear and tear, the motors were not of much practical use at that time.

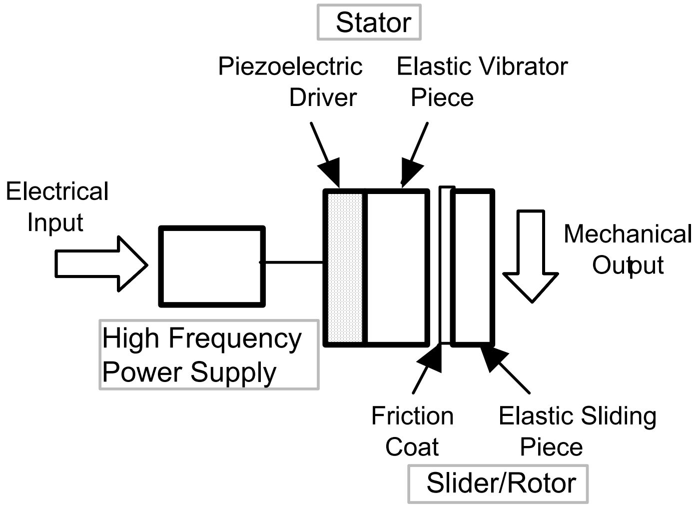

Fig. 33 Fundamental construction of an ultrasonic motor.

In the 1980s, with increasing chip pattern density, the semiconductor industry began to demand much more precise and sophisticated positioners which would not generate magnetic field noise. This urgent need accelerated the development of ultrasonic motors. Another advantage of ultrasonic motors over conventional electromagnetic motors with expensive copper coils is the improved availability of piezoelectric ceramics at reasonable cost. Japanese manufacturers are currently producing piezoelectric buzzers at about 30 - 40 cents per unit.

Let us summarize the merits and demerits of the ultrasonic motor:

Merits

1. Low speed and high torque -- Direct drive
2. Quick response, wide velocity range, hard brake and no backlash
   -- Excellent controllability
   -- Fine position resolution
3. High power / weight ratio and high efficiency
4. Quiet drive
5. Compact size and light weight
6. Simple structure and easy production process
7. Negligible effect from external magnetic or radioactive fields, and also no generation of these fields

Demerits

8. Necessity for a high frequency power supply
9. Less durability due to frictional drive
10. Drooping torque vs. speed characteristics

(b) Classification and Principles of Ultrasonic Motors

From a customer's point of view, there are rotary and linear type motors. If we categorize them according to the vibrator shape, there are rod type, π-shaped, ring (square) and cylinder types. Two categories are being investigated for ultrasonic motors from a vibration characteristic viewpoint: a standing-wave type and a propagating-wave type. Refresh your memory on the wave formulas. The standing wave is expressed by

$$u_S(x,t) = A \cos kx \cdot \cos \omega t, \qquad (43)$$

while the propagating wave is expressed as

$$u_p(x,t) = A \cos (kx - \omega t). \qquad (44)$$

Using a trigonometric relation, Eq. (44) can be transformed as

$$u_p(x,t) = A \cos kx \cdot \cos \omega t + A \cos (kx - \pi/2) \cdot \cos (\omega t - \pi/2). \qquad (45)$$

This leads to an important result, a propagating wave can be generated by superimposing two standing waves whose phases differ by 90 degrees both in time and in space. This principle is necessary to generate a propagating wave on a limited volume/size substance, because only standing waves can be excited stably in a solid medium of finite size.

The standing-wave type is sometimes referred to as a vibratory-coupler type or a "woodpecker" type, where a vibratory piece is connected to a piezoelectric driver and the tip portion generates a flat-elliptical movement. Figure 34 shows a simple model proposed by T. Sashida.[58)] A vibratory piece is attached to a rotor or a slider with a slight cant angle. When a vibration is excited at the piezoelectric vibrator, the vibratory piece generates bending because of restriction by the rotor, so that the tip moves along the rotor face between A --> B, and freely between B --> A. If the vibratory piece and the piezo-vibrator are tuned properly, they form a resonating structure, which is an elliptical locus. Therefore, only the duration A --> B provides a unidirectional force to the rotor through friction, and, therefore, an intermittent rotational torque or thrust. However, because of the inertia of the rotor, the rotation speed ripple is not observed to be large. The standing-wave type, in general, is low in cost (one vibration source) and has high efficiency (up to 98% theoretically), but lacks control in both the clockwise and counterclockwise directions.

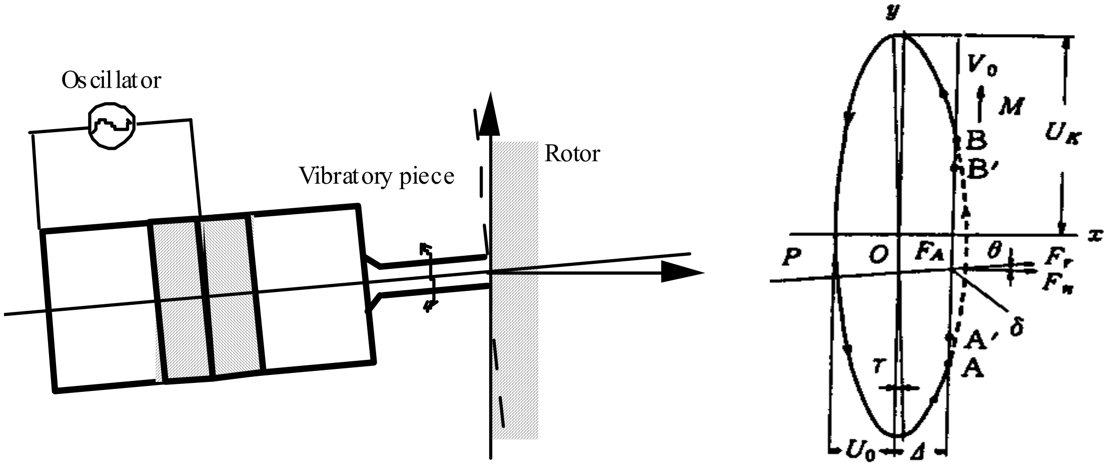

(a) (b)

Fig. 34 Vibratory coupler type motor (a) and its tip locus (b).

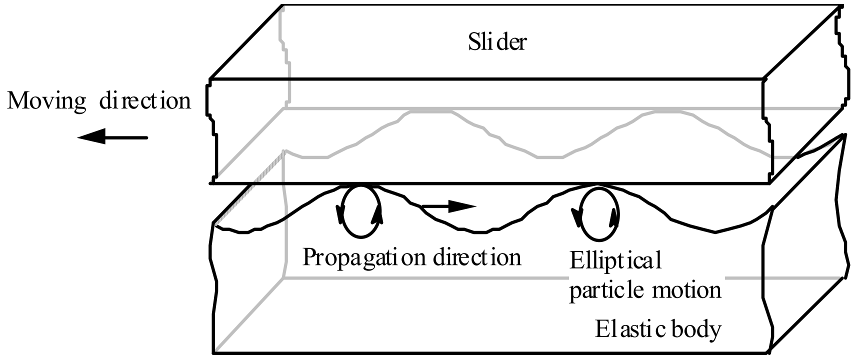

Fig. 35 Principle of the propagating wave type motor.

By comparison, the propagating-wave type (a surface-wave or "surfing" type) combines two standing waves with a 90 degree phase difference both in time and in space. The principle is shown in Fig. 35. A surface particle of the elastic body draws an elliptical locus due to the coupling of longitudinal and transverse waves. This type requires, in general, two vibration sources to generate one propagating wave, leading to low efficiency (not more than 50%), but it is controllable in both rotational directions.

(c) Various Ultrasonic Motors

T. Sashida developed a rotary type motor similar to the fundamental structure.58) Four vibratory pieces were installed on the edge face of a cylindrical vibrator, and pressed onto the rotor. This is one of the prototypes which triggered the present active development of ultrasonic motors. A rotation speed of 1500 rpm, torque of 0.08 N·m and an output of 12 W (efficiency 40%) are obtained under an input of 30 W at 35 kHz. This type of ultrasonic motor can provide a speed much higher than the inchworm types, because of its high operating frequency and amplified vibration displacement at the resonance frequency.

Hitachi Maxel significantly improved the torque and efficiency by using a torsional coupler replacing Sashida's vibratory pieces (Fig. 36), and by increasing the pressing force with a bolt.59) The torsional coupler looks like an old fashioned TV channel knob, consisting of two legs which transform longitudinal vibration generated by the Langevin vibrator to a bending mode of the knob disk, and a vibratory extruder. Notice that this extruder is aligned with a certain cant angle to the legs, which transforms the bending to a torsional vibration. This transverse moment coupled with the bending up-down motion leads to an elliptical rotation on the tip portion, as illustrated in Fig. 36(b). The optimum pressing force to get the maximum thrust is obtained, when the ellipse locus is deformed roughly by half. A motor 30 mm x 60 mm in size and with a 20 - 30° in cant angle between leg and vibratory piece can generate torques as high as 1.3 N·m with an efficiency of 80%. However, this type provides only unidirectional rotation. Notice that even though the drive of the motor is intermittent, the output rotation becomes very smooth because of the inertia of the rotor.

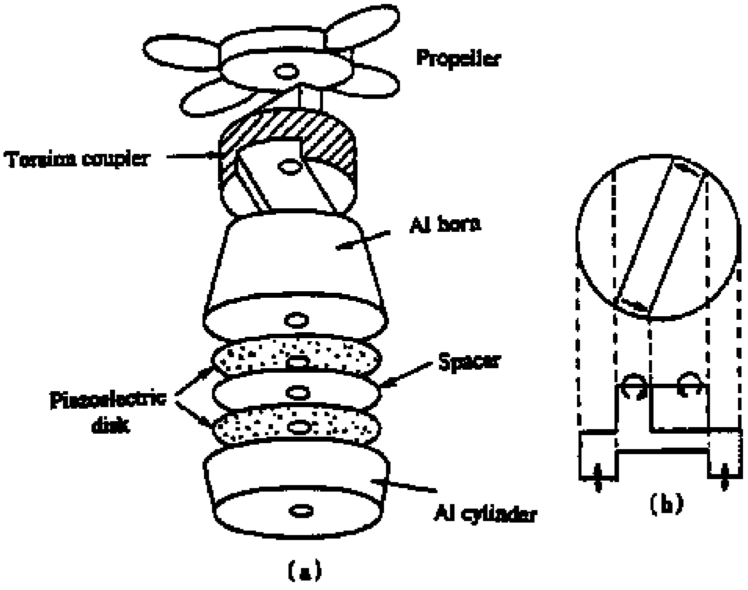

Fig. 36 Torsional coupler ultrasonic motor (a) and the motion of the torsional coupler (b).

A compact ultrasonic rotory motor, as tiny as 3 mm in diameter, has been developed at the Pennsylvania State University. As shown in Fig. 37, the stator consists of a piezoelectric ring and two concave/convex metal endcaps with "windmill" shaped slots bonded together, so as to generate a coupling of the up-down and torsional vibrations.60) Since the number of components is reduced and the fabrication process is much simplified, the fabrication price is decreased remarkably, and a disposable design becomes feasible. When driven at 160 kHz, a maximum revolution of 600 rpm and a maximum torque of 1 mN·m were obtained for a 11 mm diameter motor.

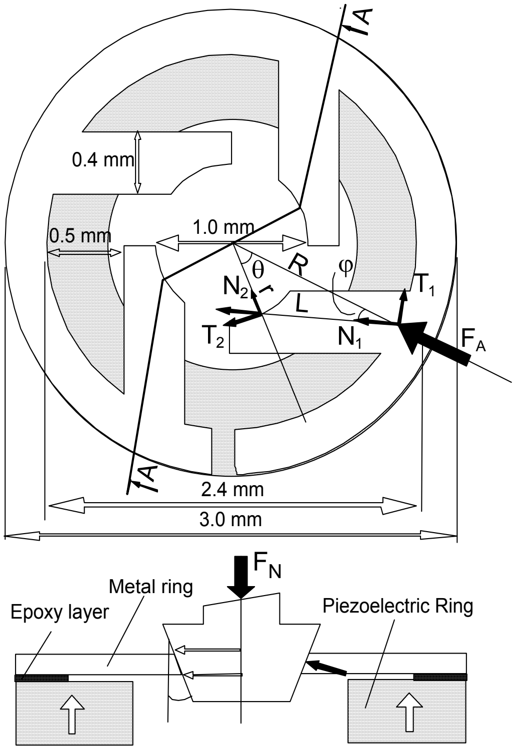

Fig. 37 "Windmill" motor with a disk-shaped torsional coupler.

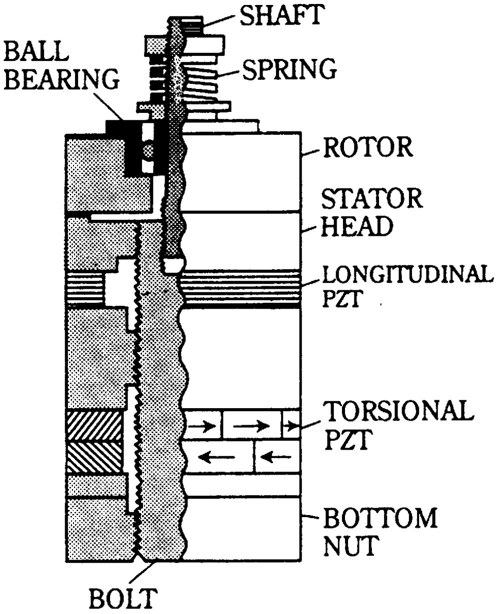

Fig. 38 Two-vibration-mode coupled type motor.

Tokin developed a piezoelectric ceramic cylinder for a torsional vibrator.61) Using an interdigital type electrode pattern printed with a 45^{o} cant angle on the cylinder surface, torsion vibration was generated, which is applicable for a simple ultrasonic motor.

Ueha proposed a two-vibration-mode coupled type (Fig. 38), that is, a torsional Langevin vibrator was combined with three multilayer actuators to generate larger longitudinal and transverse surface displacements of the stator, as well as to control their phase difference.62) The phase change can change the rotation direction.

Uchino invented a π-shaped linear motor.63) This linear motor is equipped with a multilayer piezoelectric actuator and fork-shaped metallic legs as shown in Fig. 39. Since there is a slight difference in the mechanical resonance frequency between the two legs, the phase difference between the bending vibrations of both legs can be controlled by changing the drive frequency. The walking slider moves in a way similar to a horse using its fore and hind legs when trotting. A test motor, 20 x 20 x 5 mm^3 in dimension, exhibits a maximum speed of 20 cm/s and a maximum thrust of 0.2 kgf with a maximum efficiency of 20%, when driven at 98kHz at 6V (actual power = 0.7 W). This motor has been employed in a precision X-Y stage.

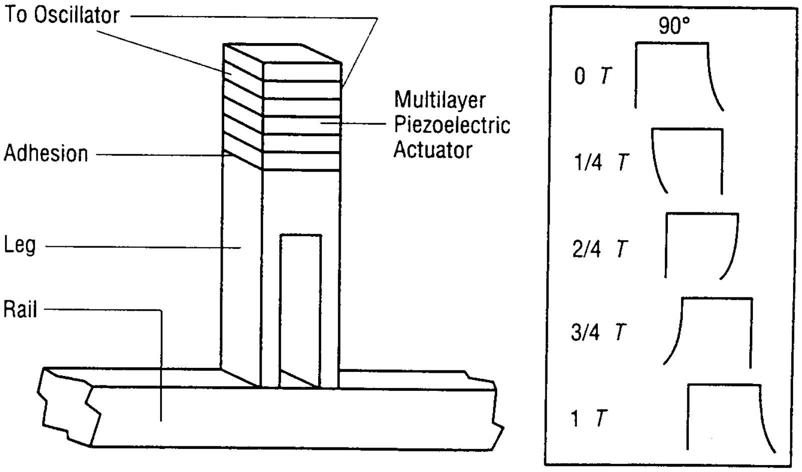

Fig. 39 π-shaped linear ultrasonic motor. (a) construction and (b) walking principle. Note the 90 degree phase difference of two legs similar to that associated with human walking.

Tomikawa's rectangular plate motor is also intriguing.64) As shown in Fig. 40, a combination of the two modes of vibration forms an elliptical displacement. The two modes chosen were the 1st longitudinal mode (L_1 mode) and the 8th bending mode (B_8), whose resonance frequencies were almost the same. By applying voltages with a phase difference of 90 degrees to the L-mode and B-mode drive electrodes, elliptical motion in the same direction can be obtained at both ends of this plate, leading to rotation of the rollers in contact with these points. Anticipated applications are paper or card senders.

Figure 41 shows the famous Sashida motor.65) By means of the traveling elastic wave induced by a thin piezoelectric ring, a ring-type slider in contact with the "rippled" surface of the elastic body bonded onto the piezoelectric is driven in both directions by exchanging the sine and cosine voltage inputs. Another advantage is its thin design, which makes it suitable for installation in cameras as an automatic focusing device. Eighty percent of the exchange lenses in Canon's "EOS" camera series have already been replaced by the ultrasonic motor mechanism.

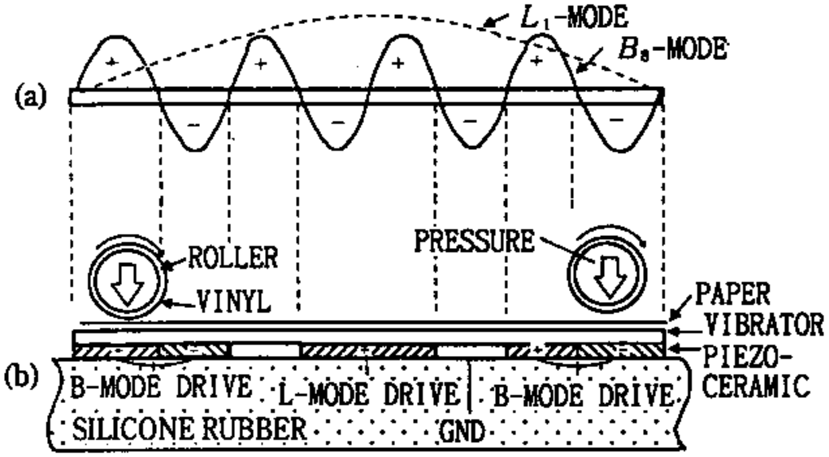

Fig. 40 L_1 and B_8 double-mode vibrator motor.

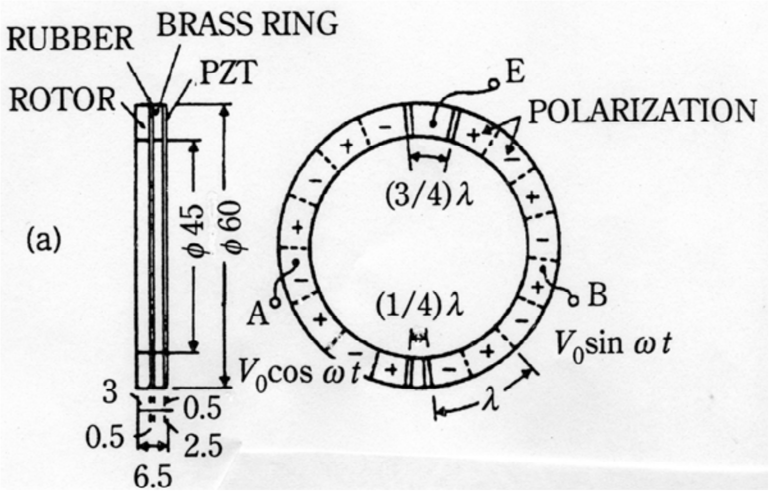

Fig. 41 Stator structure of Sashida's motor.

The PZT piezoelectric ring is divided into 16 positively and negatively poled regions and two asymmetric electrode gap regions so as to generate a 9th mode propagating wave at 44 kHz. A proto type was composed of a brass ring of 60 mm in outer diameter, 45 mm in inner diameter and 2.5 mm in thickness, bonded onto a PZT ceramic ring of 0.5 mm in thickness with divided electrodes on the back-side. The rotor was made of polymer coated with hard rubber or polyurethane. Figure 42 shows Sashida's motor characteristics.

Canon utilized the "surfing" motor for a camera automatic focusing mechanism, installing the ring motor compactly in the lens frame. It is noteworthy that the stator elastic ring has many teeth, which can magnify the transverse elliptical displacement and improve the speed. The lens position can be shifted back and forth with a screw mechanism. The advantages of this motor over the conventional electromagnetic motor are:

1. Silent drive due to the ultrasonic frequency drive and no gear mechanism (i.e., more suitable for video cameras with microphones).
2. Thin motor design and no speed reduction mechanism such as gears, leading to space saving.
3. Energy saving.

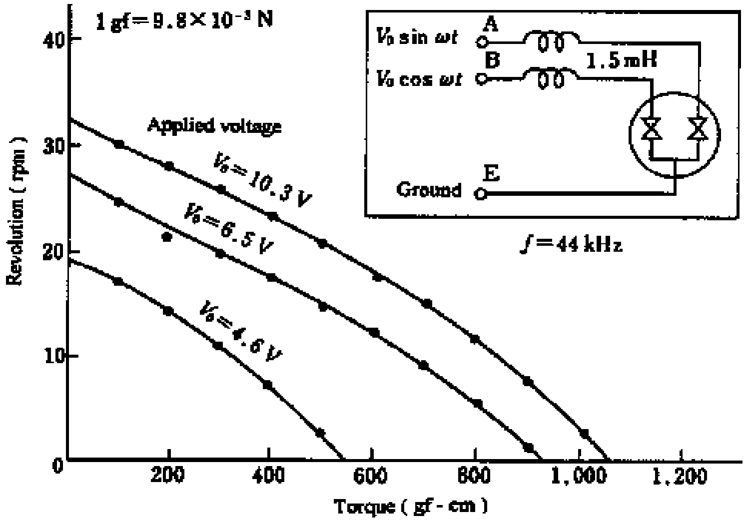

Fig. 42 Motor characteristics of Sashida's motor.

A general problem encountered for these traveling wave type motors is the support of the stator. In the case of a standing wave motor, the nodal points or lines are generally supported; this causes minimum effects on the resonance vibration. A traveling wave, however, does not have such steady nodal points or lines. Thus, special considerations are necessary. In Fig. 41, the stator is basically supported very gently along the axial direction on felt so as not to suppress the bending vibration. It is important to note that the stop pins which latch onto the stator teeth only provide high rigidity against the rotation.

Matsushita Electric proposed a nodal line support method using a higher order vibration mode.66) A stator wide ring is supported at the nodal circular line and "teeth" are arranged on the maximum amplitude circle to get larger revolution.

Seiko Instruments miniaturized the ultrasonic motor to dimensions as tiny as 10 mm in diameter using basically the same principle.67) Figure 43 shows the construction of one of these small motors with a 10 mm diameter and a 4.5 mm thickness. A driving voltage of 3 V and a current of 60 mA produces 6000 rev/min (no-load) with a torque of 0.1 mN·m. AlliedSignal developed ultrasonic motors similar to Shinsei's, which are utilized as mechanical switches for launching missiles.68)

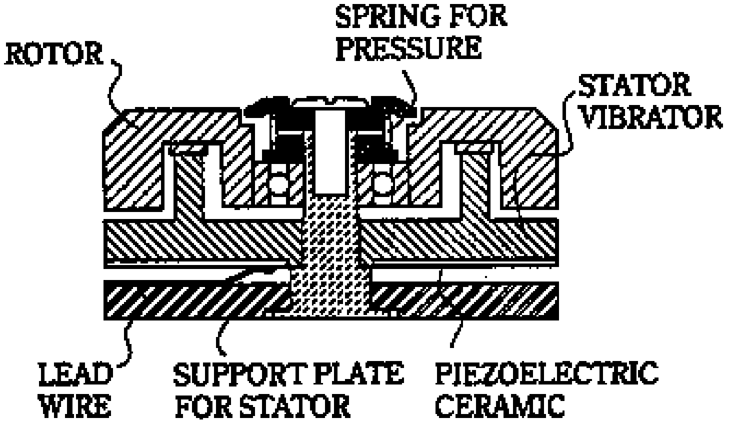

Fig. 43 Construction of Seiko's motor.

It is important to note that the unimorph (a piezoceramic plate and a metal plate bonded together) bending actuation cannot provide high efficiency theoretically, because the electromechanical coupling factor k is usually less than 10%. Therefore, instead of the unimorph structure, a simple disk was directly used to make motors.[69,70] The (1,1), (2,1) and (3,1) modes of a simple disk, which are axial-asymmetric modes, are proposed to use. Both the inner and outer circumferences can provide a rotation like a "hula hoop."

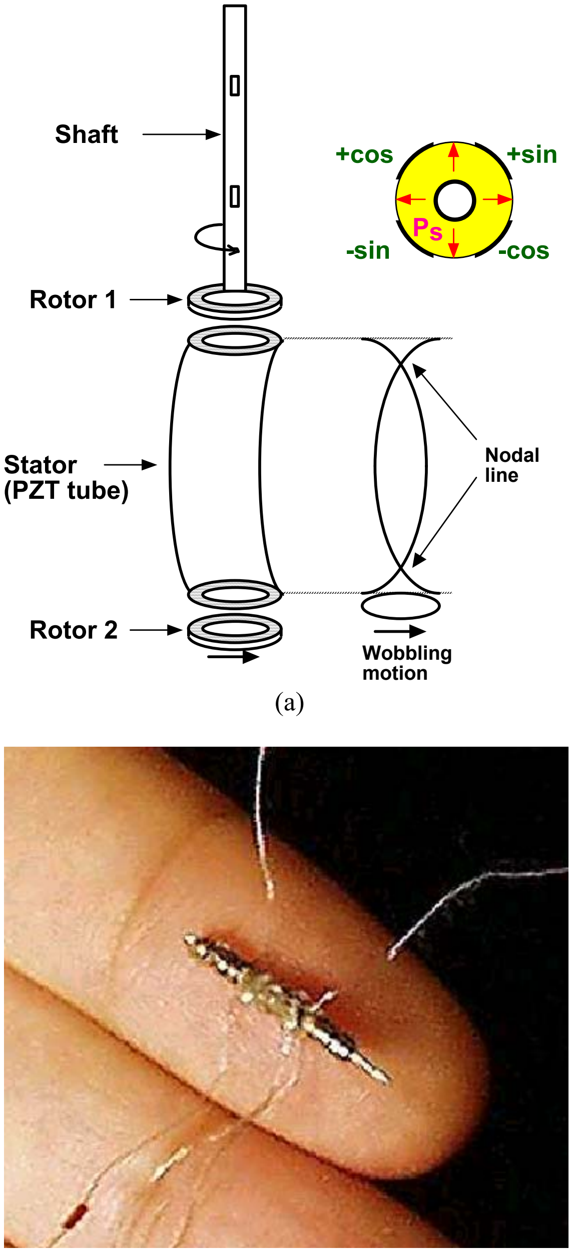

(a)

(b)

Fig. 44 "Plate-spinning" type motor by Penn State and IMRE (1.5 mm in diameter).

Another intriguing design is a "plate-spinning" type proposed by Tokin.71) Penn State and IMRE miniaturized the size down to 1.5 mm in diameter.72) Figure 44 shows its principle of operation and a photograph. A rotary bending vibration is excited on a PZT rod by a combination of sine and cosine voltages, then to rotors are brought into contact with the "spinning" rod at the end faces to produce the rotation.

In summary, the standing-wave type, in general, is low in cost (one vibration source) and has high efficiency (up to 98% theoretically), but lack of control in both the clockwise and counterclockwise directions is a problem. In comparison, the propagating-wave type combines two standing waves with a 90 degree phase difference both in time and space. This type requires, in general, two vibration sources to generate one propagating wave, leading to low efficiency (not more than 50%), but it is controllable in both rotational directions.

REFERENCES

1) B. Jaffe, W. Cook and H. Jaffe: *Piezoelectric Ceramics*, London: Academic Press (1971).
2) W. G. Cady: *Piezoelectricity*, New York: McGraw-Hill, Revised Edition by Dover Publications (1964).
3) M. E. Lines and A. M. Glass: *Principles and Applications of Ferroelectric Materials*, Oxford: Clarendon Press (1977).
4) K. Uchino: *Piezoelectric Actuators and Ultrasonic Motors*, Kluwer Academic Publishers, MA (1996).
5) K. Uchino: *Piezoelectric/Electrostrictive Actuators*, Morikita Publishing, Tokyo (1986).
6) T. Ikeda: *Fundamentals of Piezoelectric Materials Science*, Ohm Publishing Co., Tokyo (1984).
7) Y. Ito and K. Uchino: Piezoelectricity, *Wiley Encyclopedia of Electrical and Electronics Engineering*, Vol. **16**, p. 479, John Wiley & Sons, NY (1999).
8) W. A. Smith: *Proc. SPIE - The International Society for Optical Engineering* 1733 (1992).
9) H. Takeuchi, S. Jyomura, E. Yamamoto and Y. Ito: *J. Acoust. Soc. Am.*, **74**, 1114 (1982).
10) Y. Yamashita, K. Yokoyama, H. Honda and T. Takahashi: *Jpn. J. Appl. Phys.*, **20**, Suppl. 20-4, 183 (1981).
11) Y. Ito, H. Takeuchi, S. Jyomura, K. Nagatsuma and S. Ashida: *Appl. Phys. Lett.*, **35**, 595 (1979).
12) H. Takeuchi, H. Masuzawa, C. Nakaya and Y. Ito: *Proc. IEEE 1990 Ultrasonics Symposium*, 697 (1990).
13) J. Kuwata, K. Uchino and S. Nomura: *Jpn. J. Appl. Phys.*, **21**, 1298 (1982).
14) T. R. Shrout, Z. P. Chang, N. Kim and S. Markgraf: *Ferroelectric Letters*, **12**, 63 (1990).
15) R. E. Newnham, D. P. Skinner and L. E. Cross: *Materials Research Bulletin*, **13**, 525 (1978).
16) W. A. Smith: *Proc. 1989 IEEE Ultrasonic Symposium*, 755 (1989).
17) Kistler, Stress Sensor, Production Catalog, Switzerland.
18) Tokin, Gyroscope, Production Catalog, Japan.
19) K. Uchino, S. Nomura, L. E. Cross, S. J. Jang and R. E. Newham: Jpn. J. Appl. Phys. **20**, L367 (1981); K. Uchino: Proc. Study Committee on Barium Titanate, XXXI-171-1067 (1983).
20) B. A. Auld: *Acoustic Fields and Waves in Solids*, 2nd ed., Melbourne: Robert E. Krieger (1990).
21) G. S. Kino: *Acoustic Waves: Device Imaging and Analog Signal Processing*, Englewood Cliffs, N. J.: Prentice-Hall (1987).
22) C. S. Desilets, J. D. Fraser and G. S. Kino: *IEEE Trans. Sonics Ultrason.*, SU-25, 115 (1978).
23) C. Campbell: *Surface Acoustic Wave Devices and Their Signal Processing Applications*, San Diego, Calif. Academic Press (1989).
24) H. Matthews: *Surface Wave Filters*, New York: Wiley Interscience (1977).
25) C. A. Rosen: Proc. Electronic Component Symp., p.205 (1957).
26) S. Kawashima, O. Ohnishi, H. Hakamata, S. Tagami, A. Fukuoka, T. Inoue and S. Hirose: Proc. IEEE Int'l Ustrasonic Symp. '94, France (Nov., 1994).
27) K. Uchino: Bull. Am. Ceram. Soc., **65**(4), 647 (1986).
28) K.Uchino: MRS Bull., **18**(4), 42 (1993).
29) *Handbook on New Actuators for Precision Position Control* , Edit. in Chief K. Uchino., Fuji Technosystem, Tokyo (1994).
30) K. Uchino: "Recent Developments in Ceramic Actuators," Proc. Workshop on Microsystem Technologies in the USA and Canada, Germany, mst news, special issue, VDI/VDE, p.28-p.36 (1996).
31) K. Furuta and K. Uchino: Adv. Ceram. Mater., **1**, 61 (1986).

32) J. von Cieminski and H. Beige: J.Phys.D, **24**, 1182 (1991).
33) L. E. Cross, S. J.J ang, R. E. Newnham, S. Nomura and K. Uchino: Ferroelectrics, **23**(3), 187 (1980).
34) K. Uchino: Ceramic Data Book '88 (Chap.:Ceramic Actuators), Inst. Industrial Manufacturing Tech., Tokyo (1988).
35) K. Uchino and S. Nomura: Ferroelectrics, **50**(1), 191 (1983).
36) A. Furuta, K. Y. Oh and K. Uchino: Sensors and Mater., **3**(4), 205 (1992).
37) S. Takahashi, A. Ochi, M. Yonezawa, T. Yano, T. Hamatsuki and I. Fujui: Ferroelectrics, **50**, 181 (1993).
38) A. Bauer and F. Moller: Proc. 4th Int'l Conf. New Actuators, Germany, p.128 (1994).
39) Active Control Experts, Inc. Catalogue "PZT Quick Pack" (1996).
40) Y. Sugawara, K. Onitsuka, S. Yoshikawa, Q. C. Xu, R. E. Newnham and K. Uchino: J. Am. Ceram. Soc., **75**(4), 996 (1992).
41) H. Goto, K. Imanaka and K. Uchino: Ultrasonic Techno, **5**, 48 (1992).
42) N. Kanbe, M. Aoyagi, S. Hirose and Y. Tomikawa: J. Acoust. Soc. Jpn. (E), **14**(4), 235 (1993).
43) S. Sugiyama and K. Uchino: Proc. Int'l. Symp. Appl. Ferroelectrics '86, IEEE, p.637 (1986).
44) C. Kusakabe, Y. Tomikawa and T. Takano: IEEE Trans. UFFC, **37**(6), 551 (1990).
45) T. Ota, T. Uchikawa and T. Mizutani: Jpn. J. Appl. Phys., **24**, Suppl.24-3, 193 (1985).
46) J. T. Dorsey, T. R. Sutter and K. C. Wu: Proc. 3rd Int'l Conf. Adaptive Structures, p.352 (1992).
47) B. Wada: JPL Document D-10659, p.23 (1993).
48) F. K. Straub: Smart Mater. Struct., **5**, 1 (1996).
49) P. C. Chen and I. Chopra: Smart Mater. Struct., **5**, 35 (1996).
50) A. Ohgoshi and S. Nishigaki: Ceramic Data Book '81, p.35 Inst. Industrial Manufacturing Technology, Tokyo (1981).
51) T. Yano, E. Sato, I. Fukui and S. Hori: Proc. Int'l Symp. Soc. Information Display, p.180 (1989).
52) Y. Tanaka: Handbook on New Actuators for Precision Control, Fuji Technosystem, p.764 (1994).
53) Y. Yokoya: Electronic Ceramics, **22**, No. 111, p.55 (1991).
54) M. P. Koster: Proc. 4th Int'l Conf. New Actuators, Germany, p.144 (1994).
55) H. V. Barth: IBM Technical Disclosure Bull. **16**, 2263 (1973).
56) V. V. Lavrinenko, S. S. Vishnevski and I. K. Kartashev: Izvestiya Vysshikh Uchebnykh Zavedenii, Radioelektronica **13**, 57 (1976).
57) P. E. Vasiliev et al.: UK Patent Application GB 2020857 A (1979).
58) T. Sashida: Oyo Butsuri **51**, 713 (1982).
59) A. Kumada: Jpn. J. Appl. Phys., **24**, Suppl. 24-2, 739 (1985).
60) B. Koc, P. Bouchilloux and K. Uchino: IEEE Trans.-UFFC, **47**, 836 (2000).
61) Y. Fuda and T. Yoshida: Ferroelectrics, **160**, 323 (1994).
62) K. Nakamura, M. Kurosawa and S. Ueha: Proc. Jpn. Acoustic Soc., No.1-1-18, p.917 (Oct., 1993).
63) K. Uchino, K. Kato and M. Tohda: Ferroelectrics **87**, 331 (1988).
64) Y. Tomikawa, T. Nishituka, T. Ogasawara and T. Takano: Sonsors and Mater., **1**, 359 (1989).
65) T. Sashida: Mech. Automation of Jpn., **15** (2), 31 (1983).
66) K. Ise: J. Acoust. Soc. Jpn., **43**, 184 (1987).
67) M. Kasuga, T. Satoh, N. Tsukada, T. Yamazaki, F. Ogawa, M. Suzuki, I. Horikoshi and T. Itoh: J. Soc. Precision Eng., **57**, 63 (1991).
68) J. Cummings and D. Stutts: Amer. Ceram. Soc. Trans. "Design for Manufacturability of Ceramic Components," p.147 (1994).
69) A. Kumada: Ultrasonic Technology **1** (2), 51 (1989).
70) Y. Tomikawa and T. Takano: Nikkei Mechanical, Suppl., p.194 (1990).
71) T. Yoshida: Proc. 2nd Memorial Symp. Solid Actuators of Japan: Ultra-precise Positioning Techniques and Solid Actuators for Them, p.1 (1989).
72) S. Dong, K. Uchino, L. C. Lim: IEEE Trans.-UFFC, **50**, No.4 (2003) [in press].

High Power Piezoelectric Transformers
- Their Applications to Smart Actuator Systems –

Kenji Uchino
International Center for Actuators and Transducers
The Pennsylvania State University
kenjiuchino@psu.edu

Alfredo Vazquez Carazo
Face Electronics, LC
Norfolk, VA 23508
alfredo@faceco.com

Abstract: Piezoelectric transformers with power capability of < 10 W have successfully been commercialized for the backlight inverters of laptop computers. For further high power applications, our approaches in new piezoelectric materials, new designs and new connection technologies are introduced in this paper. PZT based piezoelectric ceramics with the maximum vibration velocity of 1.0 m/sec have been developed by rare-earth ion doping. Multi-stacked disk type transformers have significant advantages over the conventional Rosen type in terms of high power and isolation resistance. Also the connection technology helps to enhance the power capability. New applications of the piezoelectric transformers have been demonstrated in an integrated ultrasonic motor and a piezoelectric actuator drive system for active vibration control on helicopters.

HISTORY OF PIEZOELECTRIC TRANSFORMERS

One of the bulkiest components in information processing equipment (such as laptop computers) is the power supply, especially the electromagnetic transformer used in the power supply. Losses such as skin effect, thin wire and core losses of the electromagnetic transformer increase rapidly as the size is reduced. Therefore, it is difficult to realize miniature low profile electromagnetic transformers with high efficiency. On the contrary, high efficiency, small size, and absence of electromagnetic noise are some of the attractive features of piezoelectric transformers (PTs), making them more suitable for miniaturized power inverter components such as lighting up the cold cathode fluorescent lamp behind a color liquid crystal displays or generating high voltage for air-cleaners (T. Yoshida, 1997).

The original design to transform an input ac voltage to step up or step down using converse and direct piezoelectric properties of ceramic materials was proposed by Rosen (C.A. Rosen, 1956). The principle of this type of transformer is to excite a piezoelectric element (Fig. 1 top) at its mechanical resonance frequency. Applying an electrical input to one part of the piezoelectric element (left top electrode) generates a mechanical vibration and then this mechanical vibration is re-converted into electrical voltage from the other part (right edge electrode) of the piezoelectric plate. The voltage step-up ratio for unloaded condition (open circuited) is provided by

$$r \propto k_{31} k_{33} \, Q_m \, (L/t), \tag{1}$$

where L and t are the electrode gap distances for the input and output parts, respectively. Note that increasing in length/thickness ratio, electromechanical coupling factors and/or mechanical quality factor is the key to the step-up ratio increase. This transformer was utilized on trial in the color TVs in 1970's.

However, the initial Rosen type had a reliability problem; that is, easy mechanical breakdown at the center position due to the coincidence of the residual stress concentration (through the poling process) and the vibration nodal point (highest induced stress). Improvements over the years included the use of mechanically tough ceramic materials, of multilayer geometry that does not generate any poling direction mismatch [Philips Components, NEC (NEC, 1992)], and the redesign of the electrode configuration and exciting a 3rd longitudinal vibration mode of the rectangular plate (NEC) (S. Kawashima et. al, 1994). The piezo-transformers shown in Fig. 1 have been commercialized as a back-light inverter for the LCDs.

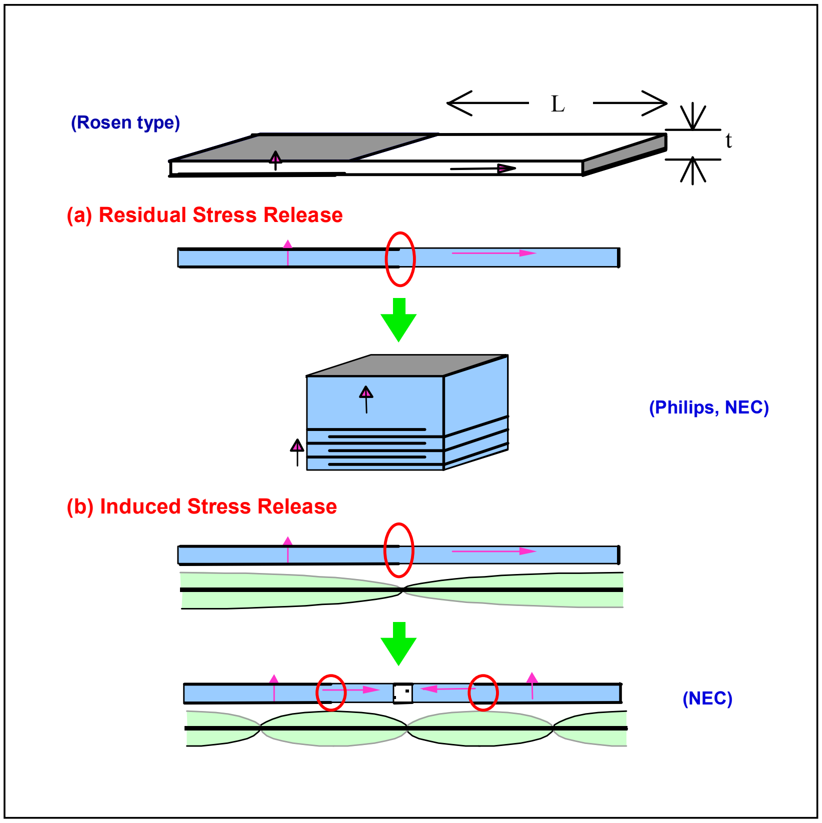

Figure 1. New piezoelectric transformer designs improved from the Rosen type. (a) multilayer type, and (b) 3rd mode type.

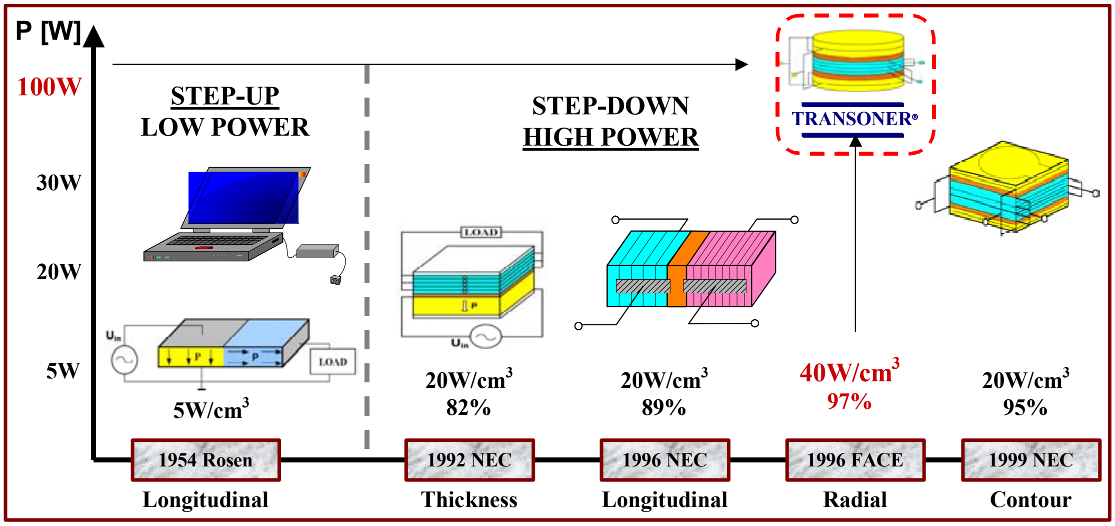

Figure 2. History of piezoelectric transformers in terms of power capability. Note that the multi-stacked disk type has a 100 W capability.

In order to improve the transformer performance, various proposals have been made: improvement in piezoceramics with higher mechanical toughness and low loss/high Q_m; selection of a vibration mode and an electrode configuration to separate the nodal point from the maximum residual stress point; selection of a vibration mode with higher electromechanical coupling. As shown in Fig. 2, though this device has been widely manufactured, the application is still limited due to the power capability < 10-20 W.

This paper reviews the recent development efforts on piezoelectric transformers from high power viewpoint, in particular: high power piezoelectrics, then our present design, multi-stacked disk type, and the connection technology of transformers. We also introduce our two new applications: an integrated ultrasonic motor and a piezoelectric actuator system driven by piezoelectric transformers.

HIGH POWER PIEZOELECTRICS

One of the serious problems which limit the power capability in present transformers is their heat generation. The conventional piezo-ceramics have the limitation in the maximum vibration velocity (v_{max}), since the additional input electrical energy is converted into heat, rather than into mechanical energy. The typical rms value of v_{max} for commercialized materials, defined by the temperature rise of 20^{o}C from room temperature, is around 0.3 m/sec for rectangular samples operating in the k_{31} mode (like a Rosen-type) (S. Hirose et. al, 1995). $Pb(Mn,Sb)O_3$ (PMS) - lead zirconate tatanate (PZT) ceramics with the v_{max} of 0.62 m/sec are currently used for NEC transformers (S. Takahashi et. al, 1995). By doping the PMS-PZT or $Pb(Mn,Nb)O_3$-PZT with rare-earth ions such as Yb, Eu and Ce, we recently developed the high power piezoelectrics, which can operate with v_{max} up to 1.0 m/sec

(J. Ryu et. al, 2003). Compared with commercially available piezoelectrics, 10 times higher input electrical energy and output mechanical energy can be expected from these new materials without generating significant temperature rise.

NEW TRANSFORMER DESIGNS

One of the drawbacks of piezo-transformers is a significant reduction of the step-up ratio (Eq. (1)) under an electrical load. This is mainly due to the impedance mismatch between the load and the output impedance of the transformer (i.e., capacitance C_{out}). For instance, a capacitive load C_L (= C_{out}) divides the step-up ratio r by two. Thus, several designs have been proposed in order to increase the step-up ratio.

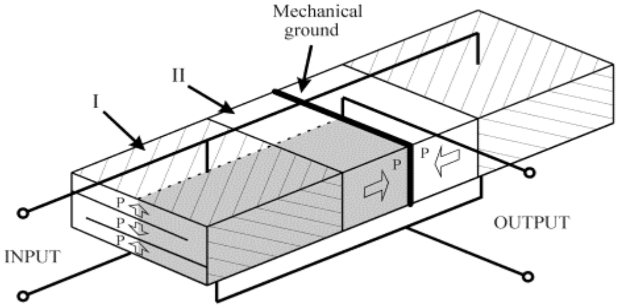

Figure 3. Multilayer type piezoelectric transformer (NEC).

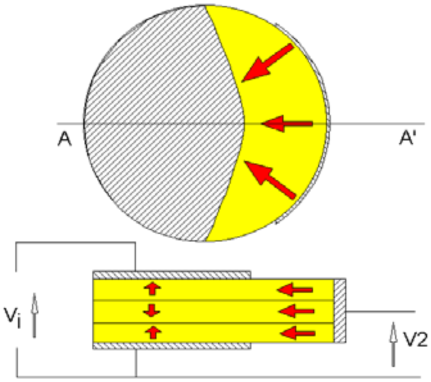

Figure 4. Disk shape piezoelectric transformer with curved electrodes (Penn State).

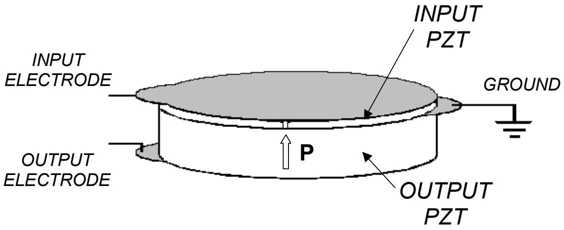

Figure 5. Stack type power transformer (Face International).

NEC developed a multilayer type transformer as shown in Fig. 3, where a higher voltage step up ratio was realized in proportion to the number of layers in the input part (S. Hirose et. al, 1995).

Disk type transformers (Fig. 4) have advantages over the Rosen type: usage of k_p and k_{15} (due to the curved electrode configuration) instead of k_{31} enhances the step-up ratio (more than 300 under zero load), and usage of curved electrodes reduces the stress concentration (B. Koc et. al, 2000). We demonstrated lighting up the 4W CCFL directly by 500V using a single disk sample (25 mm in diameter and 1 mm in thickness) without using an additional booster coil.

Face International developed a simple stacked piezo-transformer as shown in Fig. 5, which enhanced the power capability by several times over the Rosen-type transformers (R. P. Bishop, 1998). During the bonding process, the different thermal conductivity of the involved materials introduces a remained pre-stress in the transformer, which is the key to the enhancement of its power capabilities. Power rates higher than 80W with efficiencies around 95% have already been demonstrated.

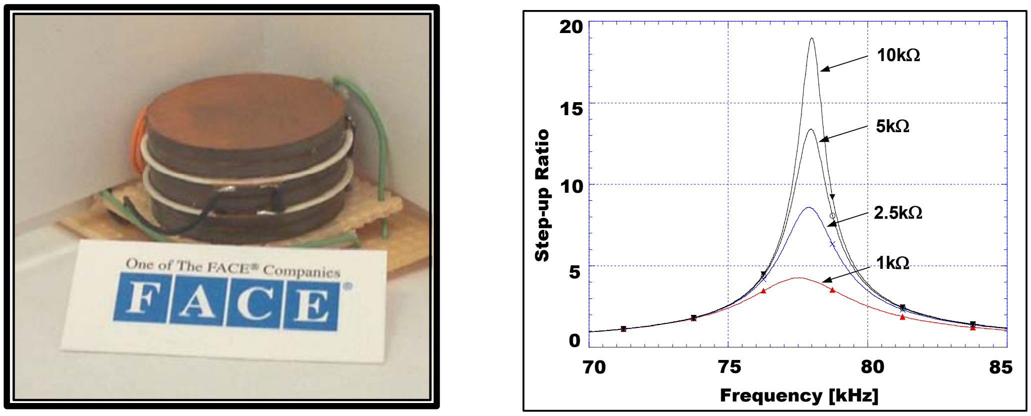

(a)

(b)

Figure 6. New multi-stacked disk type transformer for high power applications (a) and its transformer characteristics, step-up voltage ratio vs. load.

Taking into account the merits and demerits of the previous designs, for high power applications we adopted a multi-stacked disk type piezo-transformer with (or without) an insulation plate shown in Fig. 6(a), which is operated in the radial extensional mode. The merits include complete electric isolation (i.e., floating) owing to the sandwiched glass between the input and output piezo-plates, which is essential for connecting multiple transformers, and high energy density owing to a high operating frequency. Figure 6(b) shows its transformer characteristics, i.e., voltage step-up ratio versus frequency for various external load. Efficiency more than 96-98% is widely maintained.

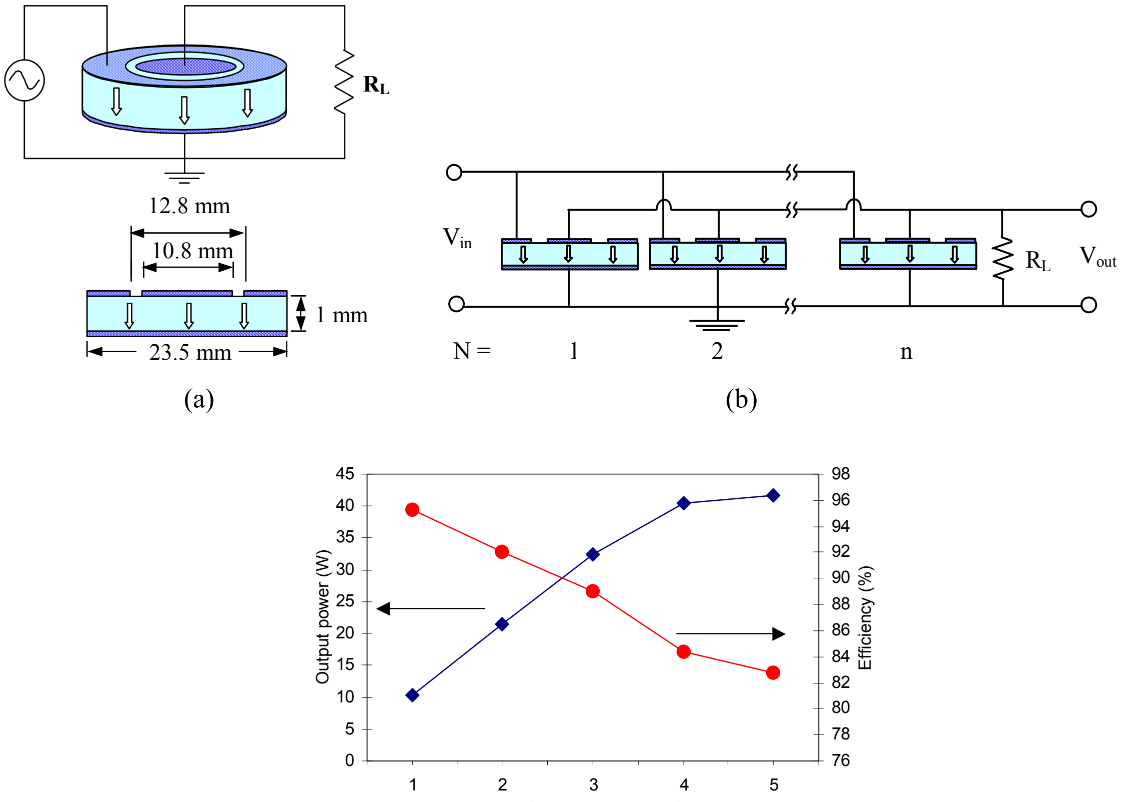

(a) (b)

(c)

Figure 7. (a) Ring-dot type piezoelectric transformer, (b) a parallel connection of piezoelectric transformers, and (c) output power and the efficiency as a function of number of transformers (V_{in} = 80 V_{rms}).

CONNECTION TECHNOLOGY

In order to seek inexpensive and mass-produced devices, our target is to sustain the transformer size less than 1" in diameter (just like a piezoelectric sounder). Consequently, because of the power limitation of each transformer, we need to consider a connection technique of multiple transformers in order to multiply the power capability.

In general, there are three combination algorithms of transformers; parallel, series, and cascade. For the parallel algorithm, the current capacity is increased by adding another path, leading to the power amplification. The series increase the capability of the voltage of both inputs and outputs, and also amplify the power. To the contrary, the cascade significantly enhances the step up or down voltage of the piezoelectric transformer. However, it does not increase much in transfer power. A parallel connection trial has been made previously using Rosen-type transformers (H.-S. Jeong et. al, 1999). However, due to the Rosen-type design with a high impedance-match load, the final power (4 W) was much below a practically required range.

Figure 7(b) shows a parallel connection of piezoelectric transformers. We utilized ring-dot type transformers (23.50 mm in diameter and 1.0 mm in thickness) operated in the fundamental radial extensional vibration mode (P. Laoratanakul et. al, 2002) (Fig. 7(a)). The input and output electrodes are concentrically placed on the top surface of the ceramic. Arrows indicate the thickness poling direction of the input and output sections. The input electrode is the external electrode ring and the output electrode is the internal center dot, which exhibits relatively low output impedance (about 500Ω). The bottom electrode, ground electrode, is common to both input and output sections and is extended to the fully bottom surface. Figure 7(c) shows the output power and the efficiency as a function of number of piezoelectric transformers when V_{in} is 80 V_{rms}. The load resistance was adjusted around a couple of 100Ω according to the transformer number, n, for maximizing the efficiency. The output power was 12 W for a single piezoelectric transformer and it was increased approximately proportional to n; when n is 2, 3 and 4, 22 W, 33 W, and 42 W, respectively. This configuration increases current capacity for the overall transformers. It is well usable and desired for higher power applications. However, a maximum efficiency is decreased with an increase in the number of piezoelectric transformers. 95% for a single transformer was reduced to 92%, 89%, 84% and 82%, with increasing the transformer number 2 to 5, respectively, at present.

APPLICATIONS

Basically, piezoelectric transformers are classified into two groups: resonance and off-resonance types. The off-resonance type is for step-down transformers used for precise measurements of high voltage such as 30 kV or high current on electric power transmission lines (A. Vazquez Carazo et. al, 1999). The resonance type is further divided into two groups: step-up types typically used as high-voltage inverters for the LCD back-light, and step-down types used as AC-DC converters (T. Zaitsu et. al, 1997). Figure 8 shows a prototype 35 W, 115 V_{AC} to 15 V_{DC} adapter for a laptop computer application, developed at our ICAT Center. Notice 1/4 smaller size and weight in comparison with the conventional electromagnetic type adapter.

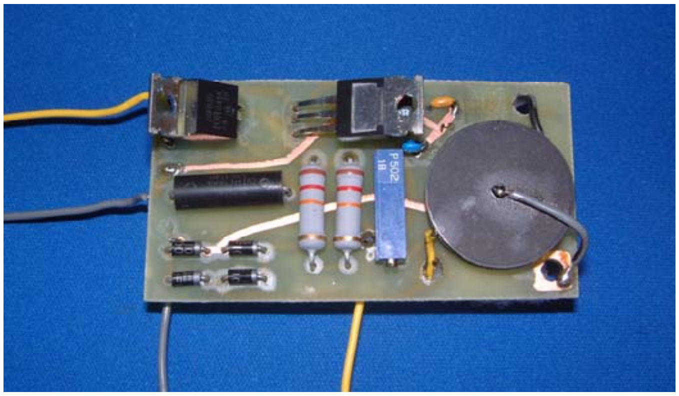

Figure 8. A prototype 35 W, 115 V_{AC} to 15 V_{DC} adapter for a laptop computer application.

We propose here a new application, that is, driving piezoelectric actuators. The basic concept is illustrated in Fig. 9. When we tune the transformer operating frequency exactly to the same frequency of an ultrasonic motor's resonance (for example, making a ring transformer, using the same size piezo-ring as the ultrasonic motor), we can use it as a drive system, or fabricate a transformer-integrated motor. When we couple a rectifier with the transformer, we can drive a multilayer or bimorph piezoelectric actuator.

Figure 10 shows a piezoelectric transformer (ring-shape) integrated ultrasonic motor (hula-hoop type). The voltage step-up ratio of 4 could provide a voltage of 40 V high enough for the motor drive, starting from a battery (H.-W. Kim et. al, 2002).

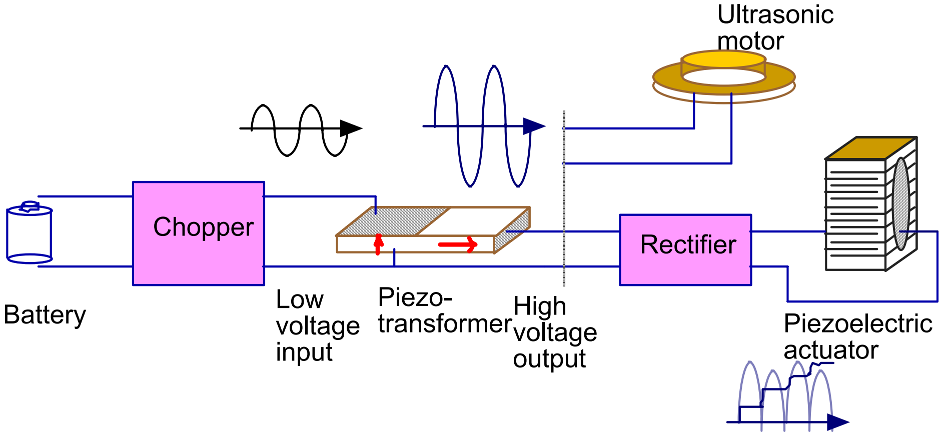

Figure 9. Basic concept of piezo-actuator drive systems (AC or pseudo DC) using a piezoelectric transformer.

Figure 10. Battery-operated ultrasonic motor (hula-hoop type) with a piezoelectric transformer (ring-shape) integrated in a drive circuit.

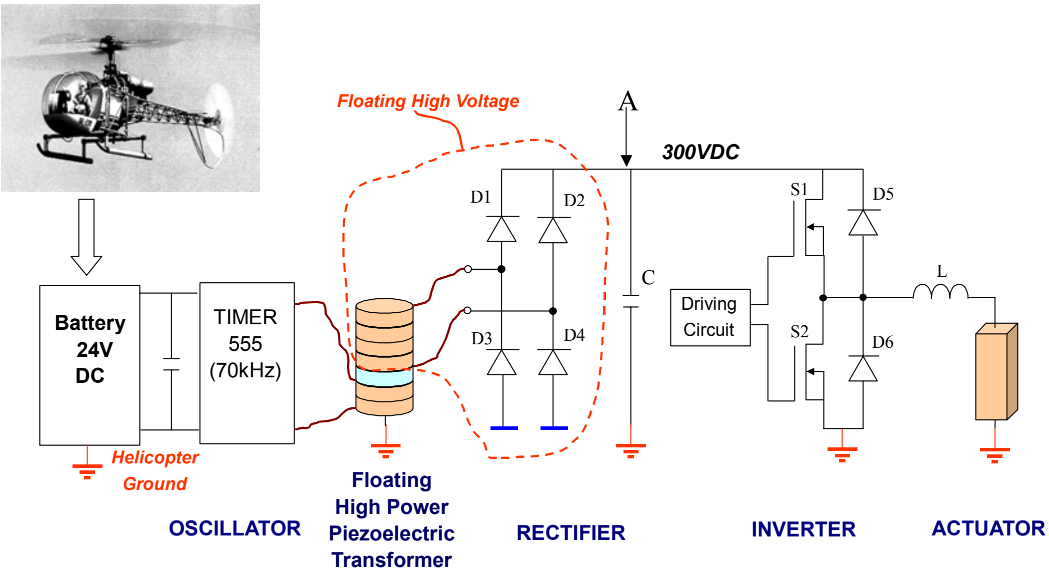

Figure 11. Compact drive system for piezoelectric actuator control.

We also demonstrated a compact drive system with a piezoelectric transformer for a multilayer piezoelectric actuator, aiming at active vibration control on a helicopter (A. Vazquez Carazo et. al, 2001). In this sort of military application, we need to realize a compact, light-weight and electromagnetic-noise-free system while keeping quick response (minimum 200Hz). For this sake, we have chosen a multilayer piezoelectric device as an actuator, and piezo-transformers (rather than electro-magnetic ones) as drive system components. Figure 11 summarizes our compact drive system for piezoelectric actuator control, using piezoelectric transformers.

We have targeted to develop two kinds of power supplies with piezo-transformers driven by a helicopter battery 24V$_{DC}$: one is a high voltage DC power supply (100-1000V, 90W) for driving the piezoelectric actuator, and the other is an AC adapter (±15V$_{DC}$, 0.1-0.5W) for driving the supporting circuitry. We utilized large and small multi-stacked piezo-transformer elements both with an insulator glass layer between the input and output parts for ensuring the complete floating condition, for the high power supply and the adapter, respectively. The used actuator was supplied from Tokin Corp., which has the size of 10x10x20mm^3, and is capable to generate a 16μm displacement under the maximum voltage of 100V.

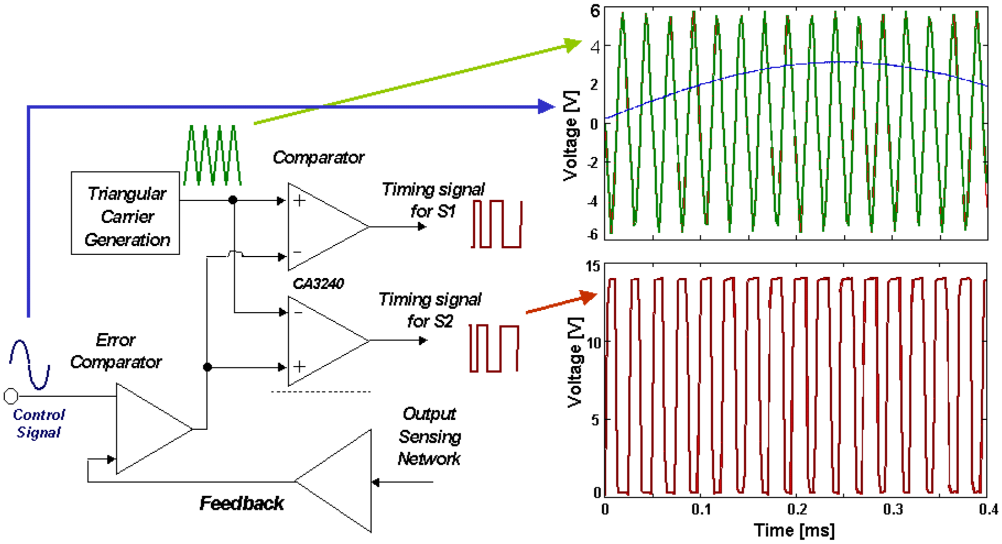

Figure 12. Pulse width modulation circuit for driving the power amplifier.

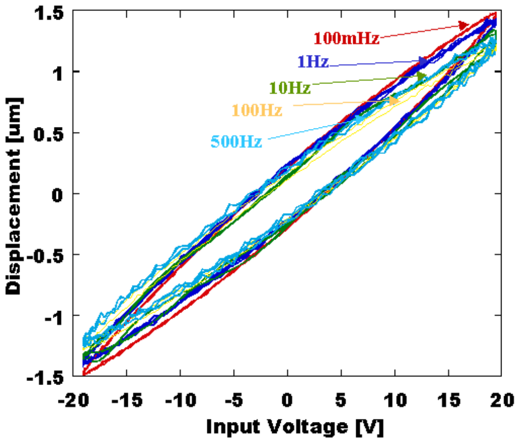

Figure 13. Displacement curves of the piezoelectric actuator driven by the newly developed power amplifier.

We initially tried to drive the actuator by applying the rectified high voltage directly after the power transformer (i.e., voltage at the point A in Fig. 11). However, because of a very slow response during a rising or falling voltage process(~1 sec), we decided to use this rectified voltage as a constant high DC voltage, and additionally use a power amplifier to control the voltage applied to the actuator. Among various power amplifier families (N. O. Sokal, 1997), we have chosen a Class-D switching amplifier (see Inverter in Fig. 10), because it has advantages over the other switching and linear amplifiers, such as permitting amplitude and frequency control and realizing fast actuation response of the actuator by chopping a DC voltage. The voltage level generated in the transformer was 300V for the input voltage of 75V applied through a timer 555 (Fig. 11).

The signal from a PWM (pulse width modulation) driving circuit (Fig. 12) was applied to two power MOSFET's of the half bridge. Thus, the constant $300V_{DC}$ voltage from the piezo-transformer was chopped, and control of frequency and magnitude was achieved. This output voltage was applied to the piezo-actuator through a filtering inductance of 100mH (Motorola, 1997). The PWM carrier frequency was chosen as 40kHz, which is below the mechanical resonance frequency of the used piezo-actuator (~60kHz). Figure 13 shows the displacement curves of the actuator driven by the newly developed power amplifier. The displacement was directly measured with an eddy current sensor. As seen in this figure, the displacement ±1.5μm was controlled by ±20V applied voltage. This drive system could be used at least up to 500Hz, which is sufficient for the active vibration control on a helicopter.

SUMMARY AND FUTURE

1. Piezoelectric transformers have the advantages over electromagnetic types in miniaturization, no electromagnetic noise generation, and high efficiency.
2. New high-power piezoceramics have been developed based on PZT-$Pb(Mn_{1/3}X_{2/3})O_3$ (X=Sb, Nb) doped with rare-earth. The maximum vibration velocity 1.0 m/s is three times that of the commercialized materials.
3. We developed a multi-stacked disk transformer using a radial mode with float mode capability which is suitable to voltage step-down applications such as driving circuit power supply.
4. Aiming at amplification of power, combination technologies of piezoelectric transformers have been demonstrated.
5. Using piezoelectric transformers, a drive system of a piezo-actuator has been developed, aiming at active vibration control on a helicopter. We manufactured a variable high voltage, DC - slow AC power supply for driving a piezoelectric multilayer actuator, and a constant low voltage DC power supply for the circuit drive. A piezo-transformer integrated ultrasonic motor has been also fabricated.

Part of this study was supported by Office of Naval Research, USA, Army Research Office, USA through QorTek Inc., and by NASA, USA through Face Electronics, LC.

REFERENCES

Bishop, R.P., 1998, Face International, Multilayer Piezoelectric Transformer," US Patent No. 5,834,882.

Hirose, S., S. Takahashi, K. Uchino, M. Aoyagi and Y. Tomikawa, 1995, "Measuring Methods for High-Power Characteristics of Piezoelectric Materials," Proc. Mater. for Smart Systems, Mater. Res. Soc. Vol. 360, pp.15-20.

Jeong, H.-S., B.-C Choi, J.-H. Yoo, I.-H. Im and C.-Y.Park, 1999, "Parallel Driving of Piezoelectric Transformers," *Jpn. J. Appl. Phys.* **38**, pp.5166-69.

Kawashima, S., O. Ohnishi, H. Hakamata, S. Tagami, A. Fukuoka, T. Inoue and S. Hirose, 1994, "Third order longitudinal mode piezoelectric ceramic transformer and its application to high-voltage power inverter," *IEEE Int'l Ultrasonic Symp. Proc.*, Nov.

Kim, H. W., S. Dong, P. Laoratanakul, K. Uchino and T. Park, 2002, "Novel Method for Driving the Ultrasonic Motor," *IEEE-UFFC Trans.*, Vol. 49, NO. 10, pp. 1356-1362.

Koc, B. and K. Uchino, 2000, "A Disk Type Piezoelectric Transformer with Crescent Shape Input Electrodes," *Proc. Piezoelectric Materials: Adv. in Sci. Tech. and Appl.*, pp.375-382.

Laoratanakul, P., A. Vazquez Carazo, P. Bouchilloux and K. Uchino, 2002, "Unipoled Disk-Type Piezoelectric Transformers," *Jpn. J. Appl. Phys.* **41**, pp. 146-50.

Motorola, 1997, "Actuator Drive and Energy Recovery System," US Patent No. 5,691,592.

NEC, 1992, "Thickness Mode Piezoelectric Transformer," US Patent No. 5,118,982.

Rosen, C.A., 1956, "Ceramic Transformers and Filters," *Proc. Electronic Component Symp.*, pp. 205-211.

Ryu, J., Kim, H.W., Uchino, K. and Lee, J., 2003, "Effect of Yb Addition on the Sintering Behavior and High Power Piezoelectric Properties of $Pb(Zr,Ti)O_3$-$Pb(Mn,Nb)O_3$, Jpn. J. Appl. Phys. Vol. 42, No. 3, pp. 1-4.

Sokal, N.O., 1997, "RF Power Amplifier, Classes A through S," Proc. Electron. Ind. Forum of New England, pp. 179-252.

Takahashi, S., Y. Sasaki, S. Hirose and K. Uchino, 1995, "Electromechanical Properties of $PbZrO_3$-$PbTiO_3$-$Pb(Mn_{1/3} Sb_{2/3})O_3$ Ceramics under Vibration-Level Change," *Mat. Res. Soc. Symp. Proc.* Vol. 360, pp.305-310.

Vázquez Carazo, A. and R. Bosch, 1999, "Piezoelectric Non-Resonant Transformer to Measure High Voltage," *J. European Ceram. Soc.* **19**, pp. 1275-79.

Vazquez Carazo, A. and K. Uchino, 2001, "Novel Piezoelectric-Based Power Supply for Driving Piezoelectric Actuators Designed for Active Vibration Damping Applications," *J. Electroceramics* Vol. 7, pp. 197-210.

Yoshida, T., 1997, "Technology Trend of Piezoelectric Devices," *Tokin Technical Review*, **24**, pp.1-9.

Zaitsu, T., Y. Fuda, Y. Okabe, T. Ninomiya, S. Hamamura, and M. Katsuno, 1997, "New Piezoelectric Transformer Converter for AC-Adapter," *Proc. IEEE APEC'97*, Vol.**2**, pp.568-572, Feb.

Micro Piezoelectric Ultrasonic Motors

K. Uchino, S. Cagatay, *International Center for Actuators and Transducers, Mater. Res. Inst., The Penn State University, University Park, PA, USA*; B. Koc*, Mechatronics Eng. Dept., Atilim University, Ankara, Turkey*; S. Dong, *Materials Sci. and Eng., Virginia Polytech Institute, Blacksburg, VA, USA*; P. Bouchilloux, *Adaptronics, Troy, NY, USA*; M. Strauss, *HME, Newburyport, MA, USA*

Abstract

This paper reviews recent developments of micro ultrasonic rotary motors using piezoelectric resonant vibrations. Following the historical background, four ultrasonic motors recently developed at Penn State University are introduced; *windmill*, *PZT tube*, *metal tube*, and *shear-type* motors. Driving principles and motor characteristics are described in comparison with the conventional ultrasonic motors. Motors with 1.5 mm in diameter and 0.8 mN·m in torque have been actually developed.

Keywords: Ultrasonic motor, Piezoelectric actuator, Standing wave motor

INTRODUCTION

The market research conducted in the middle '90 for 80 international electronic component companies provided a very intriguing demand for motors in these 10 years; that is, 5 – 8 mm size motors with reasonable efficiency, human-compatible force and inexpensive price. Regarding conventional electromagnetic motors, tiny motors smaller than 1 cm are rather difficult to be produced in principle with sufficient energy efficiency. Note that a wrist watch motor with a rotor diameter less than 1 mm ϕ still requires a relatively large (10 mm) coil for its activation, despite of its low efficiency less than 1%. MEMS devices based on Silicon electrostatic actuation are too small in size with very small force, and do not endure against the component shaking/shock test. Ultrasonic motors whose efficiency is insensitive to size are considered superior in the mini-motor area. Following the historical background, four ultrasonic motors recently developed at Penn State University are introduced in this review paper; *windmill*, *PZT tube*, *metal tube*, and *shear-type* motors. Motors with 1.5 mm in diameter and 0.8 mN·m in torque have been actually developed. Some applications using these motors are introduced lastly.

CLASSIFICATION OF ULTRASONIC MOTORS

Historical Background

Electromagnetic motors were invented more than a hundred years ago. While these motors still dominate the industry, a drastic improvement cannot be expected except through new discoveries in magnetic or superconducting materials. Regarding conventional electromagnetic motors, tiny motors smaller than 1cm long are theoretically difficult to produce with sufficient energy efficiency. Therefore, a new class of motors using high power ultrasonic energy, i.e., *ultrasonic motor*, is gaining wide spread attention. Ultrasonic motors made with piezoceramics whose efficiency is insensitive to size are superior in the mini-motor area. For example, a commercialized electromagnetic motor by Motorola with 7 mm in diameter and 16 mm in length can generate 0.075 mN·m in torque and 5000 rpm in no-load speed under an input power of 0.2 W, which is more than one order of magnitude higher than the power required for our ultrasonic motors with similar specifications.

Figure 1 shows the basic construction of an ultrasonic motor, which consists of a high-frequency power supply, a vibrator and a slider. Further, the vibrator is composed of a piezoelectric driving component and an elastic vibratory part, and the slider is composed of an elastic moving part and a friction coat.

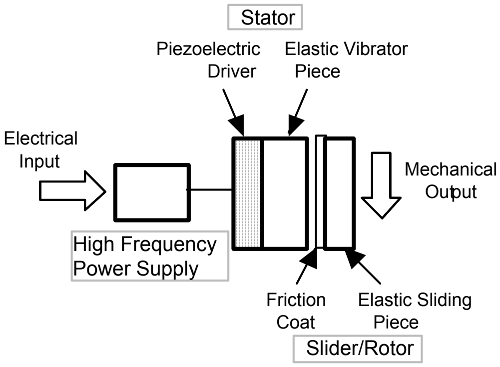

Fig. 1 Fundamental construction of an ultrasonic motor.

Though there had been some earlier attempts, the practical ultrasonic motor was proposed firstly by H. V. Barth of IBM in 1973 [1]. A rotor was pressed against two horns placed at different locations. By exciting one of the horns, the rotor was driven in one direction, and by exciting the other horn, the rotation direction was reversed. Various mechanisms based on virtually the same principle were proposed by V. V. Lavrinenko [2] and P. E. Vasiliev [3] in the former USSR. Because of difficulty in maintaining a constant vibration amplitude with temperature rise, wear and tear, the motors were not of much practical use at that time.

In 1980's, with an increase of chip pattern density, the semi-conductor industry began to request much more precise and sophisticated positioners which do not generate magnetic field noise. This urgent request has accelerated the developments in ultrasonic motors. Another advantage of ultrasonic motors over the conventional electromagnetic motors with expensive copper coils, is the improved availability of piezoelectric ceramics at reasonable cost.

The merits and demerits of the ultrasonic motors are [4]:

Merits

1. Low speed and high torque -- Direct drive
2. Quick response, wide velocity range, hard brake and no backlash
   -- Excellent controllability
   -- Fine position resolution
3. High power / weight ratio and high efficiency
4. Quiet drive
5. Compact size and light weight
6. Simple structure and easy production process
7. Negligible effect from external magnetic or radioactive fields, and also no generation of these fields

Demerits

8. Necessity for a high frequency power supply
9. Less durability due to frictional drive
10. Drooping torque vs. speed characteristics

Classification and Principles of Ultrasonic Motors

Two categories are being investigated for ultrasonic motors from a vibration characteristic viewpoint: a standing-wave type and traveling-wave type [4]. The standing wave is expressed by

$$u_S(x,t) = A \cos kx \cdot \cos \omega t, \qquad (1)$$

while the traveling wave is expressed as

$$u_P(x,t) = A \cos (kx - \omega t). \qquad (2)$$

Using a trigonometric relation, Eq. (2) can be transformed as

$$u_p(x,t) = A \cos kx \cdot \cos \omega t + A \cos (kx - \pi/2) \cdot \cos (\omega t - \pi/2). \qquad (3)$$

This leads to an important result, i.e., a traveling wave can be generated by superimposing two standing waves whose phases differ by 90 degree to each other both in time and in space. This principle is necessary to generate a traveling wave on a limited volume/size substance, because only standing waves can be excited stably in a finite size.

The standing-wave type is sometimes referred to as a vibratory-coupler type or a "woodpecker" type, where a vibratory piece is connected to a piezoelectric driver and the tip portion generates flat-elliptical movement. The standing-wave type has, in general, high efficiency, but lack of control in both clockwise and counterclockwise directions is a problem. By comparison, the traveling-wave type (a surface-wave or "surfing" type) combines two standing waves with a 90^o phase difference both in time and in space. A surface particle of the elastic body draws an elliptical locus due to the coupling of longitudinal and transverse waves. This type requires, in general, two vibration sources to generate one traveling wave, leading to low efficiency (not more than 50 %), but it is controllable in both the rotational directions just by exchanging sine and cosine supplied voltages. Due to the necessity of the dual drive system, the traveling wave type is more complicated in structure and expensive in manufacturing cost than the standing wave type.

Conventional Motor Designs

Figure 2 shows the famous Sashida motor [5]. By means of the traveling elastic wave induced by a thin piezoelectric ring, a ring-type slider in contact with the "rippled" surface of the elastic body bonded onto the piezoelectric is driven in both directions by exchanging the sine and cosine voltage inputs. The PZT piezoelectric ring is divided into 16 positively and negatively poled regions and two asymmetric electrode gap regions so as to generate a 9th mode propagating wave at 44 kHz. A prototype was composed of a brass ring of 60 mm in outer diameter, 45 mm in inner diameter and 2.5 mm in thickness, bonded onto a PZT ceramic ring of 0.5 mm in thickness with divided electrodes on the back-side. The rotor was made of polymer coated with hard rubber or polyurethane.

Canon utilized the "surfing" motor for a camera automatic focusing mechanism, installing this ring-type motor compactly in the lens frame. Using basically the same principle, Seiko Instruments miniaturized the ultrasonic motor to a diameter as small as 10 mm [6]. A driving voltage of 3 V provides torque of 0.1 mN·m. Seiko installed this tiny motor into a wrist watch as a silent alarm. AlliedSignal developed ultrasonic motors similar to Shinsei's, which would be utilized as mechanical switches for launching missiles [7].

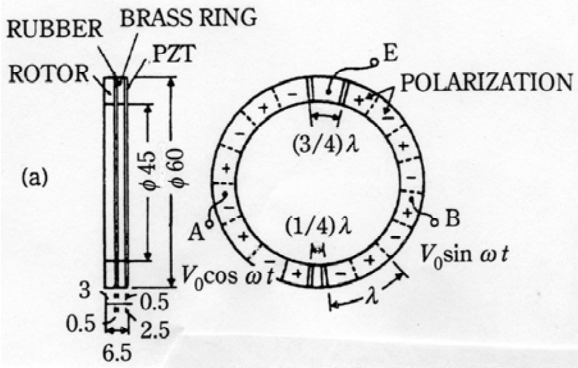

Fig. 2 Stator structure of Sashida's motor.

A significant problem in miniaturizing this sort of traveling wave motor can be found in the ceramic manufacturing process; without providing a sufficient buffer gap between the adjacent electrodes, the electrical poling process (upward and downward) easily initiates the crack on the electrode gap due to the residual stress concentration. This may restrict the further miniaturization of the traveling wave type motors. To the contrary, standing wave type motors, the structure of which is less complicated, are more suitable for miniaturization as we will discuss in the following. They require only one uniformly poled piezo-element, less electric lead wires and one power supply.

Another problem encountered in these traveling wave type motors is the support of the stator. In the case of a standing wave motor, the nodal points or lines are generally supported; this causes minimum effects on the resonance vibration. To the contrary, a traveling wave does not have such steady nodal points or lines. Thus, special considerations are necessary. In Fig. 2, the stator is basically fixed very gently along the axial direction through felt so as not to suppress the bending vibration.

We point out here also that one of the key factors for the actual commercialization of ultrasonic motors is to develop low loss and high mechanical quality factor piezoelectric materials, in order to suppress the heat generation during driving, which limits the continuous operation. We developed new ceramic series based on PZT-Pb(Mn,X)O_3 (X=Sb, Nb) systems, which can be used for 10 times higher input/output power range than the commercially available *Hard* PZT's without generating significant heat. Refer to some recent papers [8,9] on this issue.

COMPACT MOTOR DESIGNS

We adopted the following concepts for developing new compact ultrasonic motors: (a) simplify the structure and reduce the number of component, (b) use simple (i.e., uniform) poling configuration; that is, "*Gentle to Ceramic*" and (c) use the standing-wave type to reduce the drive circuit components.

Windmill Motor

We have developed a *Windmill* motor design with basically a flat and wide configuration, using a metal-ceramic composite structure [10,11]. The motor is composed of four components: stator, rotor, ball-bearing and housing unit [Fig. 3(a)]. The piezoelectric part has a simple structure of a ring electroded on its top and bottom surfaces (ϕ 3.0mm) poled uniformly in the thickness direction. The metal ring machined by Electric Discharge Machining has four inward arms placed 90^o apart on its inner circumference. The metal and piezoelectric rings are bonded together, but the arms remain free; they thus behave like cantilever beams [Fig. 3(b)]. The length and cross-sectional area of each arm were selected such that the resonance frequency of the second bending mode of the arms is close to the resonance frequency of the radial mode of the stator. The rotor is placed at the center of the stator and rotates when an electric field is applied at a frequency between the radial and bending resonance modes. The truncated cone shape at the rotor end guarantees a permanent contact with the tips of the arms.

The operating principle of this motor is as follows: in the contraction cycle of the stator, the four arms at the center of the metal ring clamp the rotor and push it in the tangential direction. Since the radial mode frequency of the stator is close to the second bending mode frequency of the arms, the respective deformations are added and the tips of the arms bend down. In the expansion cycle, the arms release the rotor from a different path such that their tips describe an elliptical trajectory on the surface of the rotor. This motion seems to be a human finger's grasping-and-rotating action.

Figure 4 shows the size dependence of the motor characteristics. When driven at 160 kHz, the maximum revolution 2000 rpm and the maximum torque 0.8 mNm were obtained for a 5 mm ϕ motor. Figure 5 shows motor characteristics in a 3 mm ϕ motor plotted as a function of load torque. A starting torque of 17 μNm is one order of magnitude higher than that of a thin film motor with a similar size [12].

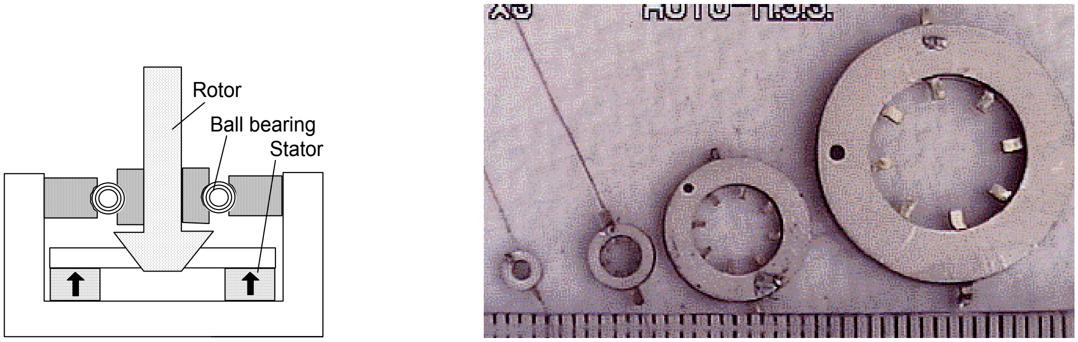

(a) (b)

Fig. 3 "Windmill" motor using a metal coupler with multiple inward arms. (a) Cross sectional view, and (b) photos of various size stators (3-20 mm ϕ).

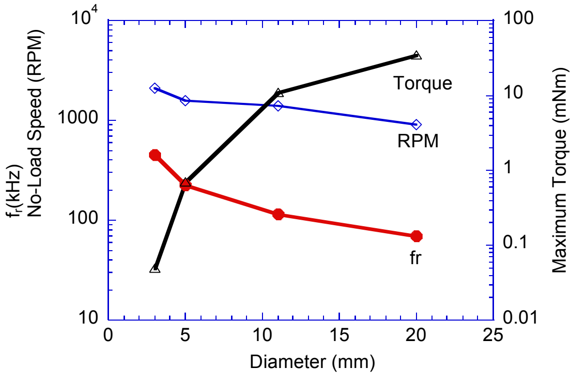

Fig. 4 Radial mode resonance frequency, no-load speed and starting torque vs. diameter of the stator, measured at 15.7 V.

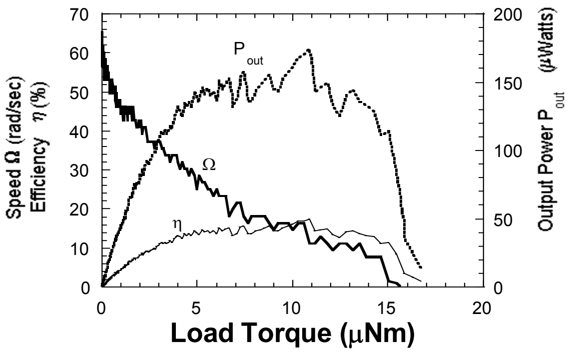

Fig. 5 Speed, efficiency, and output power versus load torque for a 3 mm ϕ motor.

PZT Tube Motor

In collaboration with Institute of Materials Research and Engineering, Singapore, we developed a PZT tube motor with a slim and long configuration [13]. The principle is similar to the one proposed by Tokin [14], which is schematically illustrated in Fig. 6. Four segmented electrodes were made on a PZT tube (1.5 mm or 2.2 mm in outer diameter) uniformly poled along the radial direction. A rotary bending vibration mode was excited on the PZT cylinder by combining sine and cosine voltages to the segmented electrodes, then two rotors were made to contact the wobbling tube ends for achieving rotation. The motion is analogous to a "dish-spinning" performance.

Our motor with 1.5/2.2 mm in diameter, 7 mm in length and 0.3 g in weight could generate 0.1 mN·m in torque and 1000-2000 rpm in no-load speed. Table I summarized the specification comparison with other commercialized motors. Our motors sustain the efficiency more than 20% in this size, which is one order of magnitude higher than the electromagnetic motors. Compared with Seiko motors, the PZT tube type exceeds more than 10 times in the power density (output mechanical energy/unit volume).

Although the motor characteristic is satisfactory for various applications such as intra-vascular medical micro surgery, there is one big problem, that is, difficulty in manufacturing fine and accurate PZT tubes, which leads to the expensive manufacturing cost.

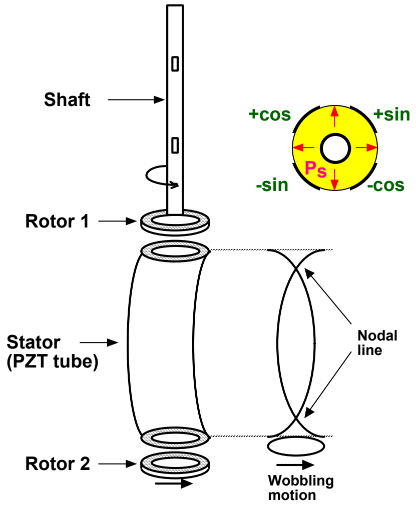

Fig. 6 Structure of a PZT tube type motor.

Table I Comparison of the motor specifications from Motorola, Seiko Instruments, and ICAT/Penn State.

	Motorola Electromagnetic Micromotor	Seiko Ultrasonic Micromotor		ICAT/PSU Ultrasonic Micromotor
Outer diameter (mm)	7	8		2.2
Length (mm)	16	4.5		8
Power source (V)	1.5	1.5*	3.5*	3 - 6*
(mA)	126	60	12	2 – 5
No-load speed (rpm)	5000	1200	1200	1000-2000
Starting torque (mN m)	0.075	0.05	0.1	0.1

* A booster circuit is required.

Metal Tube Motor

In order to lower the manufacturing cost with keeping the motor performance, we have developed a metal tube type, as shown in Fig. 7(a) [15]. Instead of the PZT tube, we utilized a metal hollow cylinder, bonded with two PZT rectangular plates uniformly poled. Both can be easily found/prepared and cheap in price. When we drive one of the PZT plates, Plate X, a bending vibration is excited basically along x axis. However, because of an asymmetrical mass (Plate Y), another hybridized bending mode is excited with some phase lag along y axis, leading to an elliptical locus in a clockwise direction. On the other hand, when Plate Y is driven, counter-clockwise wobble motion is excited. Also note that only a single-phase power supply is required.

The rotor of this motor is a cylindrical rod with a pair of stainless ferrule pressed with a spring. The assembly is shown in Fig. 7(b). The power-related characteristics of a metal cylinder motor 2.4 mm in diameter and 12 mm in length with no load applied are plotted as a function of torque in Figure 8. The motor was driven at 62.1 kHz in both rotation directions. A no-load speed of 1800 rpm and an output torque up to 1.8 mN·m were obtained for rotation in both directions under an applied rms voltage of 80 V. The very high level of torque produced by this motor is due to the dual stator configuration and the high contact force between the metal stator and rotors. The rather high maximum efficiency of about 28% for this relatively small motor is a noteworthy feature of the data presented in Fig. 8. One of the world's smallest ultrasonic motors to date is pictured in Fig. 9 [16]. It is 1.5 mm in diameter and 4 mm in length. The rotor is a thin hollow tube, through which an optical fiber can pass.

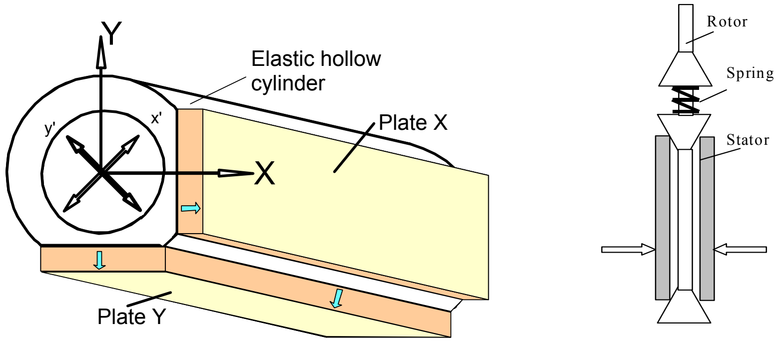

(a) (b)

Fig. 7 (a) Structure of a metal tube stator, and (b) assembly of the motor.

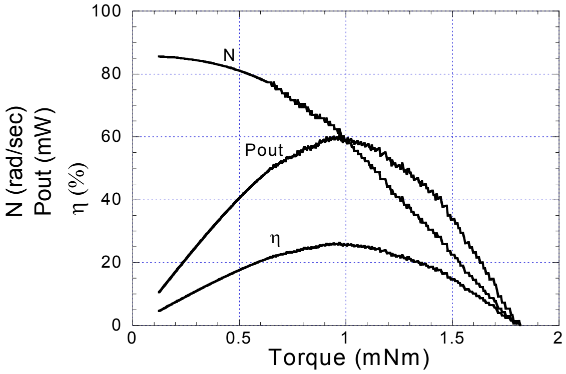

Fig. 8 The power-related characteristics of a metal cylinder rotary motor plotted as a function of torque. [Diameter: 2.4 mm, Length: 12 mm, Operating Frequency: 62.1 kHz, Load: none]

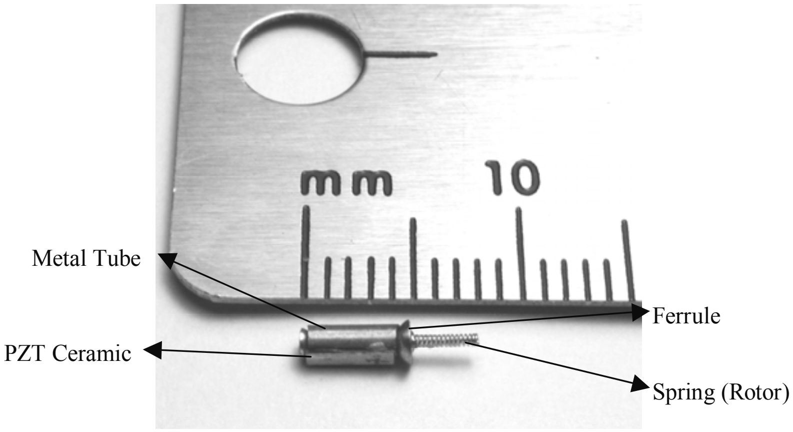

Fig. 9 One of the world's smallest ultrasonic motors to date. [Diameter: 1.8 mm, Length: 4 mm]

Shear-Type Motor

The above three motors were designed primarily aiming at discrete motor components, basically with using k_{31} mode. We describe here a new compact ultrasonic motor operated using the k_{15} shear-mode, of which the energy conversion rate from electrical to mechanical is much higher than the k_{31} type. Also this new design is compatible with the Silicon MEMS technology in the new future. Figure 10 shows a sketch of the new motor. The piezoelectric stator of this motor is constituted of a PZT ceramic disc with a center hole and a teeth type metal ring bounded to the disc. The piezoelectric disc was poled along its radial direction, the bottom electrode of which was divided into four parts with keeping the top electrode common. When a pair of voltage signals, sine and cosine, at the first shear-bending mode resonance frequency of the disc were input to the two pairs of electrodes, a traveling wave was generated circumferentially. Note that the shear mode excited in a finite size (diameter/thickness ratio <<15) disk is inevitably associated with a bending mode. A ring with teeth was used to amplify the vibration level of the traveling wave, which drove a rotor in contact via mechanical friction. A prototype motor, whose stator was 10.5 mm in diameter and 2.2mm in thickness with its first shear-bending mode resonance frequency at 38.9 kHz, exhibited the maximum no-load rotational speed of 200rpm under 70 $V_{rms}/8mA_{rms}$ applied.

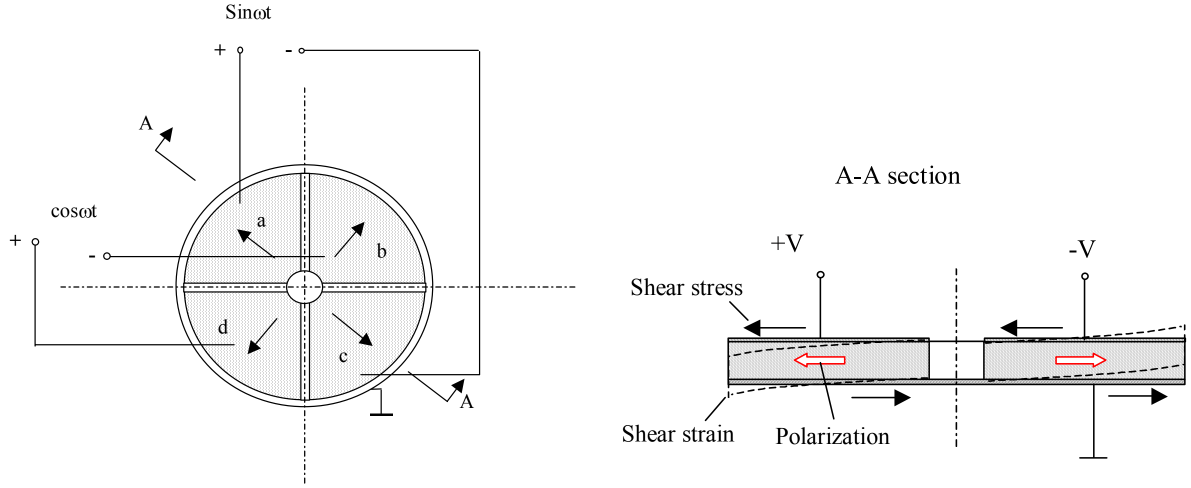

(a) Shear motor stator element. (b) Operation principle of flexure vibration using the shear-mode.

Fig. 10 Piezoelectric element for a shear-mode motor.

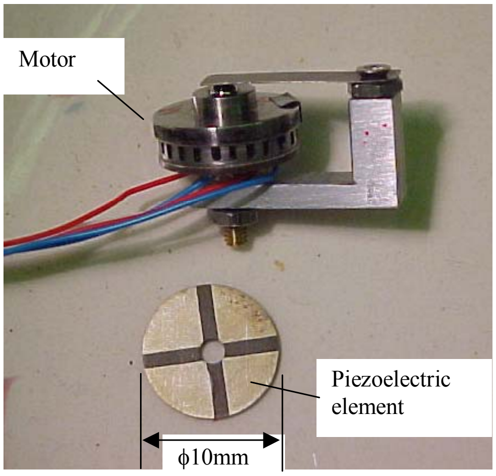

Fig. 11 Photo of the shear-mode motor.

APPLICATIONS OF MICRO MOTORS

The ICAT at Penn State is conducting various micro motor projects at present, which are divided into three categories; (1)medical diagnostic and surgery devices, (2) office and IT equipment including laptop computers, printers, scanners and cell phones, and (3) micro machines. Figure 12 depicts examples for the medical catheter application, and Fig. 13 is a photo of the world smallest 4WD vehicle with using a pair of the 4 mm long metal tube motors. Though the drive circuit and batteries have not been integrated at present, this tiny vehicle can be operated on a human finger by a joy-stick (Notice the finger print in the picture.)

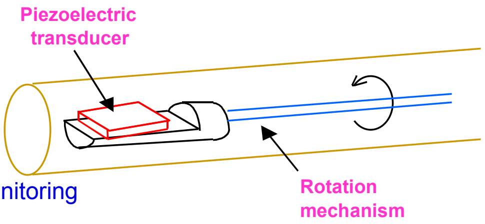

(a) Sideview Monitoring

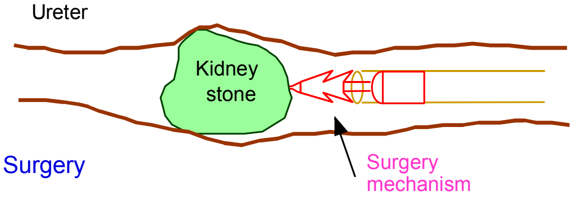

(b) Micro Surgery

Fig. 12 Application examples of micro ultrasonic motors for the medical catheter application

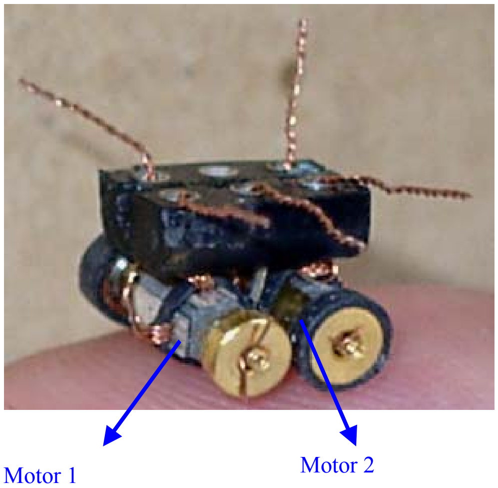

Fig. 13 World-smallest 4WD vehicle with using a pair of the 4 mm long metal tube motors. (Notice the finger print in the picture.)

SUMMARY

Ultrasonic motors are characterized by "low speed and high torque." Thus, the ultrasonic motors do not require gear mechanisms, leading to very quiet operation and space saving. Moreover, high power/weight ratio, high efficiency, compact size and light weight are very promising for the future micro actuators adopted to catheter or tele-surgery.

We introduced here three compact motors recently developed; flat type *Windmill*, thin & long *PZT tube* and its cheaper version, *metal tube*, and finally *shear* motor. For the further applications of the ultrasonic motors, systematic investigations on the following issues will be required: (1) low loss & high vibration velocity piezoceramics, (2) piezo-actuator component designs with high fracture resistance, (3) ultrasonic motor designs (standing-wave type, frictional contact), and (4) inexpensive and efficient high frequency/high power supplies.

Acknowledgement

This work was partially supported by the Office of Naval Research through Contract No. N00014-96-1-1173.

References

1) H. V. Barth: IBM Technical Disclosure Bull. **16**, 2263 (1973).
2) V. V. Lavrinenko, S. S. Vishnevski and I. K. Kartashev: Izvestiya Vysshikh Uchebnykh Zavedenii, Radioelektronica **13**, 57 (1976).
3) P. E. Vasiliev et al.: UK Patent Application GB 2020857 A (1979).
4) K. Uchino: "*Piezoelectric Actuators and Ultrasonic Motors*," Kluwer Academic Publishers, MA (1996).
5) T. Sashida: Mech. Automation of Jpn., **15** (2), 31 (1983).
6) M. Kasuga, T. Satoh, N. Tsukada, T. Yamazaki, F. Ogawa, M. Suzuki, I. Horikoshi and T. Itoh: J. Soc. Precision Eng., **57**, 63 (1991).
7) J. Cummings and D. Stutts: Amer. Ceram. Soc. Trans. "Design for Manufacturability of Ceramic Components", p.147 (1994).
8) S. Takahashi, Y. Sasaki, S. Hirose and K. Uchino: Proc. MRS '94 Fall Mtg. Vol.**360**, p.2-5 (1995).
9) K. Uchino, J. Zheng, A. Joshi, Y. H. Chen, S. Yoshikawa, S. Hirose, S. Takahashi, and J. W. D. de Vries: J. Electroceramics, **2**, 33 (1998).
10) B. Koc, A. Dogan, Y. Xu, R. E. Newnham and K. Uchino: Jpn. J. Appl. Phys. 37, 5659 (1998).
11) B. Koc, P. Bouchilloux, and K. Uchino: IEEE Trans.-UFFC, **47**, 836 (2000).
12) G. A. Racine, P. Muralt and M.A. Dudois: Smart Mater. Struct., **7**, 404 (1998)
13) S. Dong, S. P. Lim, K. H. Lee, J. Zhang, L. C. Lim and K. Uchino: IEEE Trans.-UFFC **50**(4), 361 (2003).
14) T. Yoshida: Proc. 2nd Memorial Symp. Solid Actuators of Japan: Ultra-Precise Positioning Techniques, p.1 (1989).
15) B. Koc, J. F. Tressler and K. Uchino: Proc. 7th Actuator 2000, p.242-245, Axon, Bremen (2000).
16) S. Cagatay, B. Koc and K. Uchino: IEEE Trans.-UFFC **50** (5) (2003). [in press]

Loss Mechanisms And High Power Piezoelectrics

K. Uchino, J. H. Zheng, Y. H. Chen, X. H. Du, J. Ryu, Y. Gao, *International Center for Actuators and Transducers, Penn State University, University Park, PA, USA*; S. Hirose, *Faculty of Eng., Yamagata University, Yonezawa, Japan*

Abstract

Heat generation is one of the significant problems in piezoelectrics for high power density applications. In this paper, we review the loss mechanisms in piezoelectrics first, followed by the heat generation processes for various drive conditions. Heat generation at off-resonance is caused mainly by dielectric loss tan δ' (i.e., P-E hysteresis loss), not by mechanical loss, while the heat generation at resonance is mainly attributed to mechanical loss tan ϕ'. Then, practical high power materials developed at Penn State is introduced, which exhibit the vibration velocity more than 1 m/s, leading to the power density capability 10 times of the commercially available "hard" PZTs. Finally, we propose a internal bias field model to explain the low loss and high power origin of these materials.

INTODUCTION

Loss or hysteresis in piezoelectrics exhibits both merits and demerits. For positioning actuator applications, hysteresis in the field-induced strain provides a serious problem, and for resonance actuation such as ultrasonic motors, loss generates significant heat in the piezoelectric materials. Further, in consideration of the resonant strain amplified in proportion to a mechanical quality factor, low (extrinsic) mechanical loss materials are preferred for ultrasonic motors. To the contrary, for force sensors and acoustic transducers, a low mechanical quality factor Q_m (which corresponds to high mechanical loss) is essential to widen a frequency range for receiving signals.

K. H. Haerdtl wrote a review article on electrical and mechanical losses in ferroelectric ceramics [1]. Losses are considered to consist of four portions: (1) domain wall motion, (2) fundamental lattice portion, which should also occur in domain-free monocrystals, (3) microstructure portion, which occurs typically in polycrystalline samples, and (4) conductivity portion in highly-ohmic samples. However, in the typical piezoelectric ceramic case, the loss due to the domain wall motion exceeds the other three contributions significantly. They reported interesting experimental results on the relationship between electrical and mechanical losses in piezoceramics, $Pb_{0.9}La_{0.1}(Zr_{0.5}Ti_{0.5})_{1-x}Me_xO_3$, where Me represents the doped ions Mn, Fe or Al and x varied between 0 and 0.09. However, they measured the mechanical losses on poled ceramic samples, while the electrical losses on unpoled samples, i.e., in a different polarization state, which lead big ambiguity in the discussion.

As far as the authors' knowledge, not much research effort has been put into systematic studies of the loss mechanisms in piezoelectrics, particularly in high electric field and high power density ranges. Although T. Ikeda described part of the formulas of this paper in his textbook [2], he totally neglected the piezoelectric losses, which have been found not to be neglected in our investigtions. In this paper, we review the loss mechanisms in piezoelectrics first, followed by the heat generation processes for various drive conditions. Then, practical high power materials developed at Penn State is introduced, exhibiting the power density capability 10 times of the commercially available "hard" PZTs. Finally, we propose a model to explain the low loss and high power origin of these materials.

GENERAL CONSIDERATION OF LOSS AND HYSTERESIS IN PIEZOELECTRICS

Theoretical Formulas

Since we have described the detailed mathematics in the previous paper [3], we just summarize the results in this section. We start from the following two piezoelectric equations:

$$x = s^E X + d E, \tag{1}$$
$$D = d X + \varepsilon^X \varepsilon_0 E. \tag{2}$$

Here, x is strain, X, stress, D, electric displacement, E, electric field. Equations (1) and (2) are the expression in terms of intensive (i.e., externally controllable) physical parameters X and E. Temperature dependence is carried into the elastic compliance s^E, the dielectric constant ε^X and the piezoelectric constant d. Note that the piezo-electric equations cannot yield a delay-time related loss, without taking into account irreversible thermodynamic equations or dissipation functions, in general. However, the latter considerations are mathematically equivalent to the introduction of complex physical constants into the phenomenological equations, if the loss can be treated as a perturbation.

Therefore, we will introduce complex parameters ε^{X*}, s^{E*} and d^* in order to consider the hysteresis losses in dielectric, elastic and piezoelectric coupling energy :

$$\varepsilon^{X*} = \varepsilon^X(1 - j \tan \delta'), \tag{3}$$
$$s^{E*} = s^E(1 - j \tan \phi'), \tag{4}$$
$$d^* = d(1 - j \tan \theta'). \tag{5}$$

θ' is the phase delay of the strain under an applied electric field, or the phase delay of the electric displacement under an applied stress. Both delay phases should be exactly the same if we introduce the same complex piezoelectric constant d^* into Eqs.(1) and (2). δ' is the phase delay of the electric displacement to an applied electric field under a constant stress (e.g., zero stress) condition, and ϕ' is the phase delay of the strain to an applied stress under a constant electric field (e.g., short-circuit) condition. We will consider these phase delays as "intensive" losses.

Figures 1(a) - 1(d) correspond to the model hysteresis curves for practical experiments: D vs. E curve under a stress-free condition, x vs. X under a short-circuit condition, x vs. E under a stress-free condition and D vs. X under a short-circuit condition for measuring current, respectively. Notice that these measurements are easily conducted in practice.

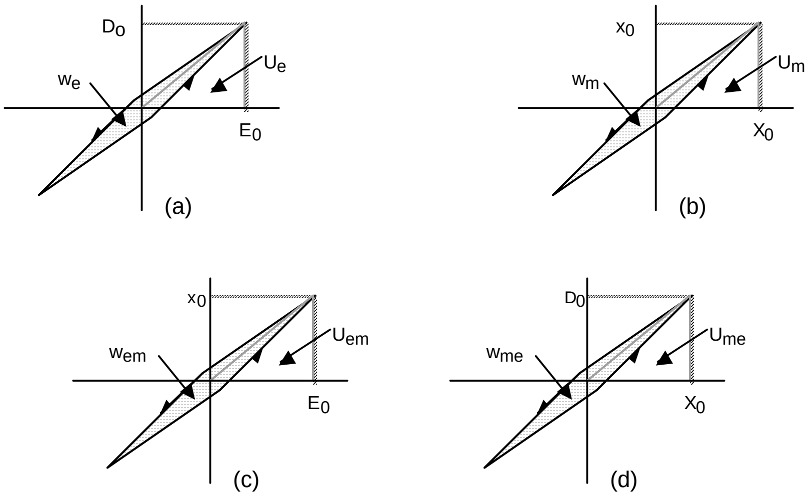

Fig.1 (a) D vs. E (stress free), (b) x vs. X (short-circuit), (c) x vs. E (stress free) and (d) D vs. X (short-circuit) curves with a slight hysteresis in each relation.

The stored energies and hysteresis losses for pure dielectric and elastic energies can be calculated as:

$$U_e = (1/2)\, \varepsilon^X \varepsilon_0 E_0^2, \tag{6}$$
$$w_e = \pi\, \varepsilon^X \varepsilon_0 E_0^2 \tan \delta', \tag{7}$$

$$U_m = (1/2)\, s^E X_0^2, \quad (8)$$

$$w_m = \pi\, s^E X_0^2 \tan\phi' . \quad (9)$$

The electromechanical hysteresis losses are more complicated, which can be calculated as follows, depending on the measuring ways; when measuring the induced strain under an electric field,

$$U_{em} = (1/2)\, (d^2 / s^E)\, E_0^2, \quad (10)$$

and

$$w_{em} = \pi\, (d^2 / s^E)\, E_0^2\, (2 \tan\theta' - \tan\phi'). \quad (11)$$

Note that the strain vs. electric field measurement should provide the combination of piezoelectric loss tanθ' and elastic loss tanϕ'. When we measure the induced charge under stress, the stored energy U_{me} and the hysteresis loss w_{me} during a quarter and a full stress cycle, respectively, are obtained as

$$U_{me} = (1/2)\, (d^2 / \varepsilon_0 \varepsilon^X)\, X_0^2, \quad (12)$$

$$w_{me} = \pi\, (d^2 / \varepsilon_0 \varepsilon^X)\, X_0^2\, (2 \tan\theta' - \tan\delta'). \quad (13)$$

Hence, from the measurements of *D* vs. *E* and *x* vs. *X*, we obtain tanδ' and tanϕ', respectively, and either the piezoelectric (*D* vs. *X*) or converse piezoelectric measurement (*x* vs. *E*) provides tan θ' through a numerical subtraction.

So far, we discussed the "intensive" dielectric, mechanical and piezoelectric losses. In order to consider real physical meanings of the losses, we will introduce the "extensive" losses [3]. When we start from the piezoelectric equations in terms of extensive physical parameters *x* and *D*:

$$X = c^D x - h D, \quad (14)$$

$$E = - h x + \kappa^x \kappa_0 D, \quad (15)$$

we introduce the extensive dielectric, elastic and piezoelectric losses as

$$\kappa^{x*} = \kappa^x (1 + j \tan\delta), \quad (16)$$

$$c^{D*} = c^D (1 + j \tan\phi), \quad (17)$$

$$h^* = h (1 + j \tan\theta). \quad (18)$$

It is notable that the permittivity under a constant strain (e.g., zero strain or completely clamped) condition, ε^{x*} and the elastic compliance under a constant electric displacement (e.g., open-circuit) condition, s^{D*} can be provided as an inverse value of κ^{x*} and c^{D*}, respectively. Thus, using the exactly the same losses in Eqs. (16) and (17),

$$\varepsilon^{x*} = \varepsilon^x (1 - j \tan\delta), \quad (19)$$

$$s^{D*} = s^D (1 - j \tan\phi), \quad (20)$$

We will consider these phase delays again as "extensive" losses.

Here, we consider the physical property difference between the boundary conditions; *E* constant and *D* constant, or *X* constant and *x* constant. When an electric field is applied on a piezoelectric sample as illustrated in the top of Fig. 2, this state will be equivalent to the superposition of the following two steps: first, the sample is completely clamped and the field E_0 is applied (pure electrical energy $(1/2)\, \varepsilon^x \varepsilon_0 E_0^2$ is input); second, keeping the field at E_0, the mechanical constraint is released (additional mechanical energy $(1/2)\, (d^2/s^E)\, E_0^2$ is necessary). The total energy should correspond to the total input electrical energy $(1/2)\, \varepsilon^X \varepsilon_0 E_0^2$. Similar energy calculation can be obtained from the bottom of Fig. 2, leading to the following equations:

$$\varepsilon^x / \varepsilon^X = (1 - k^2), \quad (21)$$

$$s^D / s^E = (1 - k^2), \quad (22)$$

$$\kappa^X / \kappa^x = (1 - k^2), \quad (23)$$

$$c^E / c^D = (1 - k^2), \quad (24)$$

where

$$k^2 = d^2/(s^E \varepsilon_0 \varepsilon^X) = h^2/(c^D \kappa^x \kappa_0). \qquad (25)$$

This k is called the *electromechanical coupling factor*, which is defined as a real number in this manuscript.

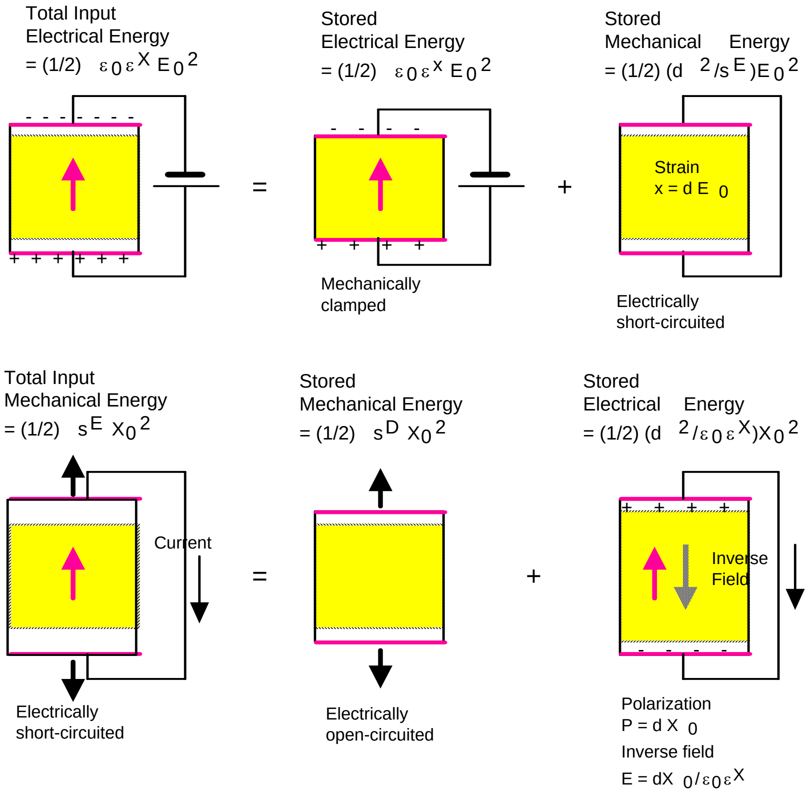

Fig. 2 Conceptual figure for explaining the relation between ε^X and ε^x, s^E and s^D.

In order to obtain the relationships between the intensive and extensive losses, the following three equations are essential:

$$\varepsilon_0 \varepsilon^X = [\kappa^x \kappa_0 (1 - h^2/(c^D \kappa^x \kappa_0))]^{-1}, \qquad (26)$$

$$s^E = [c^D (1 - h^2/(c^D \kappa^x \kappa_0))]^{-1}, \qquad (27)$$

$$d = [h^2/(c^D \kappa^x \kappa_0)] [h (1 - h^2/(c^D \kappa^x \kappa_0))]^{-1}. \qquad (28)$$

Replacing the parameters in Eqs. (26) - (27) by the complex parameters in Eqs. (3) - (5), (16) - (18), we obtain the relationships between the extrinsic and intrinsic losses:

$$\tan \delta' = (1/(1 - k^2))[\tan \delta + k^2 (\tan \phi - 2 \tan \theta)], \qquad (29)$$

$$\tan \phi' = (1/(1 - k^2))[\tan \phi + k^2 (\tan \delta - 2 \tan \theta)], \qquad (30)$$

$$\tan \theta' = (1/(1 - k^2))[\tan \delta + \tan \phi + (1 + k^2) \tan \theta], \qquad (31)$$

where k is the electromechanical coupling factor defined by Eq. (25), and here as a real number. It is important that the extrinsic dielectric and elastic losses are mutually correlated with the intrinsic dielectric, elastic and piezoelectric losses through the electromechanical coupling k^2, and that the denominator $(1 - k^2)$ comes basically from the ratios, $\varepsilon^x/\varepsilon^X = (1 - k^2)$ and $s^D/s^E = (1 - k^2)$, and this real part reflects to the dissipation factor when the imaginary part is divided by the real part. Also note that depending on the vibration mode, the definition of electromechanical coupling k can be changed such as $k^2 = d^2/(s^D \varepsilon_0 \varepsilon^X)$.

Experimental Example

We determined "intensive" dissipation factors first from (a) D vs. E (stress free), (b) x vs. X (short-circuit), (c) x vs. E (stress free) and (d) D vs. X (short-circuit) curves for a soft PZT based multilayer actuator [4]. Then, we calculated the "extensive" losses as shown in Fig. 3. Note that the piezoelectric losses tanθ' and tanθ are not so small as previously believed, but comparable to the dielectric and elastic losses, and increase gradually with the field or stress. Also it is noteworthy that the extensive dielectric loss tanδ increases significantly with an increase of the intensive parameter, i.e., the applied electric field, while the extensive elastic loss tanϕ is rather insensitive to the intensive parameter, i.e., the applied compressive stress. When similar measurements to Figs. 1(a) and 1(b), but under constrained conditions; that is, D vs. E under a completely clamped state, and x vs. X under an open-circuit state, respectively, we can expect smaller hystereses; that is, extensive losses, tanδ and tanϕ. These measurements seem to be alternative methods to determine the three losses separately, however, they are rather difficult in practice.

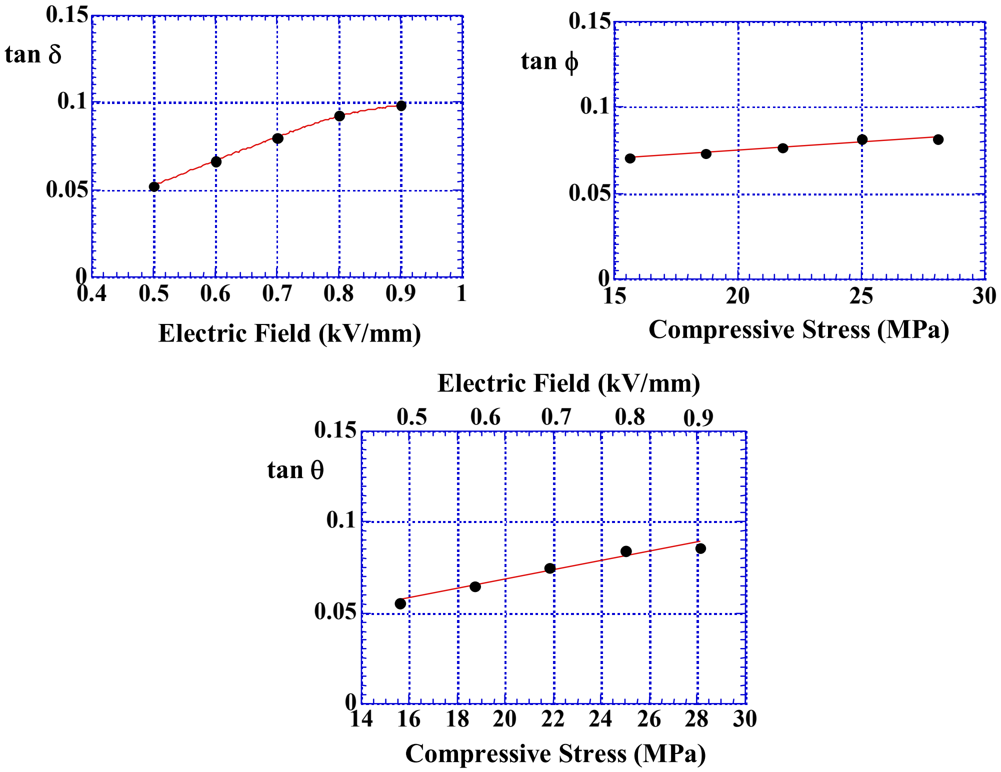

Fig. 3 Intrinsic loss factors, tanδ, tanϕ and tanθ as a function of electric field or compressive stress, measured for a PZT based actuator.

Physical Meaning of Extensive Losses

For making the situation simplest, we consider here only the domain wall motion-related losses. Taking into account the fact that the polarization change is primarily attributed to 180 degree domain wall motion, while the strain is attributed to 90 degree (or non-180°) domain wall motion, we suppose that the extensive dielectric and mechanical losses are originated from 180° and 90° domain wall motions, respectively, as illustrated in Fig. 4. The dielectric loss comes from the hysteresis during the 180° polarization reversal under E, while the elastic loss comes from the hysteresis during the 90° polarization reorientation under X. In this model, the intensive (observable) piezoelectric loss is explained by the 90° polarization reorientation under E, which can be realized by superimposing the 90° polarization reorientation under X and the 180° polarization reversal under E. This is the primarily reason why Eq. (11) includes a combination term as (2 tanθ' - tanϕ').

If we adopt the Uchida-Ikeda polarization reversal/reorientation model [5], we can explain the loss change with intensive parameter (externally controllable parameter). By finding the polarization P and the field-induced strain x as a function of the electric field E, it is possible to estimate the volume in which a 180° reversal or a 90° rotation occurred. This is because the 180° domain reversal does not contribute to the induced strain, only the 90° rotation does, whereas the 180° domain reversal contributes mainly to the polarization. The volume change of the domains with external electric field is shown schematically in Fig. 5 that with the application of an electric field the 180° reversal occurs rapidly whereas the 90° rotation occurs slowly. It is notable that at G in the figure, there remains some polarization while the induced strain is zero, at H the polarizations from the 180° and 90° reorientations cancel each other and become zero, but the strain is not at its minimum. Due to a sudden change in 180° reversal above a certain electric field, we can expect a sudden increase in the polarization hysteresis and in the loss [Fig. 3 top left]; while the slope of 90° reorientation is almost constant, we can expect a constant loss or a mechanical quality factor Q_m with changing the external parameter, *E* or *X* [Fig. 3 top right]. This situation will be discuss again in the later section.

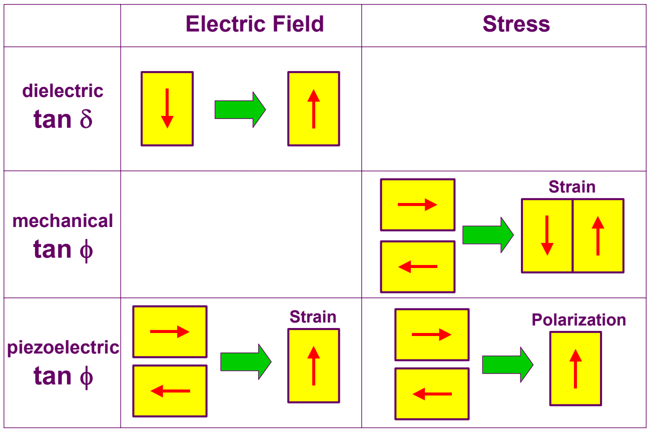

Fig. 4 Polarization reversal/reorientation model for explaining dielectric, elastic and piezoelectric losses.

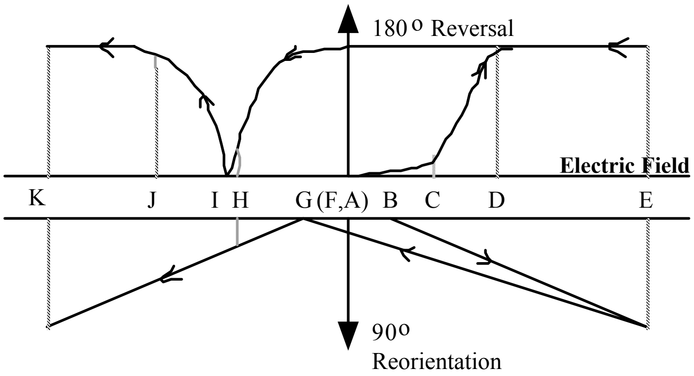

Fig. 5 Polarization reversal/reorientation model for explaining the loss change with electric field.

LOSSES AT A PIEZOELECTRIC RESONANCE

So far, we have considered the losses for a quasi-static or off-resonance state. Problems in ultrasonic motors which are driven at the resonance frequency include significant distortion of the admittance frequency spectrum due to nonlinear behavior of elastic compliance at a high vibration amplitude, and heat generation which causes a serious degradation of the motor characteristics through depoling of the piezoceramic. Therefore, the ultrasonic motor requires a very hard type piezoelectric with a high mechanical quality factor Q_m, leading to the suppression of heat generation. It is also notable that the actual mechanical vibration amplitude at the resonance frequency is directly proportional to this Q_m value.

Vibration at A Piezoelectric Resonance

Let us review the longitudinal mechanical vibration of a piezo-ceramic plate through the transverse piezoelectric effect (d_{31}) as shown in Fig. 6 [6]. Assuming that the polarization is in the z-direction and the x-y planes are the planes of the electrodes, the extensional vibration in the x direction is represented by the following dynamic equation:

$$(\partial^2 u/\partial t^2) = F = (\partial X_{11}/\partial x) + (\partial X_{12}/\partial y) + (\partial X_{13}/\partial z), \tag{32}$$

where u is the displacement of the small volume element in the ceramic plate in the x-direction. When the plate is very long and thin, X_2 and X_3 may be set equal to zero through the plate, and the relation between stress, electric field (only E_Z exists) and the induced strain is given by :

$$X_1 = x_1/s_{11}^E - (d_{31}/s_{11}^E)E_Z. \tag{33}$$

Introducing Eq.(33) into Eq.(32), and allowing for $x_1=\partial u/\partial x$ and $\partial E_Z/\partial x=0$ (due to the equal potential on each electrode), leads to a harmonic vibration equation :

$$-\omega^2\rho s_{11}^E u = \partial^2 u/\partial x^2 . \tag{34}$$

Here, ω is the angular frequency of the drive field, and ρ is the density. Substituting a general solution $u=u_1(x)e^{j\omega t}+u_2(x)e^{-j\omega t}$ into Eq.(34), and with the boundary condition $X_1 = 0$ at x = 0 and L (sample length), the following solutions can be obtained:

(strain) $$\partial u/\partial x = x_1 = d_{31}E_Z\,[\sin\omega(L-x)/v + \sin(\omega x/v)]\,/\sin(\omega L/v), \tag{35}$$

(total displacement) $$\Delta L = \int_0^L x_1 dx = d_{31}E_Z L\,(2v/\omega L)\tan(\omega L/2v). \tag{36}$$

Here, v is the sound velocity in the piezoceramic which is given by

$$v = 1 / \sqrt{\rho s_{11}^E} . \tag{37}$$

The admittance for the mechanically free sample is calculated to be:

$$\begin{aligned} Y &= (1/Z) = (i/V) = (i/E_Z t) \\ &= (j\omega wL/t)\,\varepsilon_0\varepsilon_3^{LC}[1 + (d_{31}^2/\varepsilon_0\varepsilon_3^{LC}s_{11}^E)(\tan(\omega L/2v) / (\omega L/2v))], \end{aligned} \tag{38}$$

where w is the width, L the length, t the thickness of the sample, and V the applied voltage. ε_3^{LC} is the permittivity in a longitudinally clamped sample, which is given by

$$\varepsilon_0\varepsilon_3^{LC} = \varepsilon_0\varepsilon_3^X - (d_{31}^2/s_{11}^E) = \varepsilon_0\,\varepsilon_3^X(1 - k_{31}^2) . \tag{39}$$

The final transformation is provided by the definition,

$$k_{31} = d_{31}/\sqrt{s_{11}^E\,\varepsilon_0\varepsilon_3^X} . \tag{40}$$

When the drive frequency is much lower than the resonance, taking ω --> 0 in Eq. (38) leads to $Y = (j\omega wL/t)\,\varepsilon_3^X$ (corresponding to the static capacitance). The piezoelectric resonance is achieved when the admittance becomes infinite or the impedance is zero. The resonance frequency f_R is calculated from Eq. (38), and the fundamental f_R is given by

$$f_R = v/2L = 1/(2L\sqrt{\rho\, s_{11}^E}). \qquad (41)$$

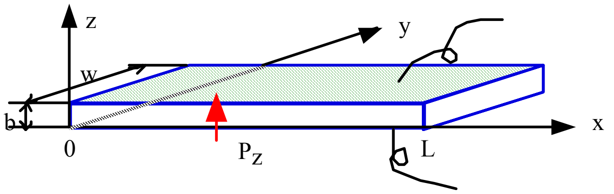

Fig. 6 Longitudinal vibration through the transverse piezoelectric effect (d_{31}) in a rectangular plate.

Now, we will introduce the complex parameters into the admittance curve around the resonance frequency, in a similar way to the previous section: $\varepsilon_3^{X*} = \varepsilon_3^X(1 - j\tan\delta')$, $s_{11}^{E*} = s_{11}^E(1 - j\tan\phi')$, and $d_{31}^* = d(1 - j\tan\theta')$ into Eq. (38):

$$\begin{aligned} Y &= Y_d + Y_m \\ &= (j\omega wL/t)\varepsilon_0\varepsilon_3^X(1 - k_{31}^2)[1 - j\,(1/(1-k_{31}^2))((\tan\delta' + k_{31}^2(\tan\phi' - 2\tan\theta'))] \\ &+ (j\omega wL/t)\varepsilon_0\varepsilon_3^X k_{31}^2\ [(1 - j(2\tan\theta' - \tan\phi')][(\tan(\omega L/2v^*)\,/\,(\omega L/2v^*)] \\ &= j\omega C_d(1 - j\tan\delta) + j\omega C_d K_{31}^2[(1-j(2\tan\theta' - \tan\phi')][(\tan(\omega L/2v^*)/(\omega L/2v^*)], \qquad (42) \end{aligned}$$

where

$$C_0 = (wL/t)\,\varepsilon_0\varepsilon_3^X, \qquad (43)$$

$$C_d = (1 - k_{31}^2)\,C_0\,. \qquad (44)$$

Note that the loss for the first term (damped conductance) is represented by the "extensive" dielectric loss tan δ, not by the intensive loss tan δ'. We further calculate $1/(\tan(\omega L/2v^*)$ with an expansion-series approximation around $(\omega L/2v) = \pi/2$, taking into account that the resonance state is defined in this case for the maximum admittance point, rather than the infinite Y.

Using new frequency parameters,

$$\Omega = \omega L/2\,v,\ \Delta\Omega = \Omega - \pi/2\ (<<1), \qquad (45)$$

and $K_{31}^2 = k_{31}^2/(1 - k_{31}^2)$, the motional admittance Y_m is approximated around the first resonance frequency by

$$Y_m = j(\pi^2/8)\,\omega_0 C_d K_{31}^2\ [(1+j((3/2)\tan\phi' - 2\tan\theta')]/[(-(4/\pi)\Delta\Omega + j\tan\phi'). \qquad (46)$$

The maximum Y_m is obtained at $\Delta\Omega = 0$:

$$Y_m^{\max} = (\pi^2/8)\,\omega_0\,C_d\,K_{31}^2\,(\tan\phi')^{-1} = (\pi^2/8)\,\omega_0\,C_d\,K_{31}^2\,Q_m, \qquad (47)$$

where $Q_m = (\tan\phi')^{-1}$. Similarly, the maximum displacement $u_{\max}$ is obtained at $\Delta\Omega = 0$:

$$u_{\max} = (\pi^2/8)\,d_{31}\,E_Z L\,Q_m. \qquad (48)$$

The maximum displacement at the resonance frequency is $(\pi^2/8)\,Q_m$ times larger than that at a non-resonance frequency, $d_{31}E_ZL$.

In a brief summary, when we observe the admittance or displacement spectrum as a function of drive frequency, and obtain the mechanical quality factor Q_m estimated from $Q_m = \omega_0/2\Delta\omega$, where $2\Delta\omega$ is a full width of the 3 dB down (i.e., $1/\sqrt{2}$) of the maximum value at $\omega = \omega_0$, we can obtain the intensive mechanical loss tan ϕ'.

Equivalent Circuit under High Power Drive

The equivalent circuit for the piezoelectric actuator is represented by a combination of L, C and R. Figure 7 (a) shows an equivalent circuit for the resonance state, which has very low impedance. Taking into account Eq. (42), we can understand that C_d and R_d correspond to the electrostatic capacitance (for a longitudinally clamped sample in the previous case, not a free sample) and the clamped (or "extensive") dielectric loss tan δ, respectively, and the components L_A and C_A in a series resonance circuit are related to the piezoelectric motion. For example, in the case of the longitudinal vibration of the above rectangular plate through d_{31}, these components are represented approximately by

$$L_A = (\rho / 8)(Lb / w)(s_{11}^{E2} / d_{31}^{2}), \tag{49}$$

$$C_A = (8 / \pi^2)(Lw / b)(d_{31}^{2} / s_{11}^{E}). \tag{50}$$

The total resistance R_A ($= R_d + R_m$) should correspond to the loss tan ϕ', which is composed of the extensive mechanical loss tan ϕ and dielectric/piezoelectric coupled loss (tan δ - 2tan θ) (see Eq. (30)). Thus, intuitively speaking, R_d and R_m correspond to the extensive dielectric and mechanical losses, respectively. Note that we introduced an additional resistance R_d to explain a large contribution of the dielectric loss when a vibration velocity is relatively large.

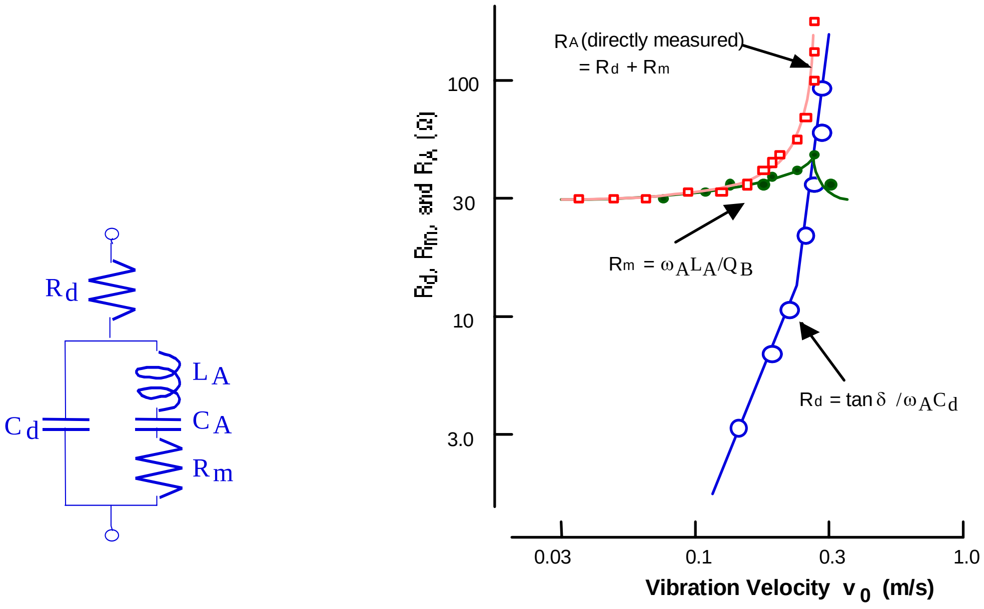

(a) (b)

Fig. 7 (a) Equivalent circuit of a piezoelectric device for the resonance under high power drive. (b) Vibration velocity dependence of the resistances R_d and R_m in the equivalent electric circuit for a longitudinally vibrating PZT ceramic transducer through the transverse piezoelectric effect d_{31}.

Losses as a Function of Vibration Velocity

Let us consider here the degradation mechanism of the mechanical quality factor Q_m with increasing electric field and vibration velocity. Figure 8 shows the change in mechanical Q_m with vibration velocity. Q_m is almost constant for a small electric field/vibration velocity, but above a certain vibration level Q_m degrades drastically, where temperature rise starts to be observed [7]. Figure 7 (b) depicts an important notion on heat generation from the piezoelectric material, where the damped and motional resistances, R_d and R_m, in the equivalent electrical circuit of a PZT sample (Fig. 7 (a)) are separately plotted as a function of vibration velocity. Note that R_m, mainly related to the extensive mechanical loss (90^o domain wall motion), is insensitive to the vibration velocity, while R_d, related to the extensive dielectric loss (180^o domain wall motion), increases significantly around a certain critical vibration velocity. Thus, the resonance loss at a small vibration velocity is mainly determined by the extensive mechanical loss which provides a high mechanical quality factor Q_m, and with increasing vibration velocity, the extensive dielectric loss contribution significantly increases. This is consistent with the discussion made on Fig. 5. After R_d exceeds R_m, we started to observe heat generation.

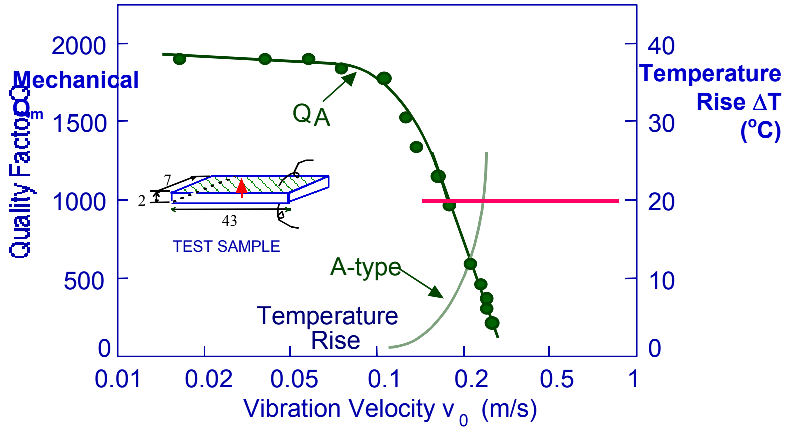

Fig. 8 Vibration velocity dependence of the quality factor Q_A and temperature rise for A (resonance) type resonance of a longitudinally vibrating PZT ceramic transducer through the transverse piezoelectric effect d_{31}. The maximum vibration velocity is defined at the velocity where 20°C temperature rise from room temperature is exhibited.

HEAT GENERATION IN PIEZOELECTRICS

Heat generation in various types of PZT-based actuators has been studied under a large electric field applied (1 kV/mm or more) at an off-resonance frequency and under a relatively small electric field applied (100 V/mm) at a resonance frequency.

Zheng et al. reported the heat generation at an off-resonance frequency from various sizes of multilayer type piezoelectric ceramic actuators [4]. The temperature change with time in the actuators was monitored when driven at 3 kV/mm and 300 Hz, and Fig. 9 plots the saturated temperature as a function of V_e/A, where V_e is the effective volume (electrode overlapped part) and A is the surface area. This linear relation is reasonable because the volume V_e generates the heat and this heat is dissipated through the area A. Thus, if we need to suppress the temperature rise, a small V_e/A design is preferred. From these experimental results, we calculated the total loss u of the piezoelectric, which are summarized in Table I. The experimental data of *P-E* hysteresis losses under a stress-free condition are also listed for comparison. It is very important that the *P-E* hysteresis intensive loss agrees well with the total loss contributing to the heat generation under an off-resonance drive.

S. Tashiro et. al observed the heat generation in a rectangular piezoelectric plate during a resonating drive [8]. Even though the maximum electric filed is not very large, heat is generated due to the large induced strain/stress at the resonance. Figure 10 depicted an infrared image taken for a resonating rectangular PZT plate in our laboratory.

The maximum heat generation was observed at the nodal point of the resonance vibration, where the maximum strain/stress are generated. This observation supports that the heat generation in a resonating sample is attributed to the intensive elastic loss tan ϕ'. This is not contradictory to the result in the previous paragraph, where a high-voltage was applied at an off-resonance frequency. We concluded there that the heat is originated from the intensive dielectric loss tan δ'. In consideration that both the "intensive" dielectric and mechanical losses are composed of the "extensive" dielectric and mechanical losses, and that the extensive dielectric loss tan δ changes significantly with the external electric field and stress, the major contribution to the heat generation seems to come from the "extensive" dielectric loss (i.e., 180° domain wall motion). Further investigations are waited for the microscopic observation of this phenomenon.

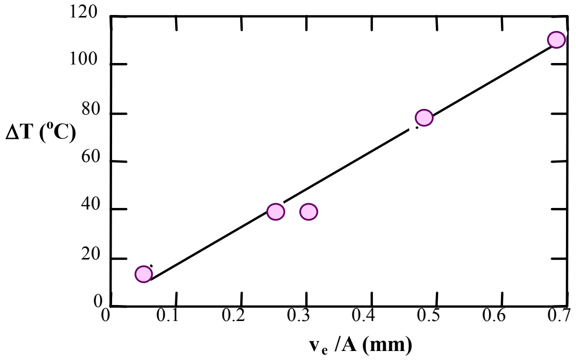

Fig. 9 Temperature rise at off-resonance versus V_e/A (3 kV/mm, 300 Hz) in various size soft PZT multilayer actuators, where V_e is the effective volume generating the heat and A is the surface area dissipating the heat.

Table I Loss and overall heat transfer coefficient for PZT multilayer samples (E = 3 kV/mm, f = 300 Hz).

Actuator	4.5x3.5x2 mm	7x7x2 mm	17x3.5x1 mm
Total loss ($\times 10^3$J/m^3) $u = \frac{\rho c v}{f v_e}\left(\frac{dT}{dt}\right)_{t\to 0}$	**19.2**	**19.9**	**19.7**
***P-E* hysteresis loss ($\times 10^3$J/m^3)**	**18.5**	**17.8**	**17.4**
k(*T*) (W/m^{2}K)	**38.4**	**39.2**	**34.1**

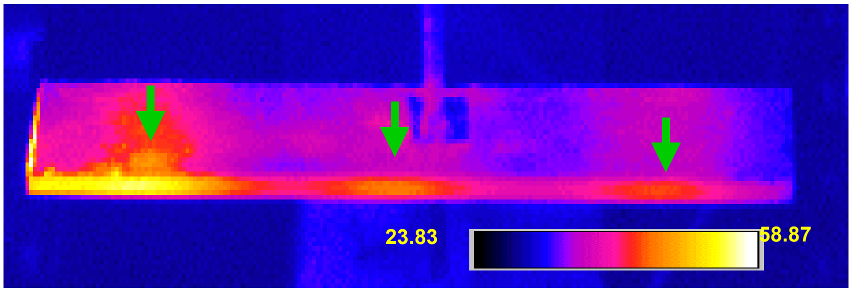

Fig. 10 An infrared image of a "hard" PZT rectangular plate driven at the second resonance mode. Note three hot points, which correspond to the nodal points for this vibration mode.

HIGH POWER PIEZOELECTRICS

Practical PZT Based Ceramics

"High Power" in this paper stands for high power density in mechanical output energy converted from the maximum input electrical energy under the drive condition with 20°C temperature rise. The mechanical power density can be evaluated by the square of the maximum vibration velocity (v_0^2), which is a sort of material's constant (Remember that the piezoelectric becomes a ceramic heater above a certain vibration level). Figure 11 shows the mechanical Q_m versus basic composition x at two effective vibration velocities $v_0 = 0.05$ m/s and 0.5 m/s for $Pb(Zr_xTi_{1-x})O_3$ doped with 2.1 at.% of Fe [9]. The decrease in mechanical Q_m with an increase of vibration level is minimum around the rhombohedral-tetragonal morphotropic phase boundary (52/48). In other words, the smallest Q_m material at a small vibration level becomes the best at a large vibration level, and the data obtained by a conventional impedance analyzer with a small voltage/power does not provide data relevant to high power materials. Thus, we developed various measuring techniques of high power piezoelectricity, including "Constant Current" and "pulse drive" methods [10].

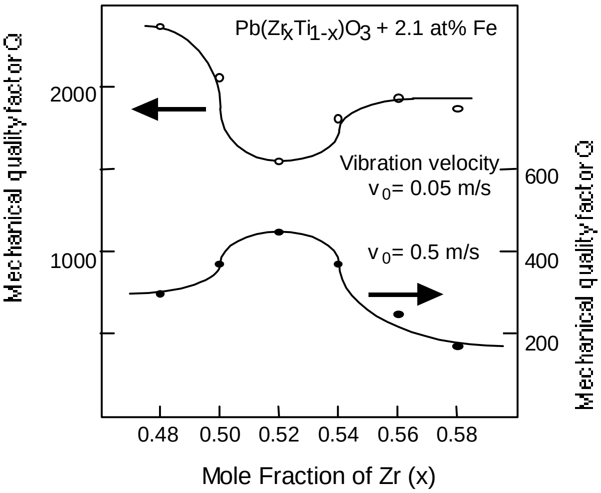

Fig. 11 Mechanical Q_m versus basic composition x at two effective vibration velocities v_0=0.05 m/s and 0.5 m/s for $Pb(Zr_xTi_{1-x})O_3$ doped with 2.1 at.% of Fe.

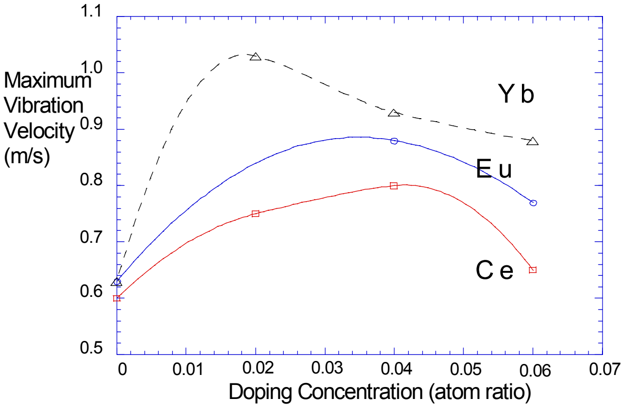

Fig. 12 Dependence of the maximum vibration velocity v_0 (20°C temperature rise) on the atomic % of rare-earth ion, Yb, Eu or Ce in the $Pb(Mn,Sb)O_3$ (PMS) – PZT based ceramics.

The conventional piezo-ceramics have the limitation in the maximum vibration velocity (v_{max}), since the additional input electrical energy is converted into heat, rather than into mechanical energy. The typical rms value of v_{max} for commercially available materials, defined by the temperature rise of 20°C from room temperature, is around 0.3 m/sec for rectangular samples operating in the k_{31} mode (like a Rosen-type transformer) [7]. $Pb(Mn,Sb)O_3$ (PMS) - lead zirconate tatanate (PZT) ceramics with the v_{max} of 0.62 m/sec are currently used for NEC transformers [9]. By doping the PMS-PZT or $Pb(Mn,Nb)O_3$-PZT with rare-earth ions such as Yb, Eu and Ce, we recently developed the high power piezoelectrics, which can operate with v_{max} up to 1.0 m/sec [11, 12]. Compared with commercially available piezoelectrics, 10 times higher input electrical energy and output mechanical energy can be expected from these new materials without generating significant temperature rise. Figure 12 shows the dependence of the maximum vibration velocity v_0 (20°C temperature rise) on the atomic % of rare-earth ion, Yb, Eu or Ce in the $Pb(Mn,Sb)O_3$ (PMS) – PZT based ceramics. Enhancement in the v_0 value is significant by adding a small amount of the rare-earth ion [12].

Origin of the High Power Piezoelectrics

"Hard" PZT is usually used for high power piezoelectric applications, because of its high coercive field; in other words, the stability of the domain walls. Acceptor ions, such as Fe^{3+}, introduce oxygen deficiencies in the PZT crystal (In the case of donor ions, such as Nb^{5+}, Pb deficiency is introduced). Thus, the acceptor doping causes domain pinning through the easy reorientation of deficiency-related dipoles, leading to "hard" characteristics (Domain Wall Pinning Model [13]).

High mechanical Q_m is essential in order to obtain a high power material with a large maximum vibration velocity. Figure 13 exhibits suggestive results in the mechanical Q_m increase with time lapse (minute) after the electric poling measured for various commercial soft and hard PZTs, PSM-PZT, and PSM-PZT doped with Yb. Note first that the Q_m values for hard PZT and our high power piezoelectrics were almost the same, slightly higher than soft PZTs, and around 200-300 just after the poling. After a couple of hours passed, the Q_m values increased more than 1000 for the "hard" materials, while no change was observed in the "soft" material. The increasing slope is the maximum for the Yb-doped PSM-PZT. Note second that this gradual increase (in a couple of hours) in the Q_m cannot be explained by the above-mentioned "domain wall pinning" model, but more likely by some ionic diffusion model.

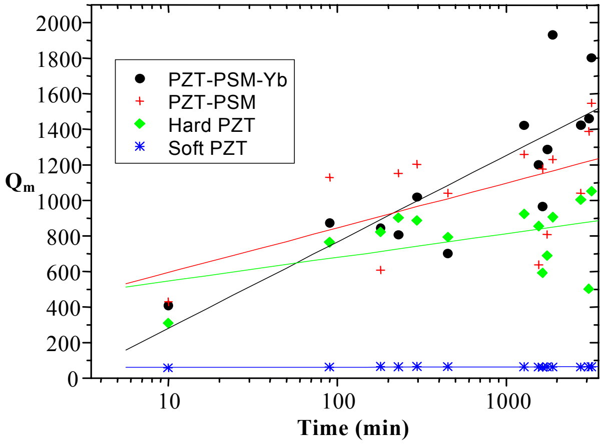

Fig. 13 Change of the mechanical Q_m with time lapse (minute) just after the electric poling measured for various commercial soft and hard PZTs, PSM-PZT, and PSM-PZT doped with Yb.

Figure 14 shows the polarization vs. electric field hysteresis curves measured for the Yb-doped $Pb(Mn,Sb)O_3$- PZT sample just after poling (fresh), 48 hours after, and a week after (aged). Remarkable aging effects could be observed; (a) in the decrease in the magnitude of the remnant polarization, and (b) in the positive internal bias electric field growth (i.e., the hysteresis curve shift leftwards in terms of the external electric field axis). The phenomenon (a) can be explained by the local domain wall pinning effect, but the large internal bias (more than 1 kV/mm) growth (b) seems to be the origin of the high power characteristics. Suppose that the vertical axis in Fig. 5 shifts rightwards, the inverse electric field required for realizing the 180^o polarization reversal is increased, leading to the resistance enhancement against generating the hysteresis or heat.

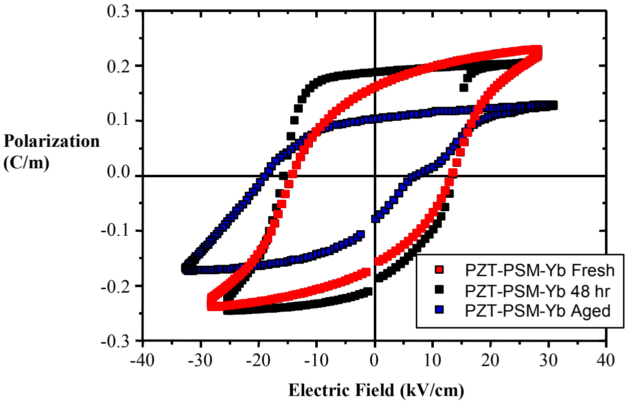

Fig. 14 Polarization vs. electric field hysteresis curves measured for the Yb-doped Pb(Mn,Sb)O_3- PZT sample just after poling (fresh), 48 hours after, and a week after (aged).

Finally, let us propose the origin of this internal bias field growth. Based on the necessity of the oxygen deficiencies and the relatively slow (a couple of hours) growth rate, we assume here the oxygen deficiency diffusion model, which is illustrated in Fig. 15. Under the electric poling process, the defect dipole P_{defect} (a pair of acceptor ion and oxygen deficiency) will be arranged parallel to the external electric field. After removing the field, the oxygen diffusion occurs, which can be estimated in a scale of hour at room temperature. Taking into account slightly different atomic distances between the A and B ions in the perovskite crystal in a ferroelectric (asymmetric) phase, the oxygen diffusion probability will be slightly higher for the downward, as shown in the figure, leading to the increase in the defect dipole with time. This may be the origin of the internal bias electric field.

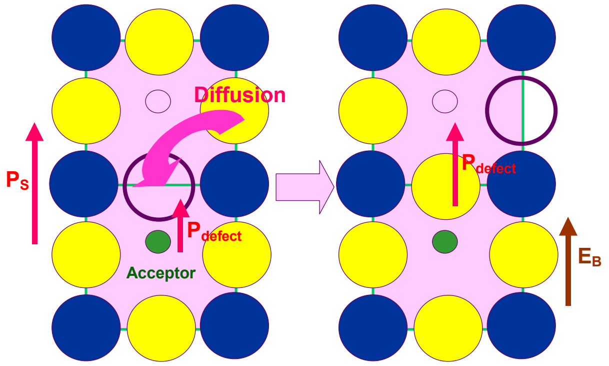

Fig. 15 Oxygen deficiency diffusion model for explaining the internal bias electric field growth.

CONCLUSIONS

(1) There are three loss origins in piezoelectrics: dielectric, elastic and piezoelectric losses. 180^O and non-180^O domain wall motions contribute primarily to the dielectric and elastic losses, respectively.

(2) Heat generation occurs in the sample uniformly under an off-resonance mainly due to the intensive dielectric loss, while heat is generated primarily at the vibration nodal points via the intensive elastic loss under a resonance.

(3) Doping rare-earth ions into PZT-Pb(Mn,X)O_3 (X = Sb, Nb) ceramics increases the maximum vibration velocity up to 0.9 m/s, which corresponds to one order of magnitude higher energy density than conventionally commercialized piezo-ceramics.

(4) To obtain stabilized high vibration velocity, domain wall stabilization via the positive internal bias field (rather than local domain wall pinning) seems to be essential.

Since the above conclusions were derived only from a limited number of PZT-based soft and hard piezoelectrics, it is too early to generalize these conclusions. Further investigations are highly required.

ACKNOWLEDGEMENT

Part of this research was supported by the Office of Naval Research through the grant no. N00014-96-1-1173 and N00014-99-1-0754.

REFERENCES

1. K. H. Haerdtl, Ceram. Int'l., **8**, 121-127 (1982).
2. T. Ikeda, *Fundamentals of Piezoelectric Materials Science*, (Ohm Publication Co., Tokyo, 1984), pp. 83.
3. K. Uchino and S. Hirose, IEEE-UFFC Trans., **48**, 307-321 (2001).
4. J. Zheng, S. Takahashi, S. Yoshikawa, K. Uchino and J. W. C. de Vries, J. Amer. Ceram. Soc., **79**, 3193-3198 (1996).
5. N. Uchida and T. Ikeda, Jpn. J. Appl. Phys., **6**, 1079 (1967).
6. K. Uchino, *Piezoelectric Actuators and Ultrasonic Motors*, (Kluwer Academic Publ., Boston, 1997), pp. 197.
7. S. Hirose, M. Aoyagi, Y. Tomikawa, S. Takahashi and K. Uchino, Proc. Ultrasonics Int'l '95, Edinburgh, pp. 184-187 (1995).
8. S. Tashiro, M. Ikehiro and H. Igarashi, Jpn. J. Appl. Phys., **36**, 3004-3009 (9197).
9. S. Takahashi and S. Hirose, Jpn. J. Appl. Phys., **32**, 2422-2425 (1993).
10. K. Uchino, J. Zheng, A. Joshi, Y. H. Chen, S. Yoshikawa, S. Hirose, S. Takahashi and J. W. C. de Vries, J. Electroceramics, **2**, 33-40 (1998).
11. J. Ryu, H. W. Kim, K. Uchino and J. Lee, Jpn. J. Appl. Phys., **42**, No. 3, 1-4 (2003).
12. Y. Gao, K. Uchino and D. Viehland, J. Appl. Phys., **92**, 2094-2099 (2002).
13. K. Uchino, *Ferroelectric Devices*, (Marcel Dekker, Inc., New York, 2000), pp. 63.